Numerical Modeling of Transport Phenomena
in Reactive Porous Structures for Solar Fuel Applications

A DISSERTATION
SUBMITTED TO THE FACULTY OF THE GRADUATE SCHOOL
OF THE UNIVERSITY OF MINNESOTA
BY

Daniel Joseph Keene

IN PARTIAL FULFILLMENT OF THE REQUIREMENTS
FOR THE DEGREE OF
DOCTOR OF PHILOSOPHY

Drs. Wojciech Lipiński and Jane H. Davidson, Co-advisers

August 2013

Acknowledgements

Dedication

To Jamie, the best friend and wife I could ever ask for—my true ezer kenegdo.

Abstract

The focus of this work is the development and use of a numerical model to study solar thermochemical fuel production using nonstoichiometric ceria in the form of a reactive porous medium. Volume averaging theorems are applied at the pore-level to obtain a set of governing equations that use effective transport properties to describe the heat and mass transfer processes in the reactive porous medium on the macroscale. Reaction rate expressions are formulated for both the thermal reduction and oxidation steps as an interphase mass flux whose dependence on the partial pressures, solid temperature, and nonstoichiometry is derived from the ionization state of the oxygen vacancies.

The porosity and pore-level solid feature size (as represented by a Sauter mean diameter) of a porous monolith are varied from 0.6 to 0.9 and 10 to 1000 μm, respectively, to determine their impact on the rate of oxygen release and the solar-to-chemical energy conversion efficiency during thermal reduction while the macroscale geometry and operating conditions are held fixed. The process is carried out in a batch mode by placing the reactive medium inside a cavity where it is directly irradiated with a concentrated solar flux as a sweep gas passes through its pore network. The best performance is obtained with a non-uniform heating of the solid, which is attributed to the nonlinear temperature dependence of the equilibrium nonstoichiometry. The solar-to-chemical energy conversion efficiency attains its highest value of 10.9 % with a porosity of 0.9 and a Sauter mean diameter of 10 μm. These results imply that high porosities and small feature sizes are preferred, but it is recognized and discussed that these findings are strongly tied to the particular set of operating conditions considered.

The mathematical model is also used in conjunction with available experimental data to develop a method for determining a reaction rate expression that characterizes the oxidation of ceria by carbon dioxide. The volume-averaged conservation equations for the porous medium are used to simulate a packed bed of porous particles and the axially-dispersed plug flow model is used to compare numerical predictions of the effluent composition with experimental measurements. Reaction rate expressions are developed and their kinetic parameters are determined by minimizing the difference between the numerical predictions

and the experimental measurements as quantified by a root mean square error for a temperature of 1203 K. At this temperature, numerical results obtained using a reaction rate expression based on singly ionized oxygen vacancies provide excellent agreement with the experimental data.

Contents

List of Tables

List of Figures

Nomenclature

a_{sf} interfacial surface area per unit total volume ($m^2 m^{-3}$)

C concentration ratio

c interparticle clearance (m)

$\bar{c}_p$ molar specific heat ($J\ kmol^{-1}\ K^{-1}$)

D diameter (m), diffusion coefficient ($m^2 s^{-1}$)

d_{32} Sauter mean diameter used to describe pore-scale feature size (m)

E residence time distribution function (s^{-1})

$E_{b\lambda}$ spectral hemispherical emissive power of a blackbody ($W\ m^{-2} \mu m^{-1} K^{-4}$)

F view factor

g scattering asymmetry factor

h enthalpy ($J\ kg^{-1}$)

$\bar{h}$ molar enthalpy ($J\ kmol^{-1}$)

$h_{O_2,sf}$ enthalpy for interphase flux of oxygen ($J\ kg^{-1}$)

h_{sf} interphase heat transfer coefficient ($W\ m^{-2} K^{-1}$)

H irradiation ($W\ m^{-2}$)

I nominal terrestrial solar irradiation ($1000\ W\ m^{-2}$)

K permeability (m^2)

K_{KV} equilibrium constant for doubly ionized vacancy reduction reaction

$K_{KV,d}$ equilibrium constant for doubly ionized vacancy oxidation reaction

$K_{KV,s}$ equilibrium constant for singly ionized vacancy oxidation reaction

k thermal conductivity ($W\ m^{-1} K^{-1}$)

k_K Kozeny constant

L length of domain (m)

M molecular weight ($kg\ kmol^{-1}$)

m mass (kg)

$\dot{m}''_{sf}$ interphase mass flux from solid to fluid ($kg\ m^{-2}\ s^{-1}$)

N number of chemical species in the gas phase

$N_{\Delta z}$ total number of cells

Nu_{pore} pore-scale Nusselt number

n refractive index

n_{O_2} amount of diatomic oxygen produced (kmol)

$\dot{n}''_{O_2}$ molar production rate of diatomic oxygen per unit cross-section area (kmol m^{-2}s^{-1})

$\hat{n}_{\text{sf}}$ outward unit normal vector for the solid phase

$\dot{n}''_{\text{sf},0}$ kinetic rate constant (kmol$_\text{O}$ m^{-2}s^{-1})

Pe_{disp} axially-dispersed plug flow model parameter

Pr Prandtl number

p pressure (Pa)

Q heat (J); radiative efficiency factor

$\dot{Q}$ heat rate (W)

$\dot{Q}'''$ heat rate per unit volume (Wm^{-3})

q'' heat flux (W m^{-2})

r radial coordinate (m)

R radius of cylindrical domain (m)

$\bar{R}$ universal gas constant (J kmol^{-1}K^{-1})

T temperature (K)

t time (s)

t_{res} axially-dispersed plug flow model parameter (s)

u velocity (m s^{-1})

V volume (m^{3})

X mole fraction

Y mass fraction

z axial coordinate (m)

Greek Symbols

α total hemispherical absorptivity

β^{tr} transport extinction coefficient (m^{-1})

β_m^{tr} Rosseland-mean transport extinction coefficient (m^{-1})

η_{batch} overall solar-to-chemical energy conversion efficiency

$\Delta \bar{h}_{CO_2}^0$ standard enthalpy change for CO_2 dissociation (J kmol^{-1})

$\Delta \bar{h}_{KV}^0$ standard enthalpy change for Eq. (3.6) (J kmol^{-1})

$\Delta \bar{h}_{KV,d}^0$ standard enthalpy change for Eq. (5.5) (J kmol^{-1})

$\Delta \bar{h}_{KV,s}^0$ standard enthalpy change for Eq. (5.14) (J kmol^{-1})

$\Delta \bar{h}_{O_2}^0$ standard oxidation enthalpy change (J kmol^{-1})

$\Delta \bar{h}_{red}$ molar heat of reduction defined by Eqs. (3.14) and (3.15) (J kmol^{-1})

$\Delta \bar{s}_{CO_2}^0$ standard entropy change for CO_2 dissociation (J kmol^{-1}K^{-1})

$\Delta \bar{s}_{KV}^0$ standard entropy change for Eq. (3.6) (J kmol^{-1} K^{-1})

$\Delta \bar{s}_{KV,d}^0$ standard entropy change for Eq. (5.5) (J kmol^{-1} K^{-1})

$\Delta \bar{s}_{KV,s}^0$ standard entropy change for Eq. (5.14) (J kmol^{-1} K^{-1})

$\Delta \bar{s}_{O_2}^0$ standard oxidation entropy change (J kmol^{-1})

$\Delta \bar{g}_{CO_2}^0$ standard Gibbs free energy change for CO_2 dissociation (J kmol^{-1})

$\Delta \bar{g}_{O_2}^0$ standard oxidation Gibbs free energy change (J kmol^{-1})

Δz cell size (m)

δ nonstoichiometry

∂V boundary of volume V (m^2)

ϵ total hemispherical emissivity

γ geometric grid stretching parameter

λ wavelength (m)

μ dynamic viscosity (kg m^{-1}s^{-1})

ν stoichiometric coefficient

ϕ porosity

ψ generic operand

ρ density (kg m^{-3})

σ Stefan–Boltzmann constant (W m^{-2}K^{-4})

τ time constant (s)

ω scattering albedo

Subscripts

0   location $z = 0$

∞ ambient location upstream of $z = 0$

abs   absorption

apert   aperture

calc   calculated

chem   chemistry

coarse coarse grid region

cr   critical

disp   dispersion

eff   effective

end   endpoint

eq   equilibrium

i species index; dummy counter

iz cell index

i   initial

inter   interparticle

intra   intraparticle

f   fluid

fine   fine grid region

form   formation

L location $z = L$

PBPP   packed bed of porous particles

p   particle

r   radial

rad   radiative

ref   reference

s   solid

sca   scattering

stag   stagnant

z axial, streamwise

λ spectral

Superscripts

inter   interparticle

intra   intraparticle

Other Symbols

$\langle\ \rangle$ superficial average

$\langle\ \rangle^{j}$ intrinsic average over phase j

$[\ \ ]$ normalized concentration operator

Ce'_{Ce} cerium atom (at cerium lattice site) in 3+ state

Ce^{X}_{Ce} cerium atom (at cerium lattice site) of neutral charge

O^{X}_{O} oxygen atom (at oxygen site) with neutral charge

$V^{\cdot\cdot}_{O}$ vacancy (at oxygen lattice site) with 2- state

$V^{\cdot}_{O}$ vacancy (at oxygen lattice site) with 1- state

Chapter 1
Introduction

Meeting the global demand for energy is among the chief concerns of our time. If the projected future demands are to be met with renewable sources, there is only one with the necessary abundance: the sun. In fact, as sunlight strikes the earth, the energy received in just one hour exceeds the total amount consumed by mankind throughout the entire year [1]. Therefore, an effective means to address the energy challenge is to develop methods for converting solar energy into more usable forms.

While solar energy is plentiful, it is neither steadily nor uniformly available. Consequently, storage must be an integral part of any solar technology if it is to meet a significant fraction of the global demand for energy. Using concentrated solar irradiation to drive thermochemical processes is such a technology because it allows solar energy to be stored in a dense and stable chemical form. Of particular interest is the splitting of water and carbon dioxide because the hydrogen and carbon monoxide products can be combined to form synthesis gas, which can be converted to liquid hydrocarbons using well-established methods. These "solar fuels" can easily replace their petroleum-based alternatives without necessitating a new infrastructure, thereby avoiding this tremendous drawback to a purely hydrogen-based system. Furthermore, the production and consumption of solar fuels creates a closed material cycle, a quality which is essential for long-term sustainability.

Therefore, solar energy can be concentrated to produce a variety of high-value chemical products through the splitting of water and/or carbon dioxide. However, direct thermolysis not only requires very high temperatures to achieve significant conversion, but a high temperature gas separation process is required in order to prevent the thermodynamic penalty (and potential danger) of product recombination [2–5]. These requirements have led researchers to thermochemical cycles that accomplish the splitting

1

using a series of steps in order to lower the operating temperatures and obviate the separation challenge by producing the oxygen and hydrogen in distinct steps.

Among the multitude of cycles identified, two-step cycles based on metal oxide redox chemistry show great promise [6–8]. Partial redox cycles are an intriguing option and feature a multivalent metal whose oxide can remain solid throughout the entire cycle, as shown for the case of cerium oxide (ceria) in Eqs. (1.1)–(1.2):

Solar step:
$$CeO_2(s) \rightarrow CeO_{2-\delta}(s) + \frac{\delta}{2}O_2(g) \tag{1.1}$$

Non-solar step:
$$\delta H_2O(g) + CeO_{2-\delta}(s) \rightarrow CeO_2(s) + \delta H_2(g) \tag{1.2a}$$

or

$$\delta CO_2(g) + CeO_{2-\delta}(s) \rightarrow CeO_2(s) + \delta CO(g) \tag{1.2b}$$

Net cycle:
$$\delta H_2O(g) \rightarrow \delta H_2(g) + \frac{\delta}{2}O_2(g) \tag{1.3a}$$

or

$$\delta CO_2(g) \rightarrow \delta CO(g) + \frac{\delta}{2}O_2(g) \tag{1.3b}$$
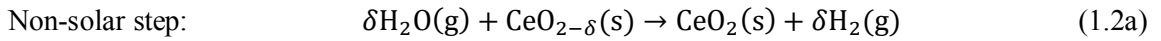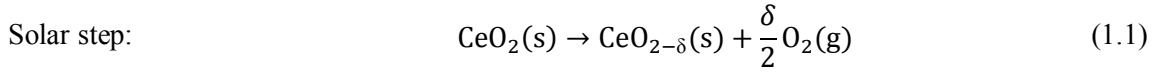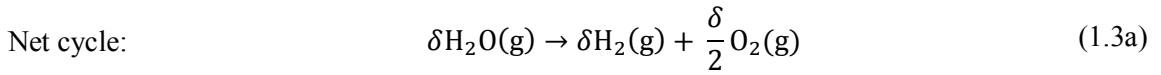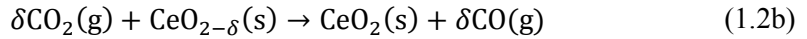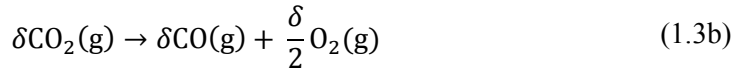
Because the metal oxide remains solid in its reduced state, the separation challenge is completely eliminated. However, these cycles present a new set of design challenges. In comparison to other cycles, the solid materials produce less fuel per unit mass of metal. This decrease in gravimetric fuel productivity leads to increased cycling rates and a greater need for recuperating sensible heat to achieve good fuel production rates and efficiencies, respectively. The solid phase requires a high surface area per unit mass to promote rapid kinetics because of the heterogeneous nature of the chemical reaction, but it must also be capable of absorbing concentrated solar irradiation.

Therefore, a promising strategy is to form the metal oxide into a porous structure because it satisfies these important requirements by achieving a large surface area while remaining optically thick. Furthermore, as transport processes are influenced by both inherent material properties and pore-scale morphology, the porous medium can be

tailored to achieve a desired set of macroscopic characteristics. This flexibility presents a multitude of choices with their associated trade-offs, and raises the question at the heart of this research: how can the pore architecture be engineered in order to optimize the solar-to-chemical energy conversion?

Optimizing solar thermochemical fuel production relies on understanding the predominant phenomena for each step of the partial redox cycle shown in Fig. 1.1. During the reduction step, concentrated solar irradiation drives the release of oxygen from the solid phase, where it will then be transported through the void space by convection and/or diffusion. Of utmost importance is matching the delivery of solar energy with the endothermic requirement of the reaction, which requires an in-depth understanding of how the heat and mass transfer processes interact throughout the reactive porous structure. During the oxidation step, a feedstock (water or carbon dioxide) is delivered through the pore network where it can react with the metal oxide to produce the chemical fuel (hydrogen or carbon monoxide). Here, mass transfer becomes very important because the gas phase transport is responsible for both delivering the feedstock to the reduced solid (so that the reaction can occur) and carrying the chemical fuel away from the oxidized solid (so that the reverse reaction does not become favored). Clearly, controlling the interactions between the chemistry and the heat and mass transfer processes is at the center of developing high performance porous materials for solar thermochemical fuel production.

The goal of this research has been to use numerical simulations to provide insight into these coupled phenomena to identify porous structures that will optimize performance. This thesis is organized by the primary tasks that have been accomplished in support of achieving this objective. Chapter 2 contains a literature review that places this work within the broader context of identifying promising routes to solar thermochemical fuel production and prior modeling efforts. Chapter 3 consists of a research paper that has been published in the ASME Journal of Heat Transfer. Its focus is presenting the multi-scale model developed to study the multimode heat and mass transfer processes during nonstoichiometric thermal reduction, describing the details of the numerical method employed by the computational code developed to solve the governing equations, and

illustrating the insights provided by the numerical simulations using results from a test case. Chapter 4 consists of a manuscript that has been submitted for publication in the American Institute of Chemical Engineers Journal. It builds on the developed numerical simulation capabilities outlined in Chapter 3 to explore the impact of the morphological parameters of a porous monolith on the rate of oxygen release and solar-to-chemical energy conversion efficiency during nonstoichiometric thermal reduction. Chapter 5 outlines a procedure that has been developed wherein numerical simulations are utilized in conjunction with experimental data to determine a reaction rate expression for the oxidation of ceria by carbon dioxide. Chapter 6 contains a comprehensive summary, conclusions, and suggestions for future work.
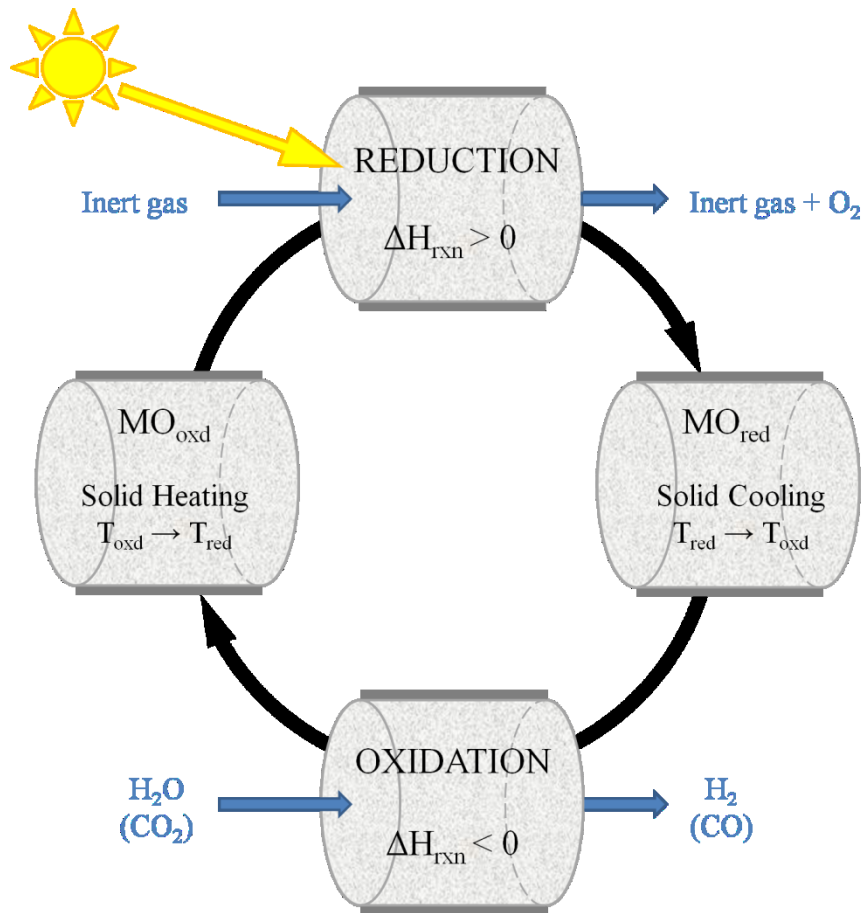
Fig. 1.1. Overview of a porous medium accomplishing a solar-driven partial redox thermochemical cycle. Concentrated solar irradiation drives the high temperature endothermic reaction that transforms the solid from its oxidized state (MO_{oxd}) to its reduced state (MO_{red}); subsequent exposure to an oxidizing agent at a lower temperature produces the chemical fuel and recharges the material.

Chapter 2
Background

Non-volatile metal oxides possess many attractive qualities and are consequently being studied for solar thermochemical fuel production. After briefly summarizing the advancements made in materials and reactor development, the surprisingly scant characterization of partial redox materials and its impact on reactor design is discussed. Then, studies that have modeled similar chemical processes in porous media are considered to highlight prior work that will inform the modeling approach being undertaken in this research and place it in an appropriate context.

Multivalent Metal Oxides for Solar Fuel Production

Materials Development

Since the introduction of the iron oxide cycle [9], most efforts have been focused on bringing down the operating temperature by using various metals (Ni, Mn, Co, Zn, Mg) as partial substitutions for iron to form mixed metal oxides [6], although one study has considered a nonstoichiometric process[1] [10]. The use of support materials [6,11–13] and iron-containing zirconia processes [14,15] have been studied in attempts to mitigate sintering, but have not proved entirely successful.

An alternative to the ferrites that has been receiving increased attention are cerium-based oxides. Although ceria had been studied for decomposing water at low temperatures [16], its use in a solar-driven water-splitting cycle was not considered until more recently [17]. Ceria seems particularly well-suited for a nonstoichiometric process because it can achieve a high degree of nonstoichiometry while preserving its cubic fluorite crystal structure, and experimental tests show that the kinetics and gravimetric fuel productivity are at least as good as the best ferrites [18]. Various partial substitutions for cerium have also been investigated [19–26] in hopes of bringing down the

---

[1] In contrast to accomplishing a conversion of magnetite (Fe_3O_4) to wustite (FeO), only a fraction of the Fe cations experience a change in valence state so that the spinel crystal structure is maintained but populated with defects throughout.

temperatures required for thermal reduction and stabilizing the lattice to better resist sintering, but this typically degrades the ability of the material to split water and/or carbon dioxide.

Implications for Reactor System Development

While materials development is still ongoing, multiple reactor concepts have already been tested. The early solar reactors were based on unreactive ceramic structures with ferrite coatings [27,28], and this concept is still being studied with new materials [29,30]. Both a Ni,Mn-ferrite and ceria coating were used when adapting this strategy to a novel rotary type reactor [31]. More recently, reactor concepts have moved to forming porous structures composed entirely of the materials that were previously only applied as coatings. Examples include a cavity-based system featuring a stationary porous medium [32–34] and the novel counter-rotating-ring receiver/reactor/recuperator (CR5) chemical heat engine [35].

Taken collectively, the body of work accomplished and the progress in the development of solar-driven thermochemical reactors might suggest that these systems are well understood at a level that is informing the design of prototype reactors and their scale-up. In fact, it has even been stated that reactor performance is now limited by system scale and design features rather than by chemistry [32], which suggests that the chemistry has been at least well characterized if not optimized. However, a closer look at the tests performed throughout the materials development literature shows how this implied state of affairs is not the case.

The materials development efforts have essentially functioned as preliminary screening studies where various compositions and synthesis methods were used in search of a material with convenient operating temperatures and good fuel productivity. While these metrics are important, they are not the only factors that must be considered when designing a reactor. The primary goal is to match the absorption of concentrated solar irradiation to the energy requirement of the chemical reaction while also allowing for rapid rates of fuel production, but neither the radiative properties nor the intrinsic kinetics were quantified. Of course, detailed mechanistic modeling of the chemical kinetics may

not be necessary, but no attempts have been made to extract even an overall rate law expression. Perhaps the inherent difficulty of extracting meaningful kinetic data makes it prohibitive during a first assessment of a new material, but it is clear (from the existence of functioning reactors) that promising candidates have been identified. Furthermore, the reactivity of the materials being developed has been investigated using packed beds of powders (under presumably isothermal conditions), so these experiments would seem ideally suited for determining rate law information. So, while gravimetric fuel productivity has been determined, rate law information that could have been obtained is still unknown because no attempts were made to extract kinetic parameters.

From this discussion, it is clear that two important prerequisites for moving beyond demonstrative prototypes are missing. First, the partial redox materials to be employed in solar reactors need to be more fully characterized (and optimized), especially in regard to kinetics and radiative properties. Recent studies have used experimental [36–38] and tomography-based [39] methods to determine the extinction coefficients of porous ceria structures, but have not considered a wide variety of morphologies. While the thermal reduction reaction appears to be limited by the rate at which the solid can be heated [18,34], the kinetics of oxidation have not yet been characterized beyond measurements of the effluent gas composition obtained with different materials and morphologies [18,26,32–34,40–42]. These studies are able to make valuable comparisons between different materials and/or morphologies, but because they consider only the observed (rather than intrinsic) kinetics, they must be carefully interpreted within the context of their particular set of operating conditions. Second, efforts need to be undertaken so that once a suitable material has been properly characterized, this information can be used to design reactive structures that will lead to effective solar reactors.

The present work uses numerical simulations to address both the need for a more complete kinetic characterization and a better understanding of how the morphological parameters of a porous structure will impact its thermochemical performance. As this involves modeling the chemical and transport processes in a reactive porous structure, previous pertinent studies will now be reviewed.

Previous Studies and their Modeling Approaches

This research uses transport modeling to determine how partial redox materials can be effectively utilized in a solar reactor system when formed into a porous structure. The general class of systems being modeled is a porous medium where the solid phase reacts with the gas phase and participates in the radiative heat transfer arising from the high temperatures associated with the chemical processes and/or direct external irradiation. Hence, the behavior of iron-based and cerium-based materials can be studied using a general formulation for high temperature noncatalytic gas–solid reactions, although this work considers reactive porous structures composed only of ceria.

While the class of systems just described may seem very broad, it is actually outside the common chemical engineering uses of porous media in heterogeneous catalysis. There, the porous medium is used to offer a large surface area upon which gas phase reactants can more easily react, and temperatures are often sufficiently low as to minimize the importance of radiative heat transfer. Porous media combustion studies represent an important exception because in addition to the mass, momentum, and energy equations for the reacting flow, it is becoming more common to treat the solid phase as a participating medium and therefore include a source term in its energy equation that is obtained by solving the radiative transfer equation [43–49]. However, these systems feature a chemically inert solid phase, which makes their behavior significantly and fundamentally different from noncatalytic gas-solid reactions. Therefore, these studies will not be reviewed, but it is recognized that the methods developed for these problems inform some of the techniques used in this study.

Historically, studies of noncatalytic gas–solid reactions have been focused on the diffusion–reaction process occurring within a single particle and usually made a number of simplifications [50]. More recently, numerical methods have been used to obtain solutions for a wider class of behavior with some of these simplifications relaxed. Examples include studies of the transient behavior of a porous particle composed of grains with multiple gas–solid reactions [51] and the effects of different reaction orders and Thiele modulus values on conversion profiles [52].

A sophisticated approach to gas–solid reactions in packed beds has been performed by coupling the macroscale transport (which includes convection) to a pore-scale diffusion–reaction problem [51,53], but the treatment of radiation heat transfer is greatly simplified by relying on empirical correlations for an overall effective thermal conductivity. A more sophisticated heat transfer analysis was performed for the thermal decomposition of limestone driven by direct irradiation [54]. Monte Carlo ray tracing was used to determine the radiative heat flux incident on the bed of particles, whose internal heat transfer was treated with a thermal conductivity that included a component from a non-gray Rosseland diffusion approximation. Convective heat transfer losses at the boundaries were also included, but there was no discussion of mass transfer effects related to the transport of the carbon dioxide reaction product, although the reaction rate expression is not coupled to any mass transfer effects but rather depends upon only the temperature and reaction extent of the solid phase. Solar thermogravimetry experiments of a directly irradiated packed bed of ZnO particles have also been modeled using a thermal conductivity that is augmented by a radiative component for the internal heat transfer with convective and radiative losses at the boundary [55,56]. Here, the ablative nature of the thermal dissociation reaction occurring at the irradiated surface caused the packed bed to shrink. Mass transfer was not modeled, although the kinetic parameters that were obtained by fitting to the experimental data were found to depend on the argon mass flow rate that removed the reaction products from the sample cavity. A study of an indirectly irradiated reactor concept for the carbothermal reduction of ZnO also used a one-dimensional energy equation with no mass transfer modeling and a zero-order Arrhenius reaction rate expression to capture the behavior of the shrinking packed bed caused by the ablative nature of the reaction [57]. In contrast to these packed bed batch processes, a moving packed bed utilizing an incident radiative flux for gasifying coal has been modeled using a steady state one-dimensional formulation that included heat and mass transfer [58]. The model treats radiative heat transfer using the Rosseland diffusion approximation and features a momentum equation that seems very inappropriate because it does not include any terms representing the flow resistance from the solid phase, even though it appears to have captured the behavior of their experimental system.

10

The coupling of radiative heat transfer and a heterogeneous chemical system was studied in greater detail using steam gasification of an idealized coal particle suspension [59]. A sophisticated treatment of the radiative heat transfer was performed where Mie theory was used to update the radiative properties at each time step as the particles shrank during the course of reaction and the source term in the energy equation was obtained using a collision-based Monte Carlo technique. To focus on the radiation-chemistry interaction, all other heat and mass transfer processes were neglected. While a mass balance on the solid phase particles is performed, an analogous conservation principle for the gas phase does not appear despite the fact that the reaction rate expressions depend on the partial pressures of the various components. Hence, the coupling between the kinetics and mass transfer based on the reaction rate expressions was never realized. This quasi-continuous treatment of the particle suspension was compared to a discrete-particle formulation and found to be more computationally efficient as well as more accurate because the latter experiences greater stochastic errors from the Monte Carlo method for an equal number of rays [60]. A similar methodology was applied to a ZnO particle suspension (treated in a quasi-continuous manner) where Mie theory was used to update radiative properties while the radiative source term in the energy equation was obtained by a path-length Monte Carlo method [61]. Again, other modes of heat transfer were not included and there is no inclusion of mass transfer. In this work, the zero-order reaction rate expression that was used prevents any dependence on the gas phase composition, thereby eliminating any coupling between the kinetics and mass transfer. In these studies, the size of the medium was held fixed as the particle diameter decreased as a consequence of reaction.

It is worth noting that a partial redox cycle features chemistry that differs in an important way from the processes that have been previously modeled. The reduction of ZnO features a solid reactant evolving into gas phase products, while coal gasification features a solid and gas phase reactant combining to give gas phase products. A partial redox cycle features a thermal reduction process where a solid reactant is converted into a solid and gas phase product, while the oxidation features a solid and gas phase reactant combining to form a solid and gas phase product.

11

Recent studies of gas–solid reactions in a more general porous medium include a local thermal non-equilibrium treatment of a hydrogen/metal hydride reactor for a heat pump system [62] and a local thermal equilibrium treatment of the oxidative pyrolysis of wood including both heterogeneous and homogeneous chemical reactions [63]. Both of these studies are one-dimensional, use Darcy's law for their momentum equation, and do not consider radiative heat transfer.

It was mentioned in the previous section that multiple reactor concepts based on partial redox thermochemical cycles have been tested. However, it appears as though modeling attempts have only been made for the ceramic honeycomb monolith structures coated with redox active materials [64]. The analysis is based on a one-dimensional treatment of laminar flow with surface sorption and reaction occurring along the axial dimension of a single honeycomb channel. The heat transfer formulation uses the solid phase axial boundary condition to absorb the concentrated solar irradiation, after which only axial conduction along the wall and convection with the fluid are considered. This is a unique approach because it is a (simplified) pore-scale analysis and is not possible for a more general morphology.

In summary, prior studies of gas–solid reactions featuring sophisticated heat transfer analyses generally simplify the chemistry and mass transfer, while those with a more complicated chemical reaction network simplify the heat transfer analysis. In order to explore the concept of effectively accomplishing a solar-driven partial redox thermochemical cycle by forming the metal oxide into a porous structure, both the heat and mass transfer must be properly modeled. In light of the absence of modeling efforts fitting this description, this research will explore the behavior of these systems in order to understand and optimize the interactions of the transport processes with the chemical kinetics.

Chapter 3

A Model of Transient Heat and Mass Transfer in a Heterogeneous Medium of Ceria Undergoing Nonstoichiometric Reduction[2]

The redox chemistry of nonstoichiometric metal oxides can be used to produce chemical fuels by harnessing concentrated solar energy to split water and/or carbon dioxide. In such a process, it is desirable to use a porous reactive substrate for increased surface area and improved gas transport. The present study develops a macroscopic-scale model of porous ceria undergoing thermal reduction. The model captures the coupled interactions between the heat and mass transfer and the heterogeneous chemistry using a local thermal non-equilibrium (LTNE) formulation of the volume averaged conservation of mass and energy equations in an axisymmetric cylindrical domain. The results of a representative test case simulation demonstrate strong coupling between gas phase mass transfer and the chemical kinetics as well as the pronounced impact of optical thickness on the temperature distribution and thus global solar-to-chemical energy conversion.

Introduction

Cerium dioxide (ceria) has been identified as a promising metal oxide to realize solar-driven redox cycles that produce the components of synthesis gas, H_2 and CO, via H_2O and CO_2 splitting [17,18,26,40,41,65]. The two-step nonstoichiometric cycle consists of a high-temperature endothermic reduction step, in which concentrated solar radiation is used as the exclusive source of process heat, and a low-temperature exothermic oxidation step. The net result is the splitting of water or carbon dioxide.

Solar step: $$CeO_2(s) \rightarrow CeO_{2-\delta}(s) + \frac{\delta}{2}O_2(g) \qquad (3.1)$$

---
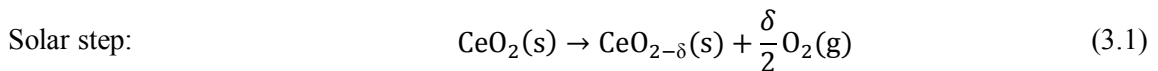
[2] This chapter is based on the article Keene D. J., Davidson J. H., and Lipiński W., 2013, "A Model of Transient Heat and Mass Transfer in a Heterogeneous Medium of Ceria Undergoing Nonstoichiometric Reduction," Journal of Heat Transfer, **135**(5), p. 052701.

Non-solar step:

$$\delta H_2O(g) + CeO_{2-\delta}(s) \rightarrow CeO_2(s) + \delta H_2(g)$$

or   (3.2)

$$\delta CO_2(g) + CeO_{2-\delta}(s) \rightarrow CeO_2(s) + \delta CO(g)$$

Net cycle:

$$\delta H_2O(g) \rightarrow \delta H_2(g) + \frac{\delta}{2}O_2(g)$$

or   (3.3)

$$\delta CO_2(g) \rightarrow \delta CO(g) + \frac{\delta}{2}O_2(g)$$
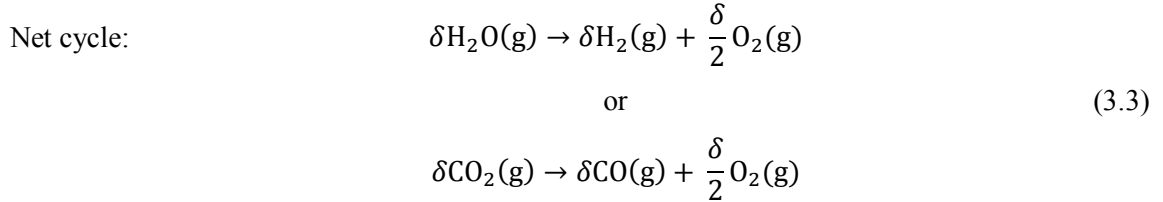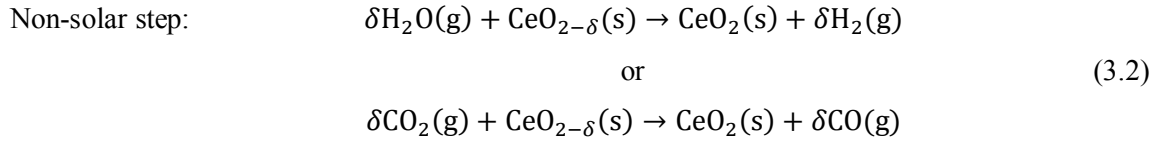
A promising approach for implementing ceria in a solar reactor is to form the reactive material into a porous structure that simultaneously serves as an effective radiant absorber and provides high specific surface area for promoting rapid solid-gas reactions [32,35,41]. Direct absorption of external radiation at the reaction site has the potential to decrease temperature gradients and consequently utilize the reactive medium more uniformly by overcoming heat transfer limitations. By modifying the structure morphology, its heat and mass transfer characteristics can be tailored for achieving a desired thermochemical response. Understanding the transport phenomena in the reactive medium and identifying a geometry that allows for maximum conversion of heat into chemical energy is crucial to the design of an efficient solar reactor realizing cycle (3.1)–(3.2).

In this paper, we focus on the development of a transient analysis and model of heat and mass transfer as reaction (3.1) occurs in a porous ceria medium exposed to direct high-flux irradiation and present a representative test case to demonstrate the model. An expression for the reaction rate is formulated to capture the influence of temperature, nonstoichiometry, and gas phase composition. Conservation equations are derived by applying the volume averaging theory [66] to the two-phase reactive medium for the conditions of local thermal non-equilibrium (LTNE) and then solved numerically to obtain the macroscale behavior. The results obtained for the representative test case are

presented to illustrate the coupling between the transport processes and the chemical reaction occurring as the evolved gas product is removed with a sweeping gas.

Problem Statement

The coupled heat and mass transfer processes of the nonstoichiometric reduction reaction (3.1) are modeled for a representative test case using a stationary axisymmetric cylindrical domain as shown in Fig. 3.1. The heterogeneous medium is modeled as a continuum and assumed to be homogeneous, isotropic and dimensionally stable at the macroscopic level. The input parameter values for the representative test case are listed in Table 3.1.

The medium is exposed to an external concentrated radiative heat flux at the boundary. The concentration ratio is set to 1000 suns, which is sufficient in the test case to reach the temperatures required by the endothermic reaction. The surroundings are assumed cold and black. A sweeping gas consisting of argon with a very small amount of oxygen enters the porous medium at $z = 0$. The primary motivation for having the gas flow through the porous medium is to remove the oxygen that is released from the solid by sweeping it downstream. One requirement for performing this task is that the gas flow residence time must be shorter than the time scale for axial oxygen mass diffusion. The inlet flow rate is selected based on satisfying this criterion without requiring copious amounts of sweeping gas while the outlet pressure is selected to be atmospheric. The oxygen content of the sweeping gas ($Y_{O_2,\infty} = 7.8039 \times 10^{-6}$) is chosen to obtain nonstoichiometries sufficiently high for fuel production ($\delta \approx 0.1$) while maintaining temperatures below 2000 K. The sweeping gas temperature is assumed to be equal to the operating temperature for the fuel production step as it can be realized in a solar reactor implementing gas phase heat recovery. The lateral boundary ($r = R$) is assumed to be impermeable to mass transfer and adiabatic, while the outlet boundary ($z = L$) is assumed to be adiabatic. The total mass flux, species mass flux, and heat flux associated with the sweep gas entering the domain are specified as shown in Fig. 3.2.

The two-phase medium consists of a radiatively participating solid phase and an assumed radiatively non-participating gas phase. Due to the large extinction coefficient of

15

porous ceria structures [36–38,67], and consequently large optical thickness of the medium, the Rosseland diffusion approximation is used for the internal radiative heat transfer. Implementing this approximation requires surface radiative properties at the irradiated boundary, which are selected by treating the surface as black.

The mass diffusion coefficient is calculated using Chapman–Enskog theory [68], while the intrinsic viscosity and thermal conductivity for the fluid mixture are obtained using a mixing rule that uses the mole fraction as a weighting function for the pure species values:

$$\mu_f = \sum_{i=1}^{N} X_i \mu_i \qquad (3.4)$$

$$k_f = \sum_{i=1}^{N} X_i k_i \qquad (3.5)$$

The species viscosities, thermal conductivities, and specific heats are evaluated as functions of temperature [69,70]. For oxygen, viscosity data are available only for temperatures up to 1500 K; at higher temperatures the value at 1500 K is taken. For the solid, the specific heat and thermal conductivity are evaluated as functions of temperature [70,71].

Analysis

The numerical heat and mass transfer analysis of the reacting heterogeneous medium is based on volume-averaged mass and energy conservation equations that couple radiative, conductive and convective heat transfer modes as well as the advection and diffusion of mass with the chemical kinetics. The volume-averaged equations render the pore-level transport phenomena through effective properties that arise from the averaging process so that the macroscale behavior captures the influence of the morphology.

Chemical Kinetics

The heterogeneous reaction causes interphase mass transfer, which manifests as a source term for the conservation of mass equations and an associated interphase enthalpy

transfer source term in the conservation of energy equations. An important subtlety is that the interphase enthalpy flux must be considered in conjunction with the solid enthalpy when allocating the energy requirements of the chemical reaction between the two phases, which becomes an intricate task due to the LTNE treatment.

In developing the reaction rate expression, it is critical to incorporate both O_2 release and O_2 uptake because chemical equilibrium during the nonstoichiometric reduction of ceria depends strongly on the temperature and oxygen partial pressure. The uptake and release of an oxygen atom from the solid can be described at the lattice level using Kröger–Vink notation [72] as

$$2Ce'_{Ce} + V_O^{\cdot\cdot} + \frac{1}{2}O_2(g) \leftrightarrow 2Ce_{Ce}^X + O_O^X \tag{3.6}$$
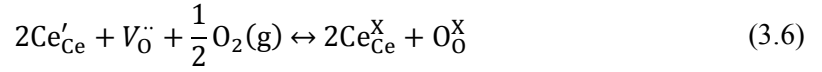
Equation (3.6) assumes the oxygen vacancy ($V_O^{\cdot\cdot}$) to be doubly ionized so that there are two cerium atoms in their 3+ oxidation state ($2Ce'_{Ce}$) per released oxygen atom, which is the prevailing explanation of nonstoichiometric defects in the literature [72]. Equation (3.6) can be used as a basis for defining an equilibrium constant in the same manner as has been done for samarium-doped ceria [18], which yields

$$K_{KV} = \exp\left(-\frac{\Delta\bar{h}_{KV}^0 - T\Delta\bar{s}_{KV}^0}{\bar{R}T}\right) = \frac{[Ce_{Ce}^X]^2[O_O^X]}{\left(\frac{p_{O_2}}{p_{ref}}\right)^{1/2}[Ce'_{Ce}]^2[V_O^{\cdot\cdot}]} \tag{3.7}$$

where p_{ref} = 1 atm. Applying electroneutrality and crystal site conservation, the equilibrium constant is expressed as a function of the nonstoichiometry according to

$$K_{KV} = \exp\left(-\frac{\Delta\bar{h}_{KV}^0 - T\Delta\bar{s}_{KV}^0}{\bar{R}T}\right) = \frac{(1-2\delta)^2(1-0.5\delta)}{\left(\frac{p_{O_2}}{p_{ref}}\right)^{\frac{1}{2}}(4\delta^2)(0.5\delta)} \tag{3.8}$$

17

which is used to construct a reaction rate in accordance with the law of mass action assumption,

$$\dot{m}''_{\text{sf},O_2} = M_{O_2} \frac{\dot{n}''_{\text{sf},0}}{2} \left\{ \frac{(1 - 2\delta)^2(1 - 0.5\delta)}{2K_{\text{KV}}} - \left(\frac{p_{O_2}}{p_{\text{ref}}}\right)^{\frac{1}{2}} \delta^3 \right\} \tag{3.9}$$

The thermodynamic data for the release and uptake of oxygen from ceria are reported in the literature using slightly different enthalpy and entropy changes defined by

$$\Delta \bar{h}^0_{O_2} - T\Delta \bar{s}^0_{O_2} = \bar{R}T\ln\left(\frac{p_{O_2}}{p_{\text{ref}}}\right) \tag{3.10}$$

Combining Eqs. (3.8) and (3.10), substituting the result in Eq. (3.9), and evaluating the resulting reaction rate using the volume-averaged solid temperature, nonstoichiometry, and oxygen partial pressure yields

$$\dot{m}''_{\text{sf},O_2} = M_{O_2} \frac{\dot{n}''_{\text{sf},0}}{2} \left\{ \exp\left(\frac{1}{2}\frac{\Delta \bar{h}^0_{O_2} - \langle T_s\rangle^s \Delta \bar{s}^0_{O_2}}{\bar{R}\langle T_s\rangle^s}\right)(\langle\delta\rangle^s)^3 - \left(\frac{\langle p_{O_2}\rangle^f}{p_{\text{ref}}}\right)^{\frac{1}{2}}(\langle\delta\rangle^s)^3 \right\} \tag{3.11}$$

It is important to recognize that the thermodynamic functions appearing in Eq. (3.11) have been measured for ceria in the range $0.001 \leq \delta \leq 0.27$ and found to depend solely on nonstoichiometry throughout the entire temperature range ($1023 \text{ K} \leq T \leq 1773 \text{ K}$) [72]. Thus, evaluating $\Delta \bar{h}^0_{O_2}$ and $\Delta \bar{s}^0_{O_2}$ using the existing data at temperatures above 1773 K is anticipated to be a reasonable extrapolation provided the nonstoichiometry remains below a value of 0.27.

With the interphase mass flux defined by Eq. (3.11), the related interphase enthalpy flux can be calculated at a specified temperature. The temperature is selected by upwinding; oxygen that is driven from the solid by the forward reaction enters the fluid

phase at the solid temperature whereas oxygen that is driven into the solid by the backward reaction enters the solid phase at the fluid temperature. This approach yields

$$\dot{m}''_{\text{sf},O_2} h_{O_2,\text{sf}} = \frac{M_{O_2}}{2} \dot{n}''_{\text{sf},0} \left\{ \exp\left(\frac{1}{2} \frac{\Delta \bar{h}^0_{O_2} - \langle T_s \rangle^s \Delta \bar{s}^0_{O_2}}{\bar{R} \langle T_s \rangle^s} \right) (\langle \delta \rangle^s)^3 h_{O_2}|_{\langle T_s \rangle^s} \right.$$

$$\left. - \left(\frac{\langle p_{O_2} \rangle^f}{p_{\text{ref}}} \right)^{\frac{1}{2}} (\langle \delta \rangle^s)^3 h_{O_2}|_{\langle T_f \rangle^f} \right\} \qquad (3.12)$$

The enthalpy of nonstoichiometric ceria is evaluated according to

$$\bar{h}_{\text{CeO}_{2-\delta}}|_{T_s} = \bar{h}_{\text{form,CeO}_2}|_{T_{\text{ref}}} + \int_{T_{\text{ref}}}^{T_s} \bar{c}_{p,\text{CeO}_2} dT + \Delta \bar{h}_{\text{red}} - \frac{\delta}{2} \bar{h}_{O_2}|_{T_s} \qquad (3.13)$$

where $\bar{h}_{\text{form,CeO}_2}|_{T_{\text{ref}}}$ is the molar enthalpy of formation for cerium dioxide at the reference temperature T_{ref} and the enthalpy of reduction is defined as

$$\Delta \bar{h}_{\text{red}} = \bar{h}_{\text{CeO}_{2-\delta}} + \frac{\delta}{2} \bar{h}_{O_2} - \bar{h}_{\text{CeO}_2} \qquad (3.14)$$

and can be evaluated from the standard oxidation enthalpy change data using

$$\Delta \bar{h}_{\text{red}} = -\frac{1}{2} \int_0^\delta \Delta \bar{h}^0_{O_2} d\delta' \qquad (3.15)$$

Mass Conservation

The interphase mass transfer appears as a sink for the solid phase conservation of mass

$$\frac{\partial}{\partial t}\{(1-\phi)\langle\rho_s\rangle^s\} = -\dot{m}''_{\text{sf,O}_2}a_{\text{sf}} \qquad (3.16)$$

where $\dot{m}''_{\text{sf,O}_2}$ is the interphase oxygen flux given by Eq. (3.11). The level of oxygen vacancies, characterized by the nonstoichiometry δ is related to the solid density according to

$$\langle\rho_s\rangle^s = \rho_{\text{CeO}_2}\left(1 - \langle\delta\rangle^s\frac{M_\text{O}}{M_{\text{CeO}_2}}\right) \qquad (3.17)$$

where it has been assumed that the unit cell size does not change with δ. Substituting Eqs. (3.11) and (3.17) into Eq. (3.16) and neglecting thermal expansion, the mass conservation equation for the solid phase is used to solve directly for the nonstoichiometry,

$$\frac{\partial}{\partial t}\left\{\frac{\rho_{\text{CeO}_2}}{M_{\text{CeO}_2}}(1-\phi)\langle\delta\rangle^s\right\} =$$
$$\dot{n}''_{\text{sf,0}}a_{\text{sf}}\left\{\exp\left(\frac{1}{2}\frac{\Delta\bar{h}^0_{\text{O}_2} - \langle T_s\rangle^s\Delta\bar{s}^0_{\text{O}_2}}{\bar{R}\langle T_s\rangle^s}\right)(\langle\delta\rangle^s)^3 - \left(\frac{\langle p_{\text{O}_2}\rangle^\text{f}}{p_{\text{ref}}}\right)^{\frac{1}{2}}(\langle\delta\rangle^s)^3\right\} \qquad (3.18)$$

Equation (3.18) contains no spatial derivatives because no mass fluxes are considered within the solid phase.

The mass conservation equation for the fluid phase is:

$$\frac{\partial}{\partial t}\left(\phi\langle\rho\rangle^\text{f}\right) + \nabla\cdot\left(\langle\rho\rangle^\text{f}\langle\vec{u}\rangle\right) = \dot{m}''_{\text{sf,O}_2}a_{\text{sf}} \qquad (3.19)$$

The ideal gas law for a multi-component mixture and Darcy's law are employed,

$$\langle p \rangle^{\mathrm{f}} = \left(\sum_{i=1}^{N} \frac{\langle Y_i \rangle^{\mathrm{f}}}{M_i} \right) \langle \rho \rangle^{\mathrm{f}} \bar{R} \langle T_{\mathrm{f}} \rangle^{\mathrm{f}} \tag{3.20}$$

$$-\nabla \left(\phi \langle p \rangle^{\mathrm{f}} \right) = \frac{\mu_{\mathrm{f}} \phi \langle \vec{u} \rangle}{K} \tag{3.21}$$

and substituted into Eq. (3.19), which transforms it into an equation for the pressure,

$$\frac{\partial}{\partial t} \left\{ \frac{\phi}{\left(\sum_{i=1}^{N} \frac{\langle Y_i \rangle^{\mathrm{f}}}{M_i} \right) \bar{R} \langle T_{\mathrm{f}} \rangle^{\mathrm{f}}} \langle p \rangle^{\mathrm{f}} \right\}$$
$$= \nabla \cdot \left\{ \frac{\frac{K}{\mu_{\mathrm{f}} \phi}}{\left(\sum_{i=1}^{N} \frac{\langle Y_i \rangle^{\mathrm{f}}}{M_i} \right) \bar{R} \langle T_{\mathrm{f}} \rangle^{\mathrm{f}}} \langle p \rangle^{\mathrm{f}} \nabla \left(\phi \langle p \rangle^{\mathrm{f}} \right) \right\} + \dot{m}''_{\mathrm{sf},O_2} a_{\mathrm{sf}} \tag{3.22}$$

The oxygen mass fraction in the fluid phase—a binary mixture of argon and oxygen—is obtained by solving the species mass conservation equation

$$\frac{\partial}{\partial t} \left(\phi \langle \rho \rangle^{\mathrm{f}} \langle Y_{O_2} \rangle^{\mathrm{f}} \right) + \nabla \cdot \left(\langle \rho \rangle^{\mathrm{f}} \langle \vec{u} \rangle \langle Y_{O_2} \rangle^{\mathrm{f}} \right)$$
$$= \nabla \cdot \left(D_{O_2,\mathrm{eff}} \langle \rho \rangle^{\mathrm{f}} \nabla \langle Y_{O_2} \rangle^{\mathrm{f}} \right) + \dot{m}''_{\mathrm{sf},O_2} a_{\mathrm{sf}} \tag{3.23}$$

Then, the argon mass fraction is calculated using

$$\langle Y_{\mathrm{Ar}} \rangle^{\mathrm{f}} = 1 - \langle Y_{O_2} \rangle^{\mathrm{f}} \tag{3.24}$$

Energy Conservation

Because the LTNE formulation is used, separate energy equations are required for the solid and fluid phases. For the solid phase, the energy equation reads:

$$\frac{\partial}{\partial t}\{(1-\phi)\langle\rho_s\rangle^s\langle h_s\rangle^s\} = \nabla \cdot \left(k_{s,eff} \nabla\langle T_s\rangle^s\right) - \langle\nabla \cdot \vec{q}''_{rad}\rangle$$
$$-\dot{m}''_{sf,O_2}a_{sf}h_{O_2,sf} - h_{sf}a_{sf}\left(\langle T_s\rangle^s - \langle T_f\rangle^f\right) \quad (3.25)$$

where the term on the left hand side represents the change in enthalpy of the solid phase, given by Eq. (3.13), and the terms on the right hand side represent conduction, radiation, interphase enthalpy transfer (due to chemical reaction), and interphase convective heat transfer (due to LTNE). The radiative source term is quantified by employing the Rosseland diffusion approximation [73]:

$$\vec{q}''_{rad} = -\frac{16n^2\sigma(\langle T_s\rangle^s)^3}{3\beta_m^{tr}}\nabla\langle T_s\rangle^s \quad (3.26)$$

The fluid-phase energy conservation equation is given by

$$\frac{\partial}{\partial t}\left(\phi\langle\rho\rangle^f\sum_{i=1}^{N}\langle Y_i\rangle^f\langle h_i\rangle^f\right) + \nabla \cdot \left(\langle\rho\rangle^f\langle\vec{u}\rangle\sum_{i=1}^{N}\langle Y_i\rangle^f\langle h_i\rangle^f\right)$$
$$= \nabla \cdot \left(\langle\rho\rangle^f\sum_{i=1}^{N}\langle h_i\rangle^f D_{i,eff}\nabla\langle Y_i\rangle^f\right) + \nabla \cdot \left(k_{f,eff}\nabla\langle T_f\rangle^f\right) \quad (3.27)$$
$$+ \dot{m}''_{sf,O_2}a_{sf}h_{O_2,sf} + h_{sf}a_{sf}\left(\langle T_s\rangle^s - \langle T_f\rangle^f\right)$$

where the left hand side captures how the energy can be stored and convected through the medium while the right hand side includes the enthalpy transfer associated with mass diffusion, conduction, interphase enthalpy transfer (due to chemical reaction), and interphase convective heat transfer (due to LTNE).

Boundary and Initial Conditions

The boundary conditions for Eqs. (3.22), (3.23), (3.25), and (3.27) are summarized in Fig. 3.2. The inlet boundary conditions for the conservation of mass, species mass, and fluid energy equations are based on the assumption that the volume located immediately upstream of the solution domain is quasi-steady so that the flux entering the solution

domain is equal to the advective flux "far upstream." The boundary condition at $r = R$ has been formulated so that each phase can experience a non-zero radial heat flux. The boundary temperature (which depends on axial position) influences these fluxes, and its value must be computed as part of the solution so that the fluxes balance to satisfy the adiabatic condition. A consequence of this approach is that local thermal equilibrium is enforced at the $r = R$ boundary.

The initial conditions for Eqs. (3.18), (3.22), (3.23), (3.25), and (3.27) are summarized in Table 3.2, where the pressure and velocity distributions are expressed in the more compact form shown by introducing $p_0^2 = p_L^2 + \frac{2\mu L}{K}(\rho u_z)_\infty \left(\sum_i \frac{Y_{i,\infty}}{M_i}\right)\bar{R}T_{f,\infty}$. The initial conditions are obtained as a steady state analytical solution to the set of governing equations with no chemical reaction and an adiabatic solid phase boundary at $z = 0$. All field variables are obtained analytically except for the nonstoichiometry, whose value is set according to chemical equilibrium based on the local temperature and oxygen partial pressure.

Effective Transport Properties

The effective transport properties that appear in the volume-averaged equations are obtained using intrinsic transport properties and morphology-dependent parameters as listed in Table 3.3. The permeability is calculated based on the hydraulic radius approach. Because the Kozeny constant k_K has been found to be a weak function of morphology [74], the permeability is influenced primarily by the porosity and specific surface area. This result is advantageous because it allows purely geometric quantities to characterize the influence of morphology on permeability. The tortuosity for mass diffusion is taken as unity. The interphase heat transfer coefficient is calculated using the empirical correlation for packed beds [75]

$$\text{Nu}_{\text{pore}} = 2 + 1.1\left(\frac{\langle\rho\rangle^f\langle|\vec{u}|\rangle d_{32}}{\mu}\right)^{0.6}\text{Pr}^{1/3} \tag{3.28}$$

The expressions used to evaluate the effective thermal conductivities warrant discussion because they differ from those most commonly used when allowing for LTNE. In the LTNE context, the effective thermal conductivity of a phase is commonly computed as the product of its intrinsic thermal conductivity and volume fraction, which allows the effective thermal conductivity of each phase to be calculated with no dependence on the other phases present. This approach is equivalent to setting the closure term to zero, which is where the expressions used in the present study differ, as will now be shown.

When the net conductive flux term in the governing fluid and solid energy equations are averaged over an entire REV (representative elementary volume), they become

$$\nabla \cdot \left(k_{\mathrm{f,eff}} \, \nabla \langle T_{\mathrm{f}} \rangle^{\mathrm{f}} \right) \equiv \nabla \cdot \langle k_{\mathrm{f}} \nabla T_{\mathrm{f}} \rangle$$
$$= \nabla \cdot \left(\phi \langle k_{\mathrm{f}} \rangle^{\mathrm{f}} \nabla \langle T_{\mathrm{f}} \rangle^{\mathrm{f}} \right) - \nabla \cdot \left(\frac{\langle k_{\mathrm{f}} \rangle^{\mathrm{f}}}{V} \int_{\partial V_{\mathrm{f}}} T_{\mathrm{f}} \hat{n}_{\mathrm{sf}} dS \right) \tag{3.29}$$

$$\nabla \cdot \left(k_{\mathrm{s,eff}} \, \nabla \langle T_{\mathrm{s}} \rangle^{\mathrm{s}} \right) \equiv \nabla \cdot \langle k_{\mathrm{s}} \nabla T_{\mathrm{s}} \rangle$$
$$= \nabla \cdot \{ (1 - \phi) \langle k_{\mathrm{s}} \rangle^{\mathrm{s}} \nabla \langle T_{\mathrm{s}} \rangle^{\mathrm{s}} \} + \nabla \cdot \left(\frac{\langle k_{\mathrm{s}} \rangle^{\mathrm{s}}}{V} \int_{\partial V_{\mathrm{s}}} T_{\mathrm{s}} \hat{n}_{\mathrm{sf}} dS \right) \tag{3.30}$$

Rather than setting the closure terms (second terms on RHS) to zero as is commonly done, the present study seeks to include them. This inclusion is accomplished by adding Eqs. (3.29) and (3.30) to obtain

$$\nabla \cdot \left(k_{\mathrm{s,eff}} \, \nabla \langle T_{\mathrm{s}} \rangle^{\mathrm{s}} \right) + \nabla \cdot \left(k_{\mathrm{f,eff}} \, \nabla \langle T_{\mathrm{f}} \rangle^{\mathrm{f}} \right)$$
$$= \nabla \cdot \{ (1 - \phi) \langle k_{\mathrm{s}} \rangle^{\mathrm{s}} \nabla \langle T_{\mathrm{s}} \rangle^{\mathrm{s}} \} + \nabla \cdot \left(\phi \langle k_{\mathrm{f}} \rangle^{\mathrm{f}} \nabla \langle T_{\mathrm{f}} \rangle^{\mathrm{f}} \right)$$
$$+ \nabla \cdot \left(\frac{\langle k_{\mathrm{s}} \rangle^{\mathrm{s}} - \langle k_{\mathrm{f}} \rangle^{\mathrm{f}}}{V} \int_{\partial V_{\mathrm{s}}} T \hat{n}_{\mathrm{sf}} dS \right) \tag{3.31}$$

where Eq. (3.31) has made use of the fact that ∂V_{s} and ∂V_{f} correspond to the same surface, and so the subscript on the temperature appearing in the integrand can be

dropped. Recognizing that $\langle T_s \rangle^s = \langle T_f \rangle^f \equiv \langle T \rangle$ for LTE, the net conductive flux described by Eq. (3.31) leads to the definition of the stagnant thermal conductivity as

$$
\nabla \cdot \left(k_{\mathrm{stag}} \nabla \langle T \rangle \right) = \nabla \cdot \{(1 - \phi)\langle k_s \rangle^s \nabla \langle T \rangle\} + \nabla \cdot \left(\phi \langle k_f \rangle^f \nabla \langle T \rangle \right)
$$
$$
+ \nabla \cdot \left(\frac{\langle k_s \rangle^s - \langle k_f \rangle^f}{V} \int_{\partial V_s} T \hat{n}_{sf} dS \right)
\tag{3.32}
$$

which allows the surface integral to be calculated as

$$
\frac{1}{V} \int_{\partial V_s} T \hat{n}_{sf} dS = \frac{k_{\mathrm{stag}} - (1 - \phi)\langle k_s \rangle^s - \phi \langle k_f \rangle^f}{\langle k_s \rangle^s - \langle k_f \rangle^f} \nabla \langle T \rangle
\tag{3.33}
$$

Then, the expressions for the effective thermal conductivity of each phase are obtained by inserting Eq. (3.33) into Eqs. (3.29) and (3.30), yielding

$$
k_{\mathrm{f,eff}} = \phi \langle k_f \rangle^f - \frac{\langle k_f \rangle^f}{\langle k_s \rangle^s - \langle k_f \rangle^f} \left(k_{\mathrm{stag}} - (1 - \phi)\langle k_s \rangle^s - \phi \langle k_f \rangle^f \right)
\tag{3.34}
$$

$$
k_{\mathrm{s,eff}} = (1 - \phi)\langle k_s \rangle^s + \frac{\langle k_s \rangle^s}{\langle k_s \rangle^s - \langle k_f \rangle^f} \left(k_{\mathrm{stag}} - (1 - \phi)\langle k_s \rangle^s - \phi \langle k_f \rangle^f \right)
\tag{3.35}
$$

Equations (3.34) and (3.35) are equivalent to the relationships that result from using the independently developed concept of an effective porosity that has recently been presented in [76]. Making use of Eq. (3.33) to evaluate the surface integrals in an LTNE problem is an admittedly heuristic extension, but this approach is preferred to setting the surface integrals to zero. For an LTE problem described by Eq. (32), setting the surface integrals equal to zero always leads to the parallel conduction model corresponding to the upper bound on the stagnant thermal conductivity. In contrast, reducing an LTNE problem to an LTE one by adding Eqs. (3.34) and (3.35) preserves any presumed form of the stagnant thermal conductivity. In this study, the stagnant thermal conductivity is estimated using the geometric mean given by

$$k_{\text{stag}} = (\langle k_{\text{s}}\rangle^{\text{s}})^{1-\phi}\big(\langle k_{\text{f}}\rangle^{\text{f}}\big)^{\phi} \tag{3.36}$$

The extinction coefficient of the porous ceria is estimated using the geometric optics limit of Mie theory in conjunction with the transport approximation modification to scattering to obtain $\beta_{\text{m}}^{\text{tr}} = \frac{3(1-\phi)}{d_{32}}(1 - g\omega)$ where g is the asymmetry factor associated with the scattering phase function and ω is the (ordinary) scattering albedo, which for the particle diameter of $d_{32} = 100\,\mu m$ have been set to 0.8 and 0.6, respectively. The extinction coefficient value obtained from this calculation does not differ greatly from estimates based on experimental measurements [36,37], and a similar application of Mie theory has recently been found to agree rather well with experimental results for ceria porous structures [38,67].

The above relationships between the morphological and transport characteristics provide reasonable estimates for a broad class of morphologies whereas more sophisticated approaches (such as tomography-based techniques [39]) can be used to improve accuracy for a particular morphology.

Solution Method

The finite volume method is applied to discretize the governing equations in space [77,78]. The solutions are obtained on a structured cylindrical grid with 800 cells of constant length in the axial direction and 10 cells of constant radial size in the radial direction, using an in-house developed Fortran code. Using Darcy's law for the momentum equation allows velocity interpolation to be avoided entirely through the use of a staggered grid. Hence, velocity data are computed and stored directly at cell faces while all other field variables are computed and stored at cell centers. Linear interpolation (the central difference scheme) is used to compute the quantities required at cell faces based on their values at adjoining cell centers.

An implicit method is applied to accommodate the disparate times scales of the different processes by integrating the governing equations using a time step of 1×10^{-2} s for the duration of 2×10^{2} s. The implicit Euler method is used because it evaluates the fluxes and source terms using exclusively future time level data, which allows the action

of the source terms to be controlled through carefully constructed linearizations [78]. These linearizations are based on a nonlinear source term $S(\Phi)$ arising in a conservation equation for the dependent variable Φ being approximated at the future time level according to $S(\Phi^{n+1}) \approx S_C + S_P \Phi^{n+1}$. Care has been taken to enforce $S_C \geq 0$ and $S_P \leq 0$, which allows the positivity criterion associated with quantities such as mass fractions to be satisfied in an elegant and robust manner. Also, the formulae for S_C and S_P have been developed so that the linearization error $(S(\Phi^{n+1}) - S_C - S_P\Phi^{n+1})$ vanishes when Φ^{n+1} is used to evaluate S_C and S_P. This feature allows the evaluation of the nonlinear source term at the future time level to become exact by recomputing the values of S_C and S_P as new data become available during the iterative procedure.

The coupled nature of the governing equations is addressed by solving them sequentially, using Eqs. (3.18), (3.23), (3.25), (3.27), and (3.22) to update $\langle \delta \rangle^{\mathrm{s}}$, $\langle Y_{O_2} \rangle^{\mathrm{f}}$, $\langle T_{\mathrm{s}} \rangle^{\mathrm{s}}$, $\langle T_{\mathrm{f}} \rangle^{\mathrm{f}}$, and $\langle p \rangle^{\mathrm{f}}$, respectively. Due to the nature of the boundary conditions, the solution has a generally strong and weak dependence on the axial and radial coordinates, respectively. Consequently, the line Gauss–Seidel method is used to solve each equation, except for Eq. (3.18) as it contains no spatial derivatives. Equation (3.22) is used as a pressure correction equation to obtain the pressure from which both the density and velocity are calculated using Eqs. (3.21) and (3.20), respectively. Inner iterations are considered converged when the L^1 norm of the relative change in the dependent variable between two successive iterations is less than 10^{-8}. Outer iterations are considered converged when the L^1 norm of the relative changes in $\langle \delta \rangle^{\mathrm{s}}$, $\langle Y_{O_2} \rangle^{\mathrm{f}}$, $\langle T_{\mathrm{s}} \rangle^{\mathrm{s}}$, $\langle T_{\mathrm{f}} \rangle^{\mathrm{f}}$, and $\langle p \rangle^{\mathrm{f}}$ between two successive outer iterations are all less than 10^{-6}.

Accuracy Considerations

The magnitude of the discretization errors in the numerical results has been assessed through a systematic refinement of the grid and time step size. The discretization error associated with the radial grid spacing was investigated by altering the number of cells in the radial direction while keeping the number of cells in the axial direction and time step held at 100 and 10^{-2} s, respectively. The radial dependence of the solution is strongest near the lateral boundary close to the inlet. Consequently, the lateral boundary

temperature near the inlet $(T(r = R, z = 5 \times 10^{-5}\text{m}))$ was used to monitor the sensitivity to radial grid spacing. The boundary temperature was compared for 10, 20, 40, and 80 cells in the radial dimension at t = 200 s. This moment in time was chosen because it is when the magnitude of the LTNE is greatest, and so it is at this moment in time when the radial dependence is most pronounced that the solution should be most sensitive to the radial grid spacing. Comparing the boundary temperatures reveals that they have a monotonic convergence with a difference between the coarsest and finest grid of only 0.012%. The average nonstoichiometry value was also compared for each of these grids because it is a global quantity of great physical significance; the convergence behavior was similar and the difference between the coarsest and finest grid at t = 200 s was 0.035%.

The discretization error associated with the axial grid spacing was investigated by altering the number of cells in the axial direction while keeping the number of cells in the radial direction and time step held at 10 and 10^{-2} s, respectively. The axial boundary temperature of the solid phase at the centerline $(T_s(r = 0, z = 0))$ was used to monitor the sensitivity to axial grid spacing. This temperature was compared for 100, 200, 400, and 800 cells in the axial dimension at different moments in time. The greatest sensitivity was observed at early times, which is attributed to the steep gradients that exist as the surface is rapidly heated by the irradiation. The convergence had a strongly asymptotic character; the difference at t = 0.5 s between using 100 and 800 axial cells was 0.126% while the difference between using 400 and 800 cells was only 0.008%. Comparing the average nonstoichiometry on the different grids showed similar convergence trends; at t = 200 s (when the average nonstoichiometry is largest) the difference between using 100 and 800 axial cells was 1.73% while the difference between using 400 and 800 cells was 0.099%.

The temporal discretization error was investigated by altering the time step size while keeping the number of radial and axial cells held at 10 and 100, respectively. The average nonstoichiometry at different moments in time was compared for time step sizes of 10^{-2} s, 5×10^{-3} s, 2.5×10^{-3} s, and 1.25×10^{-3} s, and the convergence trend was found to perfectly follow the anticipated first order behavior. At t = 200 s, the difference between using a

time step of 10^{-2} s and 1.25×10^{-3} s was 0.00344% while the difference between using a time step of 2.5×10^{-3} s and 1.25×10^{-3} s was 0.00046%. Note that the difference between using the two smallest time steps is approaching the same order as the outer iteration convergence criterion.

Based on the trends in the average nonstoichiometry, these systematic grid and time step size refinement results suggest that the discretization error in the solution obtained using 10 cells in the radial dimension, 800 cells in the axial dimension, and a time step size of 10^{-2} s is on the order of 0.1% (in the 4th significant figure).

Results

Data obtained for the test case are presented to illustrate the ability of the model to capture the coupled heat and mass transfer and chemical processes. Global (domain integrated) quantities are considered first to provide an overview of the transient process. By integrating the sum of Eqs. (3.25) and (3.27) over the entire domain, the global energy budget is expressed as

$$\dot{Q}_{solar} = \dot{Q}_{solid} + \dot{Q}_{fluid} + \dot{Q}_{rerad} + \dot{Q}_{chem} \tag{3.37}$$

Figure 3.3 shows the quantities appearing on the right hand side of Eq. (3.37) as a function of time to elucidate how the solar power input is used throughout the thermal reduction process. Initially, nearly all of the solar input is used to heat the solid, but the reradiation loss quickly becomes significant. The primary reason for the significant energy loss by reradiation in the test case is the assumption of a relatively small concentration ratio of $C_0=1000$. However, decreasing the reradiation losses is not simply a matter of increasing the concentration ratio because operational upper limits on the solid temperature must be considered. It is beyond the scope of the present work to optimize the geometry of either the solar receiver/reactor or the morphology of the porous structure, but the results presented here point out the importance of ensuring penetration of the incident flux and reducing reradiation losses.

The energy used for sensibly heating the solid decreases as its temperature stabilizes and the chemical reaction begins to proceed at an appreciable rate. Only a small fraction of the solar input is used to drive the endothermic reaction because of the significant losses due to reradiation and sensible heating of the sweep gas. More generally, performance can be increased by reducing the reradiation loss and by implementing solid and/or gas phase heat recovery [65].

The solid experiences large axial temperature gradients due to the large optical thickness of the medium, $\beta_{\mathrm{m}}^{\mathrm{tr}} L = 39$. A comparison of the solid and fluid temperatures at the centerline $r = 0$ (Figs. 3.4a and 3.4b) shows that for the particular case studied, local thermal non-equilibrium exists in a region near the inlet where $z < 0.0005$ m ($z/L < 0.05$). The largest solid–fluid temperature differences are expected near the inlet because that is where the sweeping gas first comes into contact with the solid; the results indicate that interphase heat transfer is quite effective at eliminating local thermal non-equilibrium. Note that because the sweeping gas is continually introduced at a temperature below that of the solid, this region of LTNE near the inlet, although small, persists throughout the duration of the simulation. Furthermore, it is in this same region that a slight radial dependence exists due to the lateral wall boundary condition. As mentioned earlier, local thermal equilibrium is enforced at $r = R$, and so for $z/L < 0.05$, the solid and fluid temperatures differ from their centerline values in a small region near the wall. Because both the magnitude and extent of the radial dependence of the solution is small, only the centerline axial distributions are presented in Fig. 3.4.

For $t \leq 15$ s, all of the sensible energy that goes into heating the sweep gas near the inlet is used to heat the solid at downstream locations, as seen in Fig. 3.4b. This behavior explains the low energy loss due to heating the sweep gas at early times seen in Fig. 3.3. The convective heat transfer associated with the sweep gas continues to be significant for eliminating the axial temperature gradient at later times as well, but as the solid reaches higher temperatures, the amount of sensible energy that is carried out of the domain increases. Since the sweep gas is still being introduced at a low temperature, the sensible heating associated with removing it from the domain where it has attained the solid temperature causes an energy loss at later times, as seen in Fig. 3.3.

The axial gradients in nonstoichiometry shown in Fig. 3.4c indicate that the reduction reaction proceeds nonuniformly. The axial distributions of the oxygen partial pressure and the reaction rate (Figs. 3.4d and 3.4e) illustrate that the reaction begins near the inlet, where the oxygen partial pressure experiences its minimum due to the introduction of the sweep gas. The oxygen released by the solid is convected downstream, but the flow rate of the sweeping gas is insufficient to maintain the oxygen partial pressure throughout the domain equal to that at the inlet because of the rapid reaction. Consequently, the reaction rate attains a maximum near the inlet and then rapidly decreases within a short distance. As the nonstoichiometry approaches its equilibrium value near the inlet, the reaction begins to slow down, and the sweeping gas becomes more effective at maintaining low oxygen partial pressures at further downstream locations (as seen in Fig. 3.4d for $t > 12$ s). As the reaction zone travels downstream, it broadens as its peak value monotonically decreases. The upstream tail of the reaction zone exists because the reaction rate decreases as equilibrium is approached, whereas the downstream tail of the reaction zone exists because the streamwise accumulation of oxygen stifles the thermodynamic driving force.

Conclusion

Volume-averaged mass and energy conservation equations have been formulated and numerically solved to study the coupled transport and chemical processes in a directly-irradiated porous ceria structure undergoing nonstoichiometric thermal reduction. A reaction rate expression that depends on temperature, nonstoichiometry and gas phase composition (partial pressures) was developed to study the stiff chemical equilibrium of the nonstoichiometric reduction reaction.

The test case thermal reduction of ceria features a dynamic reaction zone due to chemistry-mass transfer coupling in the presence of a sweeping gas flow through the porous structure. This outcome highlights the importance of gas phase mass transfer whereas in the past, high-temperature thermal reduction processes were modeled as depending solely on temperature and thought to be heat transfer limited.

31

The model presented is well-suited to study heat and mass transfer phenomena in heterogeneous solid–gas reactions under the high-flux irradiation encountered in high-temperature solar thermochemical processing and a specific test case pertinent to nonstoichiometric redox cycles has been solved as a prelude to more extensive parametric studies.

Table 3.1. Input parameter values.

Parameter	Symbol	Value
radius of porous cylinder	R	5 mm
length of porous cylinder	L	10 mm
pore-scale feature size	d_{32}	100 μm
porosity	ϕ	0.75
Kozeny constant	k_K	5.0
cerium dioxide density	ρ_{CeO_2}	7215 kg m^{-3}
upstream total mass flux	$(\rho u_z)_\infty$	0.3 kg m^{-2} s^{-1}
upstream oxygen mass fraction	$Y_{O_2,\infty}$	7.8039×10^{-6}
upstream fluid temperature	$T_{f,\infty}$	1000 K
outlet pressure	p_L	1.01325×10^5 Pa
solar concentration ratio	C_0	1000
Planck-mean extinction coefficient	β_m^{tr}	3.9×10^3 m^{-1}
total hemispherical absorptivity at $z = 0$	α_0	1.0
total hemispherical emissivity at $z = 0$	ϵ_0	1.0
kinetic rate constant	$\dot{n}''_{sf,0}$	1.0 kmol$_O$ m^{-2} s^{-1}

Table 3.2. Initial conditions obtained from an analytical equilibrium solution.

Variable	Initial Value
pressure	$\dfrac{\langle p \rangle^{\mathrm{f}}}{p_0} = \left\{ 1 - \left(1 - \left(\dfrac{p_L}{p_0} \right)^2 \right) \dfrac{z}{L} \right\}^{1/2}$
oxygen mass fraction	$\dfrac{\langle Y_{O_2} \rangle^{\mathrm{f}}}{Y_{O_2,\infty}} = 1$
solid temperature	$\dfrac{\langle T_{\mathrm{s}} \rangle^{\mathrm{s}}}{T_{\mathrm{f},\infty}} = 1$
fluid temperature	$\dfrac{\langle T_{\mathrm{f}} \rangle^{\mathrm{f}}}{T_{\mathrm{f},\infty}} = 1$
nonstoichiometry	$\langle \delta \rangle^s = \delta_{\mathrm{eq}}(\langle T_{\mathrm{s}} \rangle^{\mathrm{s}}, \langle p_{O_2} \rangle^{\mathrm{f}})$
radial velocity	$\langle u_r \rangle = 0$
axial velocity	$\langle u_z \rangle = \dfrac{\dfrac{1}{2} \dfrac{K p_0}{\mu L} \left(1 - \left(\dfrac{p_L}{p_0} \right)^2 \right)}{\left\{ 1 - \left(1 - \left(\dfrac{p_L}{p_0} \right)^2 \right) \dfrac{z}{L} \right\}^{1/2}}$

Table 3.3. Morphology-dependent parameters arising in the macroscale transport model.

Parameter	Dependence
K	$K = \dfrac{\phi^3}{k_K a_{\text{sf}}^2}$
a_{sf}	$a_{\text{sf}} = \dfrac{1 - \phi}{d_{32}/6}$
$D_{i,\text{eff}}$	$D_{i,\text{eff}} = \phi D_i$
h_{sf}	$h_{\text{sf}} = \dfrac{k_{\text{f}}}{d_{32}} \text{Nu}_{\text{pore}}$
$k_{\text{f,eff}}$	See Eqs. (3.34) and (3.36)
$k_{\text{s,eff}}$	See Eqs. (3.35) and (3.36)
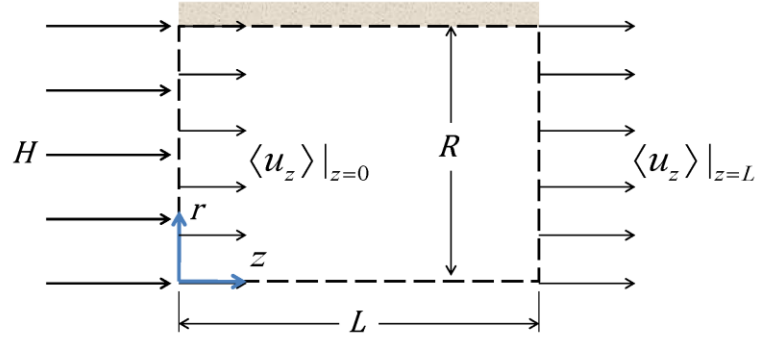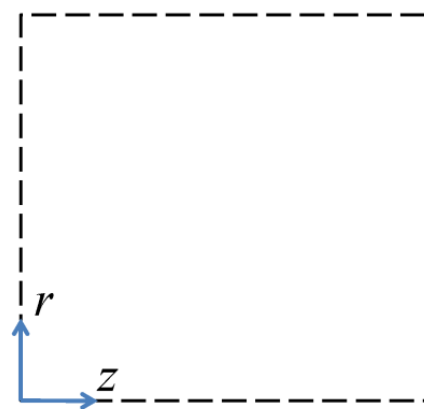
Fig. 3.1. Schematic of the axisymmetric cylindrical two-phase solid–gas reacting medium under direct irradiation.

$$-k_{\text{f,eff}} \left. \frac{\partial \langle T_{\text{f}} \rangle^{\text{f}}}{\partial r} \right|_{r=R} - (k_{\text{s,eff}} + k_{\text{rad}}) \left. \frac{\partial \langle T_{\text{s}} \rangle^{\text{s}}}{\partial r} \right|_{r=R} = 0$$

$$\left. \frac{\partial \langle p \rangle^{\text{f}}}{\partial r} \right|_{r=R} = \left. \frac{\partial \langle Y_{\text{O}_2} \rangle^{\text{f}}}{\partial r} \right|_{r=R} = 0$$

$$(\rho_{\text{f}} u_z)_\infty = \left. \left(\langle \rho_{\text{f}} \rangle^{\text{f}} \langle u_{\text{f},z} \rangle \right) \right|_{z=0}$$

$$\left. \langle p \rangle^{\text{f}} \right|_{z=L} = 0$$

$$(\rho_{\text{f}} u_z Y_i)_\infty = \left(\langle \rho_{\text{f}} \rangle^{\text{f}} \langle u_{\text{f},z} \rangle \langle Y_i \rangle^{\text{f}} - \langle \rho_{\text{f}} \rangle^{\text{f}} D_{i,\text{eff}} \frac{\partial \langle Y_i \rangle^{\text{f}}}{\partial z} \right) \Bigg|_{z=0}$$

$$\left. \frac{\partial \langle Y_{\text{O}_2} \rangle^{\text{f}}}{\partial z} \right|_{z=L} = 0$$

$$\left(\rho_{\text{f}} u_z \sum_i Y_i h_i \right)_\infty = \left(\begin{array}{c} \langle \rho_{\text{f}} \rangle^{\text{f}} \langle u_{\text{f},z} \rangle \sum_i \langle Y_i \rangle^{\text{f}} \langle h_i \rangle^{\text{f}} - k_{\text{f,eff}} \dfrac{\partial \langle T_{\text{f}} \rangle^{\text{f}}}{\partial z} \\[4mm] - \langle \rho_{\text{f}} \rangle^{\text{f}} \sum_i \langle h_i \rangle^{\text{f}} D_{i,\text{eff}} \dfrac{\partial \langle Y_i \rangle^{\text{f}}}{\partial z} \end{array} \right) \Bigg|_{z=0}$$

$$\left. \frac{\partial \langle T_{\text{f}} \rangle^{\text{f}}}{\partial z} \right|_{z=L} = 0$$

$$\left. \frac{\partial \langle T_{\text{s}} \rangle^{\text{s}}}{\partial z} \right|_{z=L} = 0$$

$$\alpha_0 C_0 H_{\text{solar}} = \left(\varepsilon_0 \sigma (\langle T_{\text{s}} \rangle^{\text{s}})^4 - (k_{\text{s,eff}} + k_{\text{rad}}) \frac{\partial \langle T_{\text{s}} \rangle^{\text{s}}}{\partial z} \right) \Bigg|_{z=0}$$

r

z

$$\left. \frac{\partial \langle p \rangle^{\text{f}}}{\partial r} \right|_{r=0} = \left. \frac{\partial \langle Y_{\text{O}_2} \rangle^{\text{f}}}{\partial r} \right|_{r=0} = 0$$

$$\left. \frac{\partial \langle T_{\text{f}} \rangle^{\text{f}}}{\partial r} \right|_{r=0} = \left. \frac{\partial \langle T_{\text{s}} \rangle^{\text{s}}}{\partial r} \right|_{r=0} = 0$$

Fig. 3.2. Boundary conditions for mass and energy equations (3.22), (3.23), (3.25), (3.27)

36
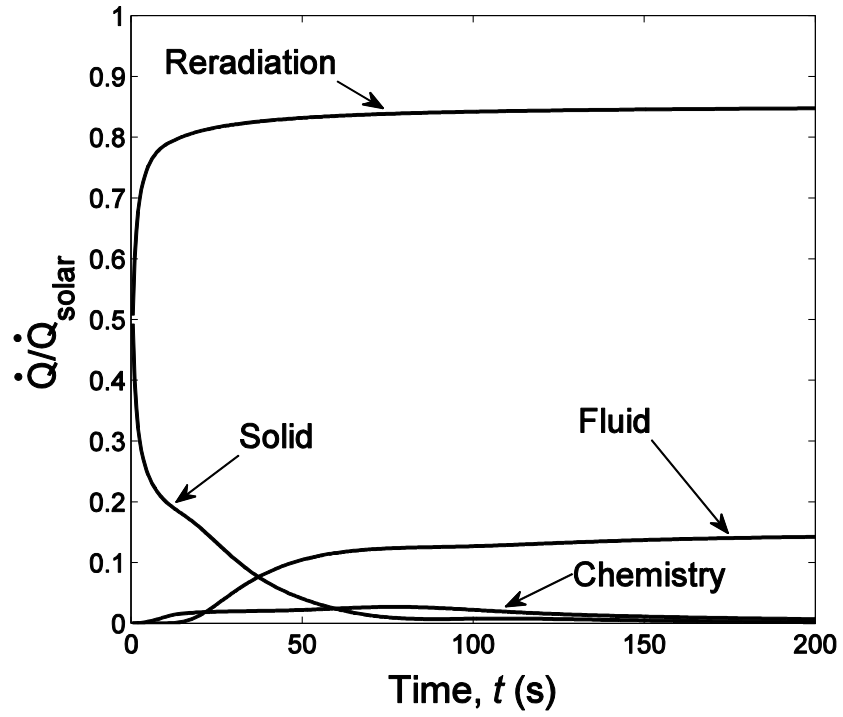
Fig. 3.3. Time evolution of the terms identified in the global energy balance described by Eq. (3.37).

(a)

(b)

(c)

(d)

39
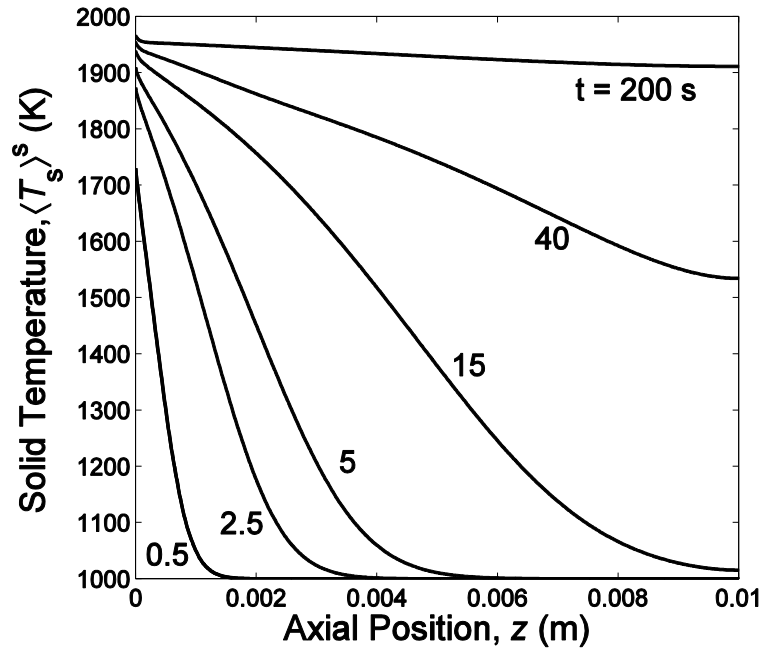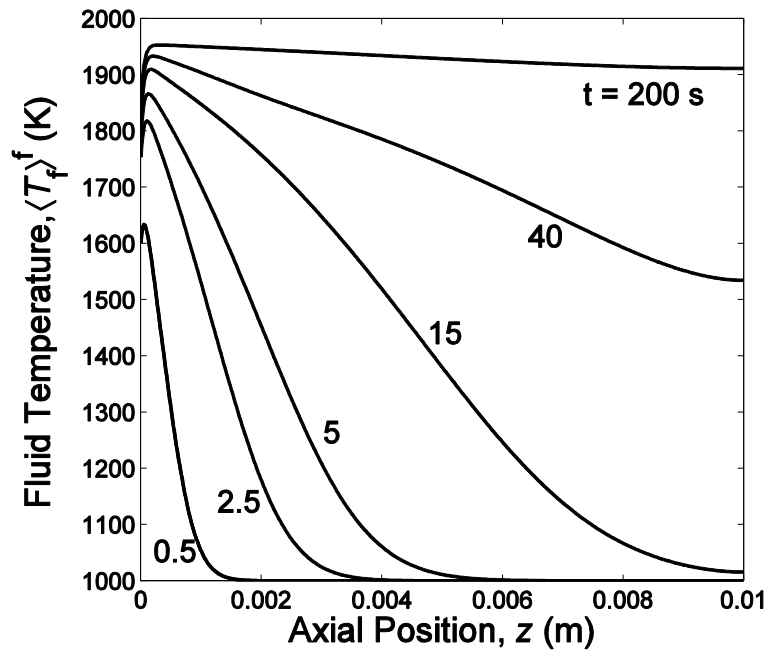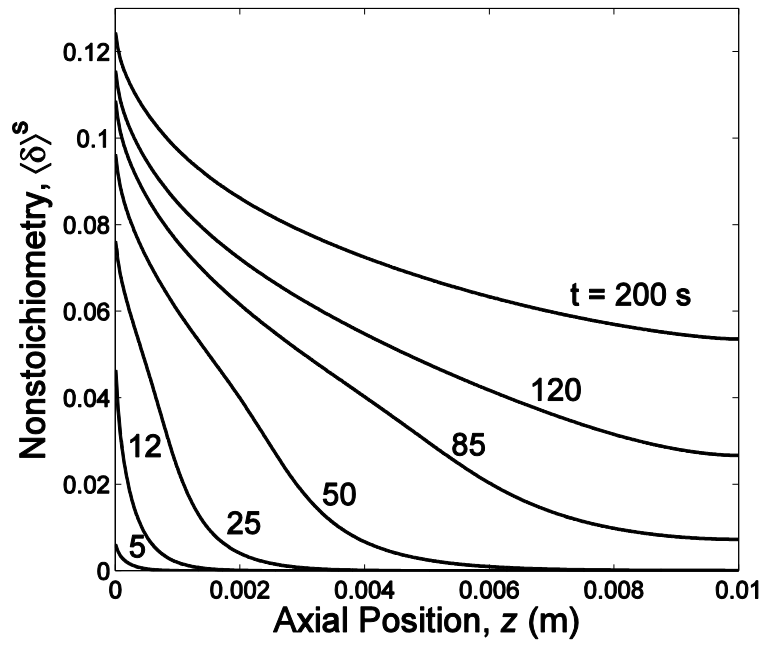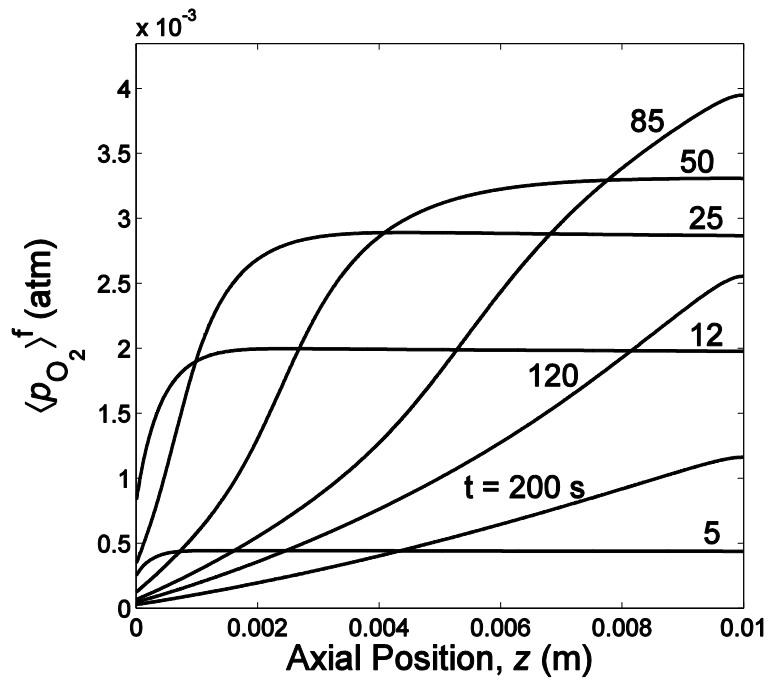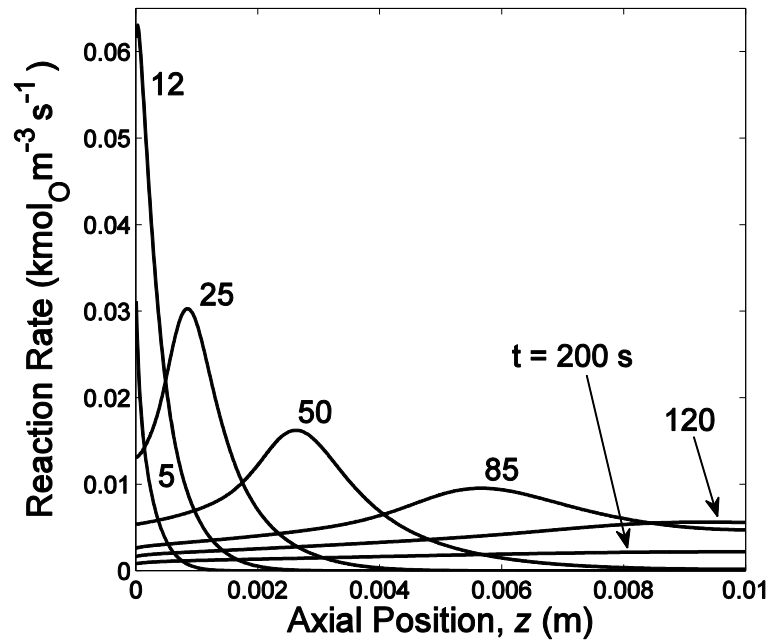
(e)

Fig. 3.4. The axial distributions of (a) solid temperature, (b) fluid temperature, (c) nonstoichiometry, (d) oxygen partial pressure, and (e) reaction rate are plotted at $r = 0$ for selected times.

Chapter 4

The Effects of Morphology on the Thermal Reduction of Nonstoichiometric Ceria under Direct Irradiation[3]

A numerical heat and mass transfer model is used to study the effects of the morphological features of a porous medium composed of ceria when it is placed in a cavity and exposed to high-flux solar irradiation to drive a nonstoichiometric reduction. The morphological features are described by the porosity and pore-level Sauter mean diameter. For porosities of 0.60, 0.75, and 0.90, the rate of oxygen production and the efficiency of solar-to-chemical energy conversion increase monotonically as the Sauter mean diameter is decreased from 1000 to 30 μm. For a porosity of 0.90, these performance metrics continue to increase down to 10 μm. The primary effect of the changes in porosity and Sauter mean diameter are through their influence on the permeability and the extinction coefficient of the medium. For appropriately selected time duration, an energy conversion efficiency of 10.9% is achieved with a Sauter mean diameter of 10 μm and a porosity of 0.90.

Introduction

Ceria has been identified as a promising material for accomplishing solar thermochemical fuel production via the nonstoichiometric redox cycle [17,18,26,40,41]:

Endothermic reduction:
$$CeO_2(s) \rightarrow CeO_{2-\delta}(s) + \frac{\delta}{2}O_2(g) \tag{4.1}$$

Exothermic oxidation:
$$\delta H_2O(g) + CeO_{2-\delta}(s) \rightarrow CeO_2(s) + \delta H_2(g) \tag{4.2a}$$

or

$$\delta CO_2(g) + CeO_{2-\delta}(s) \rightarrow CeO_2(s) + \delta CO(g) \tag{4.2b}$$

---
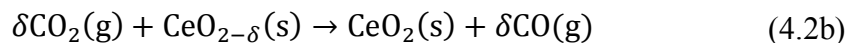
[3] This chapter is based on the manuscript Keene D. J., Lipiński W., and Davidson J. H., "The Effects of Morphology on the Thermal Reduction of Nonstoichiometric Ceria under Direct Irradiation," American Institute of Chemical Engineering, Submitted.

Net reaction:

$$\delta H_2O(g) \rightarrow \delta H_2(g) + \frac{\delta}{2} O_2(g) \qquad (4.3a)$$

or

$$\delta CO_2(g) \rightarrow \delta CO(g) + \frac{\delta}{2} O_2(g) \qquad (4.3b)$$
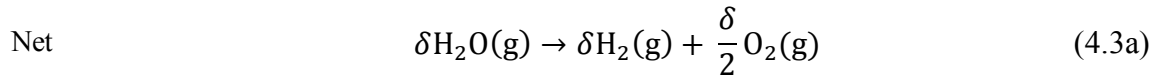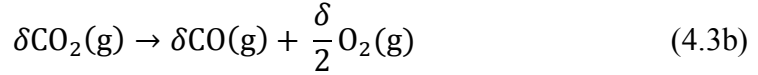
Concentrated solar energy provides the high temperature process heat to drive the endothermic thermal reduction reaction (4.1), followed by the exothermic oxidation reaction (4.2). Reaction (4.1) is realized at low oxygen pressures either under an atmosphere at ambient pressure consisting predominantly of inert gas or/and under reduced pressure. In reaction (4.2), an oxidizer, water and/or carbon dioxide, is introduced to produce hydrogen and/or carbon monoxide. The net result is the splitting of water given by Eq. (4.3a) and/or carbon dioxide given by Eq. (4.3b).

Because nonstoichiometric ceria remains a solid throughout the thermochemical cycle (4.1)−(4.2), a promising approach to accomplish the cycle in a solar reactor is to form the reactive solid into a porous structure to promote rapid solid–gas reactions through a high specific surface area while simultaneously achieving desirable transport characteristics. Prototype reactors using porous ceria structures have been experimentally demonstrated [32–35], and the routes to improved efficiencies based on heat recovery have been outlined in thermodynamic and heat transfer analyses [65,79,80]. However, in addition to the 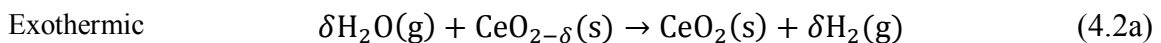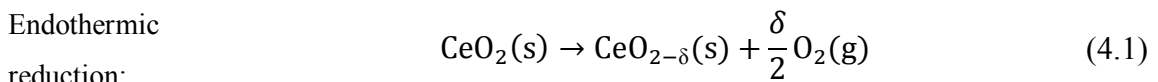incorporation of heat recovery, an understanding of how the morphological features of the porous structure impact its thermochemical behavior is central to developing porous materials for optimal transport processes and redox chemistry and for designing solar reactors that use these materials.

To inform the design of pore architectures, this paper investigates the role of the porosity and pore-level feature size as the two morphological parameters that affect the transport characteristics, and uses numerical modeling to predict their impact on thermochemical performance. In particular, we focus on a thermal reduction step where the porous structure is directly irradiated while an inert sweep gas flows through the pore network to carry away the evolved oxygen product. In the interest of focusing on the

impact of morphology, parameters associated with the domain size and boundary conditions are held constant. The transient combined heat and mass transfer model of the reacting medium formulated by the authors [81] is extended to include nongray internal radiative transport based on the Rosseland diffusion approximation with the morphology-dependent radiative properties of the medium evaluated using Mie theory. The oxygen production per unit mass of ceria, rate of oxygen production, and a solar-to-chemical energy conversion efficiency characterize the performance during the thermal reduction process.

Problem Statement

This study considers a porous monolith with an interconnected pore network to investigate how the thermochemical response of a porous material depends on its morphology. Because the porosity and specific surface area are the most salient morphological characteristics that influence the effective transport properties, these two parameters are used to establish the connection between a specific physical porous structure and an idealized representation. The Sauter mean diameter is used to estimate a pore-level length scale associated with the solid features and is computed based on the porosity and specific surface area according to

$$d_{32} = \frac{1 - \phi}{a_{\mathrm{sf}}/6} \tag{4.4}$$

From a mathematical perspective, Eq. (4.4) shows that a porosity and a specific surface area used to characterize a porous medium can be equivalently quantified in the form of a porosity and Sauter mean diameter, d_{32}. To assess the accuracy of using d_{32} to estimate the pore-level solid feature size, the pore architectures of two porous materials that have been considered for solar thermochemical processes are shown in Fig. 4.1. Using porosity and specific surface area data, the Sauter mean diameters corresponding to the materials shown in Figs. 4.1a and 4.1b are 8.31 μm and 813 μm, respectively. The values obtained using Eq. (4.4) are in qualitative agreement with the actual feature sizes for the

two very different morphologies. We use d_{32} as the representative characteristic size of the porous structure when evaluating morphology-dependent parameters, as described and discussed later in the section on the effective transport properties.

Reactive media that have been considered for solar thermochemical processes have reported porosities ranging from 0.55 to 0.92 and specific surface areas ranging from 9.85×10^2 m^2m^{-3} to 6.75×10^5 m^2m^{-3} [18,39,40,82–86]. After considering the physically realized combinations of porosity and specific surface area, the corresponding Sauter mean diameters of these porous structures range from 3 μm to 813 μm. In this work, the porosity is varied between 0.6 and 0.9 while the Sauter mean diameter is varied between 10 μm and 1000 μm. The corresponding specific surface areas range from 6.0×10^2 m^2m^{-3} to 2.4×10^5 m^2m^{-3}. These ranges represent a wide morphological parameter space whose span includes several candidate porous materials that have been fabricated and are being considered for use in solar thermochemical reactors [32–34].

The porous material is analyzed assuming it is placed at the back of a cavity as shown in Fig. 4.2. The cavity's lateral surface is angled so that the concentrated solar irradiation contained within a half cone angle of 40° entering through the aperture falls on the reactive porous medium. The ratio of aperture to cavity diameter is set at 5 to obtain a high absorption efficiency by capturing reflected and reemitted radiation within the cavity while simultaneously spreading the solar input entering through the aperture over a larger cross-sectional area. By using a cavity while distributing the external irradiation over a larger area, the nominal concentration ratio of the solar input decreases from C_{apert} = 3000 suns (1 sun = 1 kWm^{-2}) at the aperture to C_0 = 120 suns at the face of the porous structure (i.e., the $z = 0$ boundary) without compromising the ability to heat the reactive medium to high temperatures. The radiative exchange in the cavity is modeled by treating the back wall, lateral wall, and aperture as three diffuse and gray surfaces that form an enclosure. In the enclosure analysis, the back wall is treated as black, the lateral wall is treated as adiabatic, and the aperture is treated as cold and black.

The reacting porous structure of ceria is saturated with a gas flow while undergoing the reduction reaction (4.1). The solid phase is assumed to be radiatively participating while the gas phase is assumed to be radiatively non-participating. Furthermore, the solid

phase is treated as an anisotropic and dimensionally stable continuum at the macroscale. At the boundary $z = 0$, an inert sweeping gas enters the medium to carry away the released oxygen. The sweep gas is composed of argon with a small amount (10 ppm) of oxygen and its temperature is set to be 1000 K, which represents moderate gas preheating. The sweep gas flow rate, which is held constant for all cases, is selected so that the temperature of the solid phase at $z = 0$ stabilizes in the range of 1850−1950 K. The boundary at $z = L$ is treated as an outlet at atmospheric pressure and with zero temperature gradient. The system parameters are listed in Table 4.1 and the mathematical formulation of the boundary conditions is presented in the Analysis section.

Analysis

Mass Conservation

Mass conservation equations are formulated for the solid and fluid phases, and the individual components of the fluid phase [81]. The solid phase mass conservation equation is

$$\frac{\partial}{\partial t}\left\{\rho_{CeO_2}(1-\phi)\frac{M_{O_2}}{2M_{CeO_2}}\langle\delta\rangle^s\right\} = \dot{m}''_{sf,O_2}a_{sf} \tag{4.5}$$

Because the fluid is a binary mixture of argon with trace amounts of oxygen, its composition is obtained by solving the species mass conservation equation for oxygen given by [81]

$$\frac{\partial}{\partial t}\left(\phi\langle\rho\rangle^f\langle Y_{O_2}\rangle^f\right) + \nabla\cdot\left(\langle\rho\rangle^f\langle\vec{u}\rangle\langle Y_{O_2}\rangle^f\right)$$
$$= \nabla\cdot\left(D_{O_2,eff}\langle\rho\rangle^f\nabla\langle Y_{O_2}\rangle^f\right) + \dot{m}''_{sf,O_2}a_{sf} \tag{4.6}$$

followed by the computation of the argon mass fraction using

$$\langle Y_{\text{Ar}} \rangle^{\text{f}} = 1 - \langle Y_{\text{O}_2} \rangle^{\text{f}} \tag{4.7}$$

To address the pressure−velocity−density coupling, the ideal gas equation of state for a multi-component mixture

$$\langle p \rangle^{\text{f}} = \left(\sum_i \frac{\langle Y_i \rangle^{\text{f}}}{M_i} \right) \langle \rho \rangle^{\text{f}} \bar{R} \langle T_{\text{f}} \rangle^{\text{f}} \tag{4.8}$$

and Darcy's law

$$-\nabla \left(\phi \langle p \rangle^{\text{f}} \right) = \frac{\mu_{\text{f}} \phi \langle \vec{u} \rangle}{K} \tag{4.9}$$

are substituted into the overall fluid phase mass conservation equation to reformulate it in terms of the pressure according to

$$\frac{\partial}{\partial t} \left\{ \frac{\phi}{\left(\sum_i \frac{\langle Y_i \rangle^{\text{f}}}{M_i} \right) \bar{R} \langle T_{\text{f}} \rangle^{\text{f}}} \langle p \rangle^{\text{f}} \right\}$$

$$= \nabla \cdot \left\{ \frac{\frac{K}{\mu_{\text{f}} \phi}}{\left(\sum_i \frac{\langle Y_i \rangle^{\text{f}}}{M_i} \right) \bar{R} \langle T_{\text{f}} \rangle^{\text{f}}} \langle p \rangle^{\text{f}} \nabla \left(\phi \langle p \rangle^{\text{f}} \right) \right\} + \dot{m}''_{\text{sf,O}_2} a_{\text{sf}} \tag{4.10}$$

Energy Conservation

In the local thermal non-equilibrium formulation, separate energy equations are formulated for each phase. The solid phase energy equation is

$$\frac{\partial}{\partial t}\{(1-\phi)\langle\rho_s\rangle^s\langle h_s\rangle^s\} = \nabla\cdot\left(k_{s,eff}\,\nabla\langle T_s\rangle^s\right) - \langle\nabla\cdot\vec{q}''_{rad}\rangle$$

$$-\dot{m}''_{sf,O_2}a_{sf}h_{O_2,sf} - h_{sf}a_{sf}\left(\langle T_s\rangle^s - \langle T_f\rangle^f\right)$$

(4.11)

where the enthalpy is evaluated using Eq. (4.26) and the interphase enthalpy flux is evaluated using Eq. (4.25). The internal radiative heat transport is modeled using the Rosseland diffusion approximation [73,87]

$$\vec{q}''_{rad} = -\frac{16\sigma(\langle T_s\rangle^s)^3}{3\beta_m^{tr}}\nabla\langle T_s\rangle^s = -k_{rad}\nabla\langle T_s\rangle^s$$

(4.12)

where the Rosseland-mean extinction coefficient is obtained as

$$\frac{1}{\beta_m^{tr}} = \frac{\int_0^\infty \frac{1}{\beta_\lambda^{tr}}\frac{dE_{b\lambda}}{dT}\,d\lambda}{\int_0^\infty \frac{dE_{b\lambda}}{dT}\,d\lambda}$$

(4.13)

Equation (4.12) is valid for the porous ceria structures considered in this study because of their large extinction coefficient and consequently large optical thickness as discussed in the section on effective transport properties.

The fluid phase energy conservation equation is given by

$$\frac{\partial}{\partial t}\left(\phi\langle\rho\rangle^{\mathrm{f}}\sum_i\langle Y_i\rangle^{\mathrm{f}}\langle h_i\rangle^{\mathrm{f}}\right) + \nabla\cdot\left(\langle\rho\rangle^{\mathrm{f}}\langle\vec{u}\rangle\sum_i\langle Y_i\rangle^{\mathrm{f}}\langle h_i\rangle^{\mathrm{f}}\right)$$

$$= \nabla\cdot\left(\langle\rho\rangle^{\mathrm{f}}\sum_i\langle h_i\rangle^{\mathrm{f}}D_{i,\mathrm{eff}}\nabla\langle Y_i\rangle^{\mathrm{f}}\right) + \nabla\cdot\left(k_{\mathrm{f,eff}}\nabla\langle T_{\mathrm{f}}\rangle^{\mathrm{f}}\right) \qquad (4.14)$$

$$+\dot{m}''_{\mathrm{sf,O_2}}a_{\mathrm{sf}}h_{\mathrm{O_2,sf}} + h_{\mathrm{sf}}a_{\mathrm{sf}}\left(\langle T_{\mathrm{s}}\rangle^{\mathrm{s}} - \langle T_{\mathrm{f}}\rangle^{\mathrm{f}}\right)$$

Boundary and Initial Conditions

The boundary conditions for the conservation of mass, species mass, and fluid energy equations at the inlet are based on treating the region located immediately upstream of the solution domain as quasi-steady. Hence, the boundary condition for the mass conservation mass equation, Eq. (4.10), at $z = 0$ sets the total mass flux entering the domain according to

$$\left(\langle\rho\rangle^{\mathrm{f}}\langle u_{\mathrm{f},z}\rangle\right)\big|_{z=0} = \left(-\frac{\frac{K}{\mu_{\mathrm{f}}\phi}}{\left(\sum_i\frac{\langle Y_i\rangle^{\mathrm{f}}}{M_i}\right)\bar{R}\langle T_{\mathrm{f}}\rangle^{\mathrm{f}}}\langle p\rangle^{\mathrm{f}}\frac{\partial\left(\phi\langle p\rangle^{\mathrm{f}}\right)}{\partial z}\right)\Bigg|_{z=0} = (\rho_{\mathrm{f}}u_z)_\infty \quad (4.15)$$

The flow into the domain is modeled as uniform across the $z = 0$ boundary based on the pressure drop across the medium being sufficiently high and/or the sweep gas flow delivery system in the cavity being appropriately designed to provide a uniform profile. The boundary condition for the conservation of species mass equation, Eq. (4.6), at $z = 0$ sets the total flux of species i (sum of advection and diffusion) into the domain equal to the "far upstream" advective flux according to

$$\left(\langle\rho\rangle^{\mathrm{f}}\langle u_{\mathrm{f},z}\rangle\langle Y_i\rangle^{\mathrm{f}} - \langle\rho\rangle^{\mathrm{f}}D_{i,\mathrm{eff}}\frac{\partial\langle Y_i\rangle^{\mathrm{f}}}{\partial z}\right)\Bigg|_{z=0} = (\rho_{\mathrm{f}}u_z Y_i)_\infty \qquad (4.16)$$

48

Similarly, the boundary condition for the conservation of fluid energy equation, Eq. (4.14), at $z = 0$ sets the total flux equal to the far-field advective flux according to

$$\left(\langle\rho\rangle^{\mathrm{f}}\langle u_{\mathrm{f},z}\rangle \sum_i \langle Y_i\rangle^{\mathrm{f}}\langle h_i\rangle^{\mathrm{f}} - k_{\mathrm{f,eff}}\frac{\partial\langle T_{\mathrm{f}}\rangle^{\mathrm{f}}}{\partial z} - \langle\rho\rangle^{\mathrm{f}} \sum_i \langle h_i\rangle^{\mathrm{f}} D_{i,\mathrm{eff}}\frac{\partial\langle Y_i\rangle^{\mathrm{f}}}{\partial z} \right)\Bigg|_{z=0}$$
$$= \left(\rho_{\mathrm{f}} u_z \sum_i Y_i h_i \right)_{\infty} \tag{4.17}$$

The boundary condition for the solid phase energy equation, Eq. (4.11), at $z = 0$ is derived by considering an idealized model of the cavity receiver. Applying the net radiation method to analyze reflection and emission within the enclosure composed of the boundary of the porous medium, lateral wall, and aperture, the net heat flux into the solid phase of the porous medium at $z = 0$ can be expressed as

$$q'' = \alpha_{0,\mathrm{eff}} C_0 I - \varepsilon_{0,\mathrm{eff}}\sigma(\langle T_{\mathrm{s}}\rangle^{\mathrm{s}}|_{z=0})^4 \tag{4.18}$$

where the effective absorptivity and emissivity of the back wall are derived from the enclosure analysis to be

$$\alpha_{0,\mathrm{eff}} = \frac{\varepsilon_0}{1 - \frac{F_{0-1}F_{1-0}}{1 - F_{1-1}}(1 - \varepsilon_0)} \tag{4.19}$$

$$\varepsilon_{0,\mathrm{eff}} = \frac{\varepsilon_0}{1 - \frac{F_{0-1}F_{1-0}}{1 - F_{1-1}}(1 - \varepsilon_0)}\left(1 - \frac{F_{0-1}F_{1-0}}{1 - F_{1-1}}\right) \tag{4.20}$$

where F_{0-1} is the view factor describing the fraction of the back wall (surface 0) radiosity intercepted by the remaining cavity surface (surface 1). The effective absorptivity $\alpha_{0,\mathrm{eff}}$

relates the heat flux absorbed by the back wall of the cavity to the external (total hemispherical) irradiation that arrives there directly from the aperture. The effective emissivity $\varepsilon_{0,\text{eff}}$ relates the total heat flux leaving the back wall of the cavity relative to the emissive power of a blackbody at $T = \langle T_s \rangle^s|_{z=0}$. Note that the effective absorptivity and emissivity as defined by Eqs. (4.19) and (4.20) are not the apparent absorptivity and emissivity of a cavity as commonly defined in the literature; the former are defined with respect to a selected cavity wall element while the latter are defined with respect to the cavity aperture. Equating the heat flux in Eq. (4.18) with the net heat flux transported into the medium by conductive and internal radiative heat transfer gives the full boundary condition for the solid phase energy equation, Eq. (4.11), at $z = 0$ as

$$\left(\varepsilon_{0,\text{eff}} \sigma (\langle T_s \rangle^s)^4 - \left(k_{s,\text{eff}} + k_{\text{rad}} \right) \frac{\partial \langle T_s \rangle^s}{\partial z} \right) \Bigg|_{z=0} = \alpha_{0,\text{eff}} C_0 I \qquad (4.21)$$

At the $z = L$ boundary, the pressure is set to be atmospheric while the customary outflow boundary condition of setting the mass fraction and fluid temperature gradient to zero is used for the conservation of species mass and fluid energy equations, respectively. For the solid phase energy equation boundary condition at $z = L$, the solid temperature gradient is set to zero.

The initial conditions for Eqs. (4.5), (4.6), (4.10), (4.11), and (4.14) are listed in Table 4.2 in a compact form by defining $p_0^2 = p_L^2 + \frac{2\mu_f L}{K} (\rho u_z)_\infty \left(\sum_i \frac{Y_{i,\infty}}{M_i} \right) \bar{R} T_{f,\infty}$. These conditions correspond to the steady state analytical solution to the set of governing equations at the initial temperature when the solid temperature gradient is set to zero at $z = 0$. All field variables are obtained analytically except for the nonstoichiometry, which is computed numerically based on the local temperature and oxygen partial pressure in accordance with chemical equilibrium.

Solution Method

The finite volume method [77,78] is used to discretize the governing equations in space. The solutions are obtained using an in-house developed Fortran code that employs a staggered grid with the linear (central difference) interpolation scheme. A nonuniform grid has been used to ensure the gradients near the inlet are well-resolved by designing the grid to have a uniformly spaced fine grid region near the inlet and a uniformly spaced coarse grid region near the outlet. The fine grid region comprises 100 cells each of length Δz_{fine} for a total fine grid region length L_{fine}, after which the cell length is progressively increased following a geometric sequence described by

$$\Delta z_{iz} = \Delta z_{iz-1}\,\gamma \tag{4.22}$$

to smoothly transition to the cell sizes of the coarse grid region. The geometric stretching parameter never exceeds its nominal value of $\gamma = 1.5$, and details about the grid used for the different cases are presented in Table 4.3. Time integration is performed using the implicit Euler method to accommodate the disparate time scales and control the action of the nonlinear source terms. The latter allows for enforcing the positivity criterion on pressure, mass fractions, and temperatures as outlined in [81]. A time step size of 10^{-2} s is used.

The coupled nature of the governing equations is addressed by sequentially solving Eqs. (4.5), (4.6), (4.11), (4.14), and (4.10) to update $\langle\delta\rangle^{\text{s}}$, $\langle Y_{O_2}\rangle^{\text{f}}$, $\langle T_{\text{s}}\rangle^{\text{s}}$, $\langle T_{\text{f}}\rangle^{\text{f}}$, and $\langle p\rangle^{\text{f}}$, respectively. Then, Eqs. (4.8) and (4.9) are used to update $\langle\rho\rangle^{\text{f}}$ and $\langle\vec{u}\rangle$, respectively to complete an outer iteration. Outer iterations are repeated until the L^2 norm of the relative changes in $\langle\delta\rangle^{\text{s}}$, $\langle Y_{O_2}\rangle^{\text{f}}$, $\langle T_{\text{s}}\rangle^{\text{s}}$, $\langle T_{\text{f}}\rangle^{\text{f}}$, and $\langle p\rangle^{\text{f}}$ between two successive outer iterations are all less than 10^{-6}.

Reduction Kinetics and Thermodynamics

The reduction reaction (4.1) gives rise to interphase mass and enthalpy fluxes associated with the release of oxygen from the solid phase into the gas phase. Because

the chemical equilibrium of the reduction reaction is very sensitive to temperature and oxygen partial pressure, both the uptake and release of oxygen are considered. These processes are described at the lattice level using Kröger−Vink notation as

$$Ce'_{Ce} + V_O^{\cdot\cdot} + \frac{1}{2}O_2(g) \leftrightarrow Ce_{Ce}^X + O_O^X \tag{4.23}$$
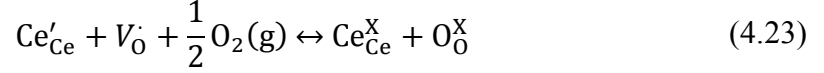
Equation (4.23) assumes the oxygen vacancy ($V_O^{\cdot\cdot}$) is singly ionized so that there is a single cerium atom in its 3+ oxidation state (Ce'_{Ce}) per released oxygen atom. As discussed in [81], applying the law of mass action and invoking crystal site conservation and electroneutrality ultimately yields the following expression for the interphase mass flux of oxygen:

$$\dot{m}''_{sf,O_2} = \frac{M_{O_2}}{2}\dot{n}''_{sf,0}\left\{\exp\left(\frac{1}{2}\frac{\Delta\bar{h}^0_{O_2} - \langle T_s\rangle^s\Delta\bar{s}^0_{O_2}}{\bar{R}\langle T_s\rangle^s}\right)(\langle\delta\rangle^s)^2 \right.$$
$$\left. -\left(\frac{\langle p_{O_2}\rangle^f}{p_{ref}}\right)^{\frac{1}{2}}(\langle\delta\rangle^s)^2\right\} \tag{4.24}$$

The thermodynamic functions appearing in Eq. (4.24) have been measured for ceria in the range $0.001 \leq \delta \leq 0.27$ and found to depend solely on nonstoichiometry throughout the entire temperature range for which data were collected (1023 K $\leq T \leq$ 1773 K) [72]. Thus, relying on these measurements to evaluate $\Delta\bar{h}^0_{O_2}$ and $\Delta\bar{s}^0_{O_2}$ at temperatures above 1773 K (for which no data exist) is a reasonable extrapolation provided the nonstoichiometry is less than 0.27. No experimental data are currently available for estimating the kinetic parameter $\dot{n}''_{sf,0}$. Results from bench-scale testing [18,42] and prototype reactors [18,34] suggest that the thermal reduction reaction is limited by the heating rate of the solid. Consequently, the value of $\dot{n}''_{sf,0}$ is selected in the present study to be sufficiently large so that the reaction rate given by Eq. (4.24) becomes an

implementation of equilibrium chemistry (i.e., fast kinetics causes the chemical reaction to become transport limited).

To ensure that the kinetic rate constant is sufficiently fast so as to allow the chemistry to maintain equilibrium, the computed nonstoichiometry field obtained from solving Eq. (4.5) was compared to the equilibrium nonstoichiometries corresponding to the oxygen partial pressure and solid temperature fields obtained by solving Eqs. (4.6), (4.10), and (4.11). The case of $\phi = 0.90$ and $d_{32} = 10$ μm was selected for this comparison because it experiences the most rapid temperature rise and is therefore the least likely to be transport limited. When comparing the computed and equilibrium nonstoichiometries, the maximum difference at any location in the domain is always less than 6.1×10^{-3}. When comparing the average nonstoichiometry and average equilibrium nonstoichiometry, the maximum difference is always less than 4.5×10^{-4}. Considering that local and average nonstoichiometries as large as 1.21×10^{-1} and 8.3×10^{-2}, respectively, occur, these differences are sufficiently small to verify the quasi-equilibrium nature of the heterogeneous chemical reaction. Furthermore, because the reaction rate expression is formulated as the product of an interphase mass flux and the specific surface area, both the kinetic rate constant $\dot{n}''_{sf,0}$ and the specific surface area have the same multiplicative influence on the reaction rate term in the conservation equations. To eliminate any possibility of introducing a kinetic influence when the specific surface area changes as a consequence of changing the Sauter mean diameter, the value of the kinetic rate constant is adjusted as different d_{32} values are considered. Specifically, the kinetic rate constant is set to $\dot{n}''_{sf,0}/d_{32} = 10^{-2} \, \text{kmol}_O \text{m}^{-2} \text{s}^{-1} \mu\text{m}^{-1}$.

The enthalpy of the oxygen leaving the solid to enter the gas is evaluated at the solid temperature whereas the fluid temperature is used to evaluate the enthalpy of the oxygen leaving the gas to enter the solid. Hence, the net interphase enthalpy flux is given by

$$\dot{m}''_{\text{sf},O_2} h_{O_2,\text{sf}} = \frac{M_{O_2}}{2} \dot{n}''_{\text{sf},0} \left\{ \exp\left(\frac{1}{2} \frac{\Delta \bar{h}^0_{O_2} - \langle T_s \rangle^s \Delta \bar{s}^0_{O_2}}{\bar{R} \langle T_s \rangle^s} \right) (\langle \delta \rangle^s)^2 h_{O_2}|_{\langle T_s \rangle^s} \right.$$

$$\left. - \left(\frac{\langle p_{O_2} \rangle^f}{p_{\text{ref}}} \right)^{\frac{1}{2}} (\langle \delta \rangle^s)^2 h_{O_2}|_{\langle T_f \rangle^f} \right\} \tag{4.25}$$

The molar enthalpy of ceria is evaluated as a function of temperature and nonstoichiometry as [81]

$$\bar{h}_{CeO_{2-\delta}}|_{T_s} = \bar{h}_{\text{form},CeO_2}|_{T_{\text{ref}}} + \int_{T_{\text{ref}}}^{T_s} \bar{c}_{p,CeO_2} dT - \frac{1}{2} \int_0^\delta \Delta \bar{h}^0_{O_2} d\delta'$$

$$- \frac{\delta}{2} \bar{h}_{O_2}|_{T_s} \tag{4.26}$$

where the formation enthalpy and temperature-dependent specific heat for cerium dioxide are taken from [70].

Effective Transport Properties

The relationships used to compute the effective transport properties are summarized in Table 4.4. The mass diffusion coefficient for oxygen in argon is calculated using Chapman–Enskog theory [68], while the intrinsic viscosity and thermal conductivity for the fluid mixture are calculated using a weighted average where the mole fraction is the weighting function. The pure species viscosities, thermal conductivities, and specific heats are evaluated as functions of temperature [69,70] as is the thermal conductivity of the solid based on data for bulk ceria [71].

For the purposes of this study, relationships between the morphological parameters and the effective transport properties with broad applicability are used to calculate the effective transport properties. There is some variability in the predicted values of the effective transport properties when using different relationships reported in the literature

[39,74,84,86,88], but the form of the dependence on the porosity and/or pore-level length scale (which governs the trends related to changing the morphological parameters) does not differ significantly. Furthermore, the sensitivity to this variability is investigated using the interphase heat transfer coefficient because its value experiences the greatest variability and also depends strongly on the pore-level length scale. Based on the reported correlation for an anisotropic porous monolith [39], the interphase heat transfer coefficient used in this study was decreased by a factor of 16 for $(\phi, d_{32}) = (0.60, 10 \text{ }\mu\text{m})$ for comparison. Even for such a conservatively large difference, the impact on the global performance metrics is very small; the peak solar-to-chemical energy conversion efficiency changes by less than 1.3%[4]. Based on the reported correlation for an RPC structure [89], the interphase heat transfer coefficient used in this study was decreased by a factor of 2 for $(\phi, d_{32}) = (0.90, 1000 \text{ }\mu\text{m})$. Again, the impact is small; the peak solar-to-chemical energy conversion efficiency changes by less than 0.3%.

The permeability is calculated using the hydraulic radius concept because the Kozeny constant has been found to be a weak function of morphology [74,88]. The tortuosity for mass diffusion is set to unity, which corresponds to the upper bound of the effective diffusivity. The interphase heat transfer coefficient is calculated using the empirical correlation for packed beds [75] with the Sauter mean diameter replacing the particle diameter to obtain

$$\text{Nu}_{\text{pore}} = \frac{h_{\text{sf}} d_{32}}{k_{\text{f}}} = 2 + 1.1 \left(\frac{\langle \rho \rangle^{\text{f}} \langle |\vec{u}| \rangle d_{32}}{\mu_{\text{f}}} \right)^{0.6} \text{Pr}^{1/3} \qquad (4.27)$$

As developed in [81], the effective thermal conductivities are computed by evaluating the closure terms using knowledge of the stagnant thermal conductivity according to

---

[4] The solar-to-chemical energy conversion efficiency differing by less than 1.3% corresponds to a difference in at most the third significant figure (i.e., it is not meant as a change in the efficiency from 10% to 8.7%).

$$k_{\text{f,eff}} = \phi\langle k_{\text{f}}\rangle^{\text{f}} - \frac{\langle k_{\text{f}}\rangle^{\text{f}}}{\langle k_{\text{s}}\rangle^{\text{s}} - \langle k_{\text{f}}\rangle^{\text{f}}}\left(k_{\text{stag}} - (1-\phi)\langle k_{\text{s}}\rangle^{\text{s}} - \phi\langle k_{\text{f}}\rangle^{\text{f}}\right) \qquad (4.28)$$

$$k_{\text{s,eff}} = (1-\phi)\langle k_{\text{s}}\rangle^{\text{s}} + \frac{\langle k_{\text{s}}\rangle^{\text{s}}}{\langle k_{\text{s}}\rangle^{\text{s}} - \langle k_{\text{f}}\rangle^{\text{f}}}\left(k_{\text{stag}} - (1-\phi)\langle k_{\text{s}}\rangle^{\text{s}} - \phi\langle k_{\text{f}}\rangle^{\text{f}}\right) \quad (4.29)$$

The geometric mean model for the stagnant thermal conductivity given by

$$k_{\text{stag}} = (\langle k_{\text{s}}\rangle^{\text{s}})^{1-\phi}\left(\langle k_{\text{f}}\rangle^{\text{f}}\right)^{\phi} \qquad (4.30)$$

is used because it provides good estimates for general isotropic porous media [90].

Broadly applicable predictions of the radiative properties of porous structures are precluded by the inherent complexity of scattering and its dependence on pore-level geometry details, which can differ considerably between various morphologies. However, due to the considerable effort required to completely characterize different morphologies and perform subsequent pore-level numerical simulations and/or experimental measurements, this work takes a simplified approach to establish a relationship between the radiative properties and the porosity and Sauter mean diameter.

The radiative properties are obtained by considering the solid phase to be a monodispersion of spherical particles with the particle diameter determined using Eq. (4.4) based on the porosity and specific surface area of the actual porous medium. The radiative properties of this idealized monodispersion are then determined from Mie theory. Using this approach to evaluate the transport extinction and scattering coefficients has been shown to be acceptable [38,87,91,92]. Independent scattering can be assumed for this monodispersion of spheres if $c/\lambda > 0.5$ [93], which has been tested by estimating the interparticle clearance c as if the spheres are positioned so that their centers form a body-centered cubic lattice. This calculation allows the interparticle clearance criterion to be expressed as

$$\lambda < 2\left[\left(\frac{\pi/6}{1-\phi}\right)^{1/3} - 1\right]d_{32} = \lambda_{cr} \qquad (4.31)$$

which shows explicitly that increasing ϕ and/or d_{32} promotes independent scattering. In light of the temperature-dependent spectral weighting function used when calculating the Rosseland-mean extinction coefficient and the temperatures encountered in this work, the independent scattering assumption is appropriate for all porosity and Sauter mean diameter combinations considered except for $(\phi, d_{32}) = (0.60, 10 \ \mu m)$. For this case, λ_{cr} = 1.88 μm, indicating that dependent scattering effects begin to become important for a non-neglibigle portion of the spectrum. Therefore, some weak dependent scattering effects are anticipated for $(\phi, d_{32}) = (0.60, 10 \ \mu m)$, but not to an extent to remove this case from consideration.

To apply Mie theory, the complex refractive index of ceria is computed for the spectral range of 100 nm $\leq \lambda \leq$ 20 μm from measurements of the complex dielectric function of cerium dioxide [94] as shown in Fig. 4.3 while the refractive index of the gas (host medium) is taken as unity. The spectral transport extinction coefficient is computed as

$$\beta_\lambda^{tr} = \frac{3}{2}\frac{1-\phi}{d_{32}}\left[Q_{abs,\lambda} + Q_{sca,\lambda}(1 - g_\lambda)\right] \qquad (4.32)$$

where $Q_{abs,\lambda}$ and $Q_{sca,\lambda}$ are the absorption and scattering efficiency factors and g_λ is the asymmetry scattering factor, obtained using the BHMIE subroutine [95]. The spectral transport extinction coefficient values obtained from this calculation do not differ greatly from estimates based on experimental measurements [36,37]. Results from a similar application of Mie theory agree reasonably with experimental results for ceria porous structures [38,67], which further supports the use of the approach taken in the present study.

The spectral integrals in Eq. (4.13) are evaluated by decomposing the spectral range into 249 bands over which $\beta_\lambda^{\text{tr}}$ is treated as constant. The spectral resolution is selected based on the anticipated range of solid phase temperatures. The extinction coefficient is calculated at the discrete wavelengths $\lambda_{\text{calc},i}$ defined by

$$\lambda_{\text{calc},i} = \lambda_{\text{calc},i-1} + \Delta\lambda_i, \qquad i = 2,3,4,\dots 249, \qquad \lambda_{\text{calc},1} = 100\text{nm},$$

$$\Delta\lambda_i = \begin{cases} 50 \text{ nm for } i \leq 99 \\ 100 \text{ nm for } i \geq 100 \end{cases} \tag{4.33}$$

while the endpoints defining the bands that contain the discrete wavelengths are given by

$$\lambda_{\text{end},i} = \begin{cases} 0 & \text{for } i = 0 \\ \dfrac{\lambda_{\text{calc},i} + \lambda_{\text{calc},i+1}}{2} & \text{for } 1 \leq i \leq 248 \\ \infty & \text{for } i = 249 \end{cases} \tag{4.34}$$

The primary computational expense associated with the use of the nongray Rosseland approximation stems from the spectral integration because the temperature-dependent weighting function requires $\beta_{\text{m}}^{\text{tr}}$ to be updated as the solution evolves. The spectral variation of the inverse of the extinction coefficient combined with the multiplicative factor accounting for the effect of porosity is plotted in Fig. 4.4 so that the radiative behavior for all combinations of ϕ and d_{32} considered in this study can be shown concisely using a single plot. As expected, the majority of the Sauter mean diameters lead to a weak spectral dependence because of their large size parameters. The extinction coefficient increases as the Sauter mean diameter decreases, closely following the trend of $\beta_\lambda^{\text{tr}} \propto 1/d_{32}$ because the absorption and scattering efficiency factors depend only slightly on the Sauter mean diameter.

Results

The impact of the morphology of the reactive medium on its thermochemical performance is quantified using the domain-average nonstoichiometry δ_{average}, the overall rate of oxygen release per unit cross-sectional area of the medium, and the overall solar-to-chemical energy conversion efficiency. The domain-average nonstoichiometry is obtained by averaging the local nonstoichiometry over the entire domain according to

$$\delta_{\text{average}}(t) = \frac{1}{V} \int_V \delta(z,t) \, dV \tag{4.35}$$

This integral quantity indicates the capacity for fuel production (per unit solid mass) and can be interpreted as a global reaction extent coordinate. However, δ_{average} alone does not fully describe the rate at which oxygen is released, so to make a more complete and balanced comparison of potential fuel production rates between the different cases, the overall rate of oxygen release per unit of cross-sectional area is computed as the product of the amount of oxygen produced per unit mass of ceria (in $\text{kmol}_O \text{kg}^{-1}_{\text{CeO}_2}$) and the overall rate at which ceria is cycled (in $\text{kg}_{\text{CeO}_2} \text{m}^{-2} \text{s}^{-1}$) according to

$$\begin{aligned}
\frac{\dot{n}''_{O_2}(t)}{2} &= \left(\frac{n_{O_2}/2}{m_{\text{CeO}_2}}\right)\left(\frac{m_{\text{CeO}_2}}{t} \frac{1}{\frac{\pi}{4}(D_{\text{apert}})^2}\right) \\
&= \left(\frac{\Delta\delta_{\text{average}}}{M_{\text{CeO}_2}}\right)\left(\frac{\rho_{\text{CeO}_2}(1-\phi)L}{t}\right)
\end{aligned} \tag{4.36}$$

where $\Delta\delta_{\text{average}} = \delta_{\text{average}}(t) - \delta_{\text{average}}(0)$. The instantaneous power requirement of the chemical reaction is defined based on breaking the chemical bonds between the cerium and oxygen atoms, which for the entire medium is calculated as

$$\dot{Q}_{\mathrm{chem}}(t) = -\int_V \frac{\partial}{\partial t}\left\{(1-\phi)\bar{\rho}_s\left(-\frac{1}{2}\int_0^\delta \Delta\bar{h}^0_{\mathrm{O}_2}d\delta'\right)\right\}dV \qquad (4.37)$$

Integrating this quantity over time and comparing it to the total amount of solar energy that is received in the same period of time yields

$$\eta_{\mathrm{batch}}(t) = \frac{-Q_{\mathrm{chem}}(t)}{Q_{\mathrm{solar}}(t)} = \frac{-\int_0^t \dot{Q}_{\mathrm{chem}}(t')dt'}{\int_0^t \dot{Q}_{\mathrm{solar}}(t')dt'} \qquad (4.38)$$

Note that while $\delta_{\mathrm{average}}$ is an instantaneous quantity, both $\dot{n}''_{\mathrm{O}_2}$ and η_{batch} involve time integration over the duration of a batch process. Also, η_{batch} characterizes only the thermal reduction process and as such can not be interpreted as the efficiency of a complete thermochemical cycle.

Because $\Delta\bar{h}^0_{\mathrm{O}_2}$ does not vary greatly over the encountered nonstoichiometry range, Q_{chem} is approximately proportional to $\Delta\delta_{\mathrm{average}}$, as shown by Eq. (4.37). Also, for steady solar power Q_{solar} is proportional to t. Consequently, the time evolution of both the overall rate of oxygen release per cross-sectional area ($\mathrm{kmol_O\,m^{-2}s^{-1}}$) and the overall energy conversion efficiency are both proportional to $\Delta\delta_{\mathrm{average}}/t$. For this reason, only peak overall oxygen release rates are reported (see Table 4.5).

The effects of morphology on the thermochemical performance of the reactive systems are explored by varying the Sauter mean diameter from 10 μm to 1000 μm for porosities of 0.60, 0.75, and 0.90. Unlike changing the Sauter mean diameter, changing the porosity leads to changes in the total amount of solid mass in the system (because the total volume of the porous medium is held constant). The change in mass influences significantly how quickly the transients evolve for fixed solar power input. Consequently, the presentation of the results is organized by comparing the effect of changing the Sauter mean diameter while holding the porosity fixed. Decreasing the

Sauter mean diameter while holding the porosity constant decreases the permeability and increases the extinction coefficient, specific surface area, and interphase convective heat transfer coefficient. As will be shown, among these factors, the two characteristics of greatest importance in predicting the trends in the performance metrics are the permeability and extinction coefficient, which have competing influences on performance. Figures 4.5a, 4.5b, and 4.5c show the transient pressure drop variation for selected values of the Sauter mean diameter for porosity values of $\phi = 0.60$, 0.75, and 0.90, respectively. Because the sweep gas flow rate $(\rho u_z)_\infty$ is constant, decreasing d_{32} increases the pressure drop due to the decrease in the permeability, and consequently increases the total pressure. Therefore, even apart from pumping power ramifications, a low permeability is undesirable because it is more difficult to maintain the low oxygen partial pressures that thermodynamically favor oxygen release. Figure 4.5a shows that with $\phi = 0.60$ the pressure drop becomes as high as 0.16 atm, 1.21 atm, and 5.02 atm for $d_{32} = 100$ μm, 30 μm, and 10 μm, respectively, but is otherwise low enough so that the pressure variation throughout the domain is not significant. Figure 4.5b shows that when $\phi = 0.75$, the pressure drop becomes as high as 0.35 atm and 1.89 atm for $d_{32} = 30$ μm and 10 μm, respectively, but is otherwise insignificant. Figure 4.5c shows that when $\phi = 0.90$, the pressure variation is insignificant for all Sauter mean diameters except for $d_{32} = 10$ μm where the pressure drop becomes as high as 0.30 atm. For all cases presented in Fig. 4.5, the pressure drop increases over time to more than twice its initial value as a consequence of the increasing gas temperatures leading to higher viscosities and velocities.

Increasing the extinction coefficient is beneficial to fuel production for the conditions considered. This result is explained by the effect of the extinction coefficient on the radiative conductivity. Increasing the extinction coefficient leads to decreasing k_{rad}, which promotes a more rapid rise of the solid temperature near the irradiated boundary and a greater streamwise temperature gradient. Evidence of the increasing streamwise temperature gradient is observed by comparing the solid temperatures at the $z = 0$ and $z = L$ boundaries. Figure 4.6 shows that as the Sauter mean diameter is decreased, the solid temperature at the irradiated boundary rises more rapidly while the solid

61

temperature at the outlet boundary rises more slowly. These monotonic trends occur for all porosities, as shown in Figs. 4.6−4.8. Although a higher solid temperature at $z = 0$ results in greater reradiation losses, higher temperatures are advantageous for promoting oxygen release because the equilibrium nonstoichiometry value (which is obtained in this study due to the assumption of fast kinetics) increases with temperature (i.e., $\frac{\partial \delta_{eq}}{\partial T} > 0$). Furthermore, the equilibrium nonstoichiometry increases more strongly with temperature as the temperature increases (i.e., $\frac{\partial^2 \delta_{eq}}{\partial T^2} > 0$).

Figure 4.9 shows the time evolution of the average nonstoichiometry and the overall solar-to-chemical energy conversion efficiency for different Sauter mean diameters when the porosity is 0.90. The average nonstoichiometry increases monotonically as the Sauter mean diameter decreases because the temperature dependence of δ_{eq}, in particular the fact that $\frac{\partial^2 \delta_{eq}}{\partial T^2} > 0$, causes a non-uniform heating of the medium and its associated high temperature region to result in more oxygen release. This monotonic increase in the oxygen release also causes a monotonic increase in the solar-to-chemical energy conversion efficiency, η_{batch}. The highest and lowest peak overall efficiency values of 10.9% and 6.97% are obtained with $d_{32} = 10$ μm and 1000 μm, respectively. The details about the maximum values for each case are summarized in Table 4.5.

Figure 4.10 reveals that when the porosity is decreased to $\phi = 0.75$, $\delta_{average}$ and η_{batch} again increase as the Sauter mean diameter is decreased from $d_{32} = 1000$ μm to 30 μm. This trend does not continue for $d_{32} = 10$ μm. Note that for batch duration times shorter than 120 s, a Sauter mean diameter of 10 μm produces a slightly higher efficiency compared to a Sauter mean diameter of 30 μm whereas the opposite is true for batch duration times longer than 120 s. This switch demonstrates the competition between promoting the release of oxygen through higher solid temperatures and hindering the thermodynamic driving force through increased pressure. The high pressure penalty dominates at later times because the pressure drop increases over time as shown in Fig. 4.5. Because both the 10 μm and 30 μm cases experience their peak values after 120 s, the highest peak overall efficiency for a porosity of 0.75 is obtained when the Sauter

mean diameter is 30 μm. The highest and lowest peak overall efficiencies of 10.4% and 7.21% are obtained with $d_{32} = 30$ μm and 1000 μm, respectively.

Figure 4.11 shows the influence of the Sauter mean diameter when the porosity is further decreased to $\phi = 0.60$. The monotonic increase in $\delta_{average}$ and η_{batch} as d_{32} is decreased from 1000 μm to 30 μm remains, but the high pressure penalty dominates even at early times. Consequently, the overall efficiency for $d_{32} = 30$ μm is greater than the overall efficiency when $d_{32} = 10$ μm regardless of the time duration of the process. The highest and lowest peak overall efficiencies of 9.72% and 7.42% are obtained with $d_{32} = 30$ μm and 1000 μm, respectively.

Attributing the deviation from the monotonic increase in $\delta_{average}$ and η_{batch} as d_{32} decreases from 1000 μm to 30 μm to the penalty incurred from a large pressure drop is consistent with the pressure drop magnitudes shown in Fig. 4.5. This explanation is further corroborated by considering special cases with $d_{32} = 10$ and 30 μm where the pressure drop penalty is eliminated by allowing the permeability to remain large. For these special cases (not shown), the monotonic increase in $\delta_{average}$ and η_{batch} as d_{32} is decreased is observed for all porosities considered.

Discussion

When interpreting the findings of this study, it is important to note that the increase in η_{batch} (or equivalently, $\dot{n}''_{O_2}$) as d_{32} is decreased is caused by the nonlinear dependence of δ_{eq} on temperature. Decreasing the ability of the solid to transfer heat into the domain (as is the case for decreasing k_{rad} and/or $k_{s,eff}$) as the means to maximize total oxygen release from a fixed amount of mass using a fixed solar power input is effective for the conditions studied here but does not utilize the entire mass of ceria to its full potential because only a fraction of the domain achieves a significant level of nonstoichiometry. Based on the thermodynamics for the nonstoichiometric ceria cycle and practical consideration, the reduction process is favored at temperatures around 1773 K. Higher temperatures pose material limitations, including sintering of some porous materials and possible volatilization, and higher losses due to reradiation.

The cavity receiver featured in this study helps avoid the problems associated with too high a surface temperature by spreading the concentrated flux over a larger area to achieve a high absorption efficiency while simultaneously decreasing the net flux into the reactive medium. Additionally, high reradiation losses are avoided as a consequence of passing a sweep gas through the pore network. Because the sweep gas is introduced at $T_{f,\infty}$ = 1000 K, the gas is heated by interphase convective heat transfer as it comes into contact with the solid. This convective cooling of the solid helps avoid excessively high temperatures at $z = 0$. Furthermore, after being heated in the inlet region, the sweep gas heats the cooler downstream regions of the solid. Therefore, in addition to working to maintain low oxygen partial pressures by removing the evolved oxygen product, the sweep gas also functions as a thermal energy carrier.

This dual role of the sweep gas suggests multiple alternative strategies that might also enhance the thermochemical performance during reduction. As the solid phase becomes better able to transfer heat by conductive and/or internal radiative heat transfer, the convective cooling of the solid provided by the sweep gas can be decreased without leading to prohibitively high solid temperatures. Decreasing the convective cooling provided by the sweep gas can be accomplished by decreasing the flow rate and/or increasing the temperature at which sweep gas is introduced. Both of these options have associated benefits; the former will decrease the pressure drop across the porous medium as well as the gas separation energy requirement associated with creating the low oxygen content sweep gas mixture while the latter will increase overall reactor efficiency assuming that the sweep gas is preheated using an effective gas phase heat recovery system. While decreasing the sweep gas flow rate might prove beneficial from a total system energy balance perspective for porous materials with good heat transfer characteristics, the flow rate of sweep gas must be sufficient to remove the evolved oxygen product and to thus maintain the partial pressure of oxygen at the desired level. Consequently, the trade-off between the sweep gas' primary role of oxygen removal and its secondary role as a thermal energy carrier is anticipated to yield an optimal sweep gas flow rate.

The significant temperature gradients encountered in this study cause much of the solid to remain at a lower temperature and be consequently underutilized from the perspective of thermochemical cycling. Based on the results of this study, addressing this drawback by modifying the morphology to promote a more uniform high temperature through better internal heat transfer is deleterious to oxygen release. However, the length of the porous medium is a degree of freedom that has not been explored in this study and is expected to impact the uniformity of the temperature and nonstoichiometry fields because of its influence on the optical thickness of the medium. For a particular morphology, the existence of an optimal length for the porous medium is anticipated because a large optical thickness can underutilize the solid from the perspective of redox cycling whereas a small optical thickness can result in the solar power being transmitted through rather than absorbed within the reactive medium.

Conclusion

A transient one-dimensional model that captures the coupled transport and chemical phenomena of a solar-driven thermal reduction process has been applied to study the effects of the porosity and solid feature size of a reactive porous structure composed of ceria for a fixed set of operating conditions. The model features an idealized cavity receiver that distributes a highly concentrated solar flux entering through the aperture over the larger front area of the reactive medium, which in addition to the use of a sweep gas passing through the pore network, allows the solar irradiation to be more readily transported into the porous material.

For the operational conditions and range of morphological parameters considered in this study, the morphology-dependent parameters of greatest influence on the overall solar-to-chemical energy conversion efficiency and/or overall oxygen release rate are the extinction coefficient and the permeability. For each value of porosity, there is an associated Sauter mean diameter that will optimize oxygen release by appropriately balancing the benefits derived from a high extinction coefficient with the penalty of a low permeability. Specifically, the pressure drop becomes significant for $d_{32} = 10$ μm when $\phi = 0.75$ or 0.60, so the best performance for these porosities is predicted when $d_{32} = 30$

µm. When ϕ = 0.90, the pressure drop remains relatively low for all Sauter mean diameters and so the best performance is predicted when d_{32} = 10 µm (the smallest value considered). The ability to obtain good performance during thermal reduction using morphologies with small Sauter mean diameters is a significant advantage because these morphologies also possess the high specific surface areas that will be needed to promote rapid fuel production during the oxidation step of the thermochemical cycle.

While these optimal values of the Sauter mean diameter correspond to the specific set of operational conditions considered, the competing influences of the extinction coefficient and permeability are anticipated to result in an optimal Sauter mean diameter when a different set of fixed operating conditions is considered. The results of this study and projections based on the dependence of the permeability and extinction coefficient on the porosity and Sauter mean diameter indicate that for a fixed set of operating conditions, the optimal Sauter mean diameter will increase as the porosity is decreased for an optically thick reactive medium whose reradiation losses are suppressed by placing it in a cavity receiver and passing sweep gas through its pore network.

This study provides insight into how ϕ and d_{32} impact performance and explores their influence for a specific configuration and set of operational conditions. However, the dual role of the sweep gas and its dependence on operational conditions (e.g., sweep gas flow rate, inlet temperature) clearly speak to the importance of considering the operational conditions when attempting to identify an optimal set of morphological parameters. Ultimately, the conditions related to the sweep gas, length of the porous medium, solar power input, etc. must be selected in concert with the morphology of the reactive medium to maximize performance.

Table 4.1. Simulation input parameters.

Parameter	Symbol	Value
length of porous medium	L	0.02 m
nominal/coarse cell size	Δz_{coarse}	1.0×10^{-4} m
Kozeny constant	k_K	5.0
cerium dioxide density	ρ_{CeO_2}	7215 kg m^{-3}
upstream total mass flux	$(\rho u_z)_\infty$	0.2 kg m^{-2} s^{-1}
upstream oxygen mass fraction	$Y_{O_2,\infty}$	8.0099×10^{-6}
upstream fluid temperature	$T_{f,\infty}$	1000 K
outlet pressure	p_L	1.01325×10^{5} Pa
solar concentration ratio (at $z = 0$)	C_0	120
solar concentration ratio (at aperture)	C_{apert}	3000
nominal unconcentrated solar flux	I	1000 W m^{-2}
emissivity of porous medium at $z = 0$	ε_0	1.0
effective absorptivity at $z = 0$	$\alpha_{0,eff}$	1.0
effective emissivity at $z = 0$	$\varepsilon_{0,eff}$	2.8135×10^{-2}
initial temperature	T_i	1000 K

Table 4.2. Initial conditions.

Variable	Initial Value
pressure	$\dfrac{\langle p \rangle^{\mathrm{f}}}{p_0} = \left\{ 1 - \left(1 - \left(\dfrac{p_L}{p_0} \right)^2 \right) \dfrac{z}{L} \right\}^{1/2}$
oxygen mass fraction	$\langle Y_{O_2} \rangle^{\mathrm{f}} = Y_{O_2,\infty}$
solid temperature	$\langle T_{\mathrm{s}} \rangle^{\mathrm{s}} = T_{\mathrm{i}}$
fluid temperature	$\langle T_{\mathrm{f}} \rangle^{\mathrm{f}} = T_{\mathrm{i}}$
nonstoichiometry	$\langle \delta \rangle^{\mathrm{s}} = \delta_{\mathrm{eq}}(\langle T_{\mathrm{s}} \rangle^{\mathrm{s}}, \langle p_{O_2} \rangle^{\mathrm{f}})$
radial velocity	$\langle u_r \rangle = 0$
axial velocity	$\langle u_z \rangle = \dfrac{\dfrac{1}{2} \dfrac{K p_0}{\mu_{\mathrm{f}} L} \left(1 - \left(\dfrac{p_L}{p_0} \right)^2 \right)}{\left\{ 1 - \left(1 - \left(\dfrac{p_L}{p_0} \right)^2 \right) \dfrac{z}{L} \right\}^{1/2}}$

Table 4.3. Numerical grid parameters.

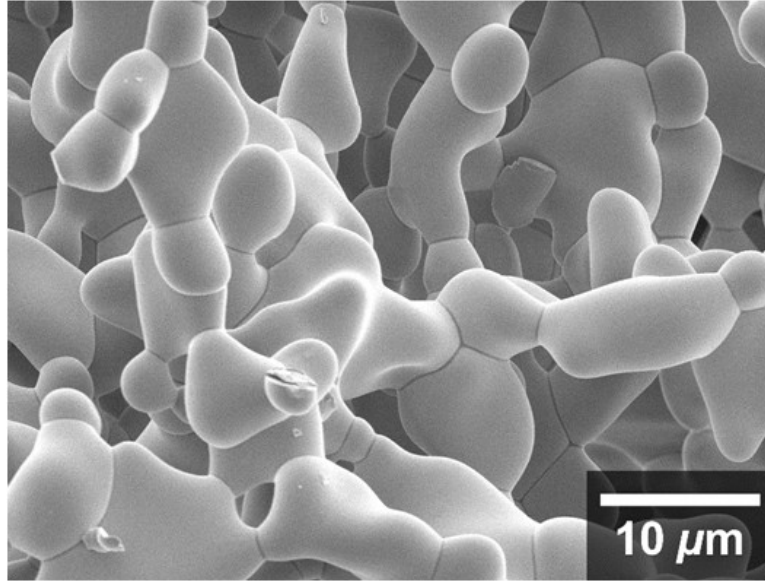| d_{32} (μm)	Δz_{fine} (m)	L_{fine} (m)	Δz_{coarse} (m)	$N_{\Delta z}$
10	2.0×10^{-7}	2.0×10^{-5}	1.0×10^{-4}	313
30	5.0×10^{-7}	5.0×10^{-5}	1.0×10^{-4}	310
100	2.0×10^{-6}	2.0×10^{-4}	1.0×10^{-4}	305
300	6.0×10^{-6}	6.0×10^{-4}	1.0×10^{-4}	299
1000	2.0×10^{-5}	2.0×10^{-3}	1.0×10^{-4}	282

Table 4.4. Morphology-dependent macroscopic transport properties.

| Parameter	Dependence
K	$K = \dfrac{\phi^3}{k_K a_{\text{sf}}^2}$
$D_{i,\text{eff}}$	$D_{i,\text{eff}} = \phi D_i$
h_{sf}	see Eq. (4.27)
$k_{\text{f,eff}}$	see Eqs. (4.28) and (4.30)
$k_{\text{s,eff}}$	see Eqs. (4.29) and (4.30)
$\beta_{\text{m}}^{\text{tr}}$	see Eqs. (4.32) and (4.13)

Table 4.5. Overall energy conversion efficiency and oxygen production characteristics.

Case		$t_{\max,\eta}$ (s)	η_{batch} $(t_{\max,\eta})$	$t_{\max,\dot{n}''_{O_2}}$ (s)	$\frac{1}{2}\dot{n}''_{O_2}(t_{\max,\dot{n}''_{O_2}})$ $(\text{kmol}_O\text{m}^{-2}\text{s}^{-1})$	δ_{average} $(t_{\max,\dot{n}''_{O_2}})$
ϕ	d_{32} (μm)					
0.60	10	454.5	0.08917	466.0	2.337×10^{-5}	0.03245
0.60	30	452.0	0.09724	466.5	2.560×10^{-5}	0.03558
0.60	100	472.0	0.09397	490.0	2.472×10^{-5}	0.03609
0.60	300	533.0	0.08363	557.5	2.191×10^{-5}	0.03640
0.60	1000	627.0	0.07416	658.0	1.941×10^{-5}	0.03806
0.75	10	263.0	0.10210	270.0	2.689×10^{-5}	0.03458
0.75	30	266.5	0.10350	275.0	2.732×10^{-5}	0.03578
0.75	100	294.5	0.09258	306.5	2.432×10^{-5}	0.03551
0.75	300	351.0	0.07995	368.0	2.092×10^{-5}	0.03669
0.75	1000	408.0	0.07215	428.0	1.889×10^{-5}	0.03853
0.90	10	101.0	0.10910	104.0	2.882×10^{-5}	0.03559
0.90	30	110.0	0.09864	114.0	2.596×10^{-5}	0.03514
0.90	100	135.0	0.08241	141.0	2.157×10^{-5}	0.03616
0.90	300	159.0	0.07344	167.0	1.922×10^{-5}	0.03817
0.90	1000	172.5	0.06974	181.0	1.826×10^{-5}	0.03933

(a)
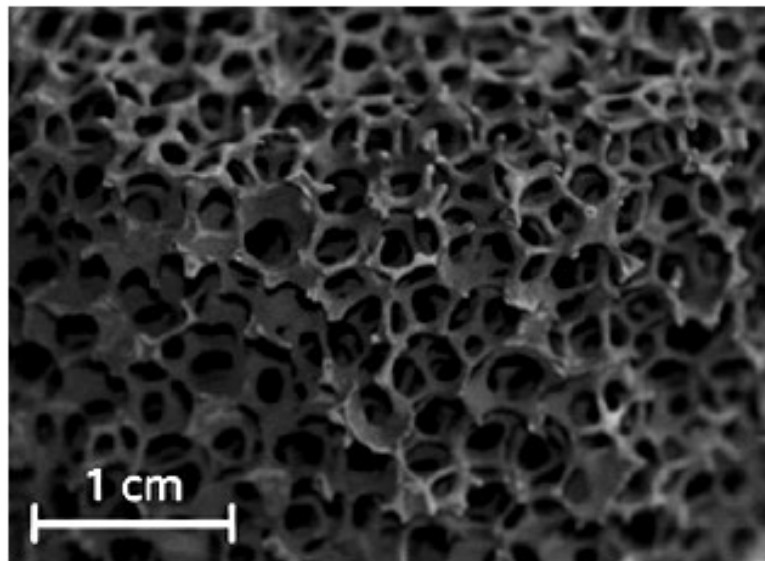
(b)

Fig. 4.1. Images of the pore-level features for (a) a medium obtained by calcining a pressed pellet composed of starch and ceria particles at 1773 K [18] (image courtesy of Nicholas D. Petkovich) and (b) a SiC reticulated porous ceramic [84]. The computed d_{32} values for these materials are 8.31 μm and 813 μm, respectively.
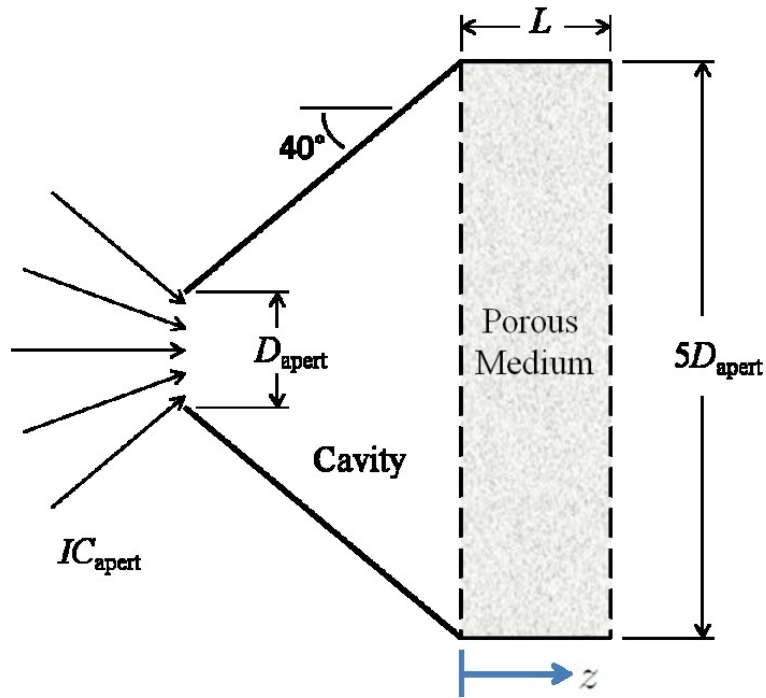
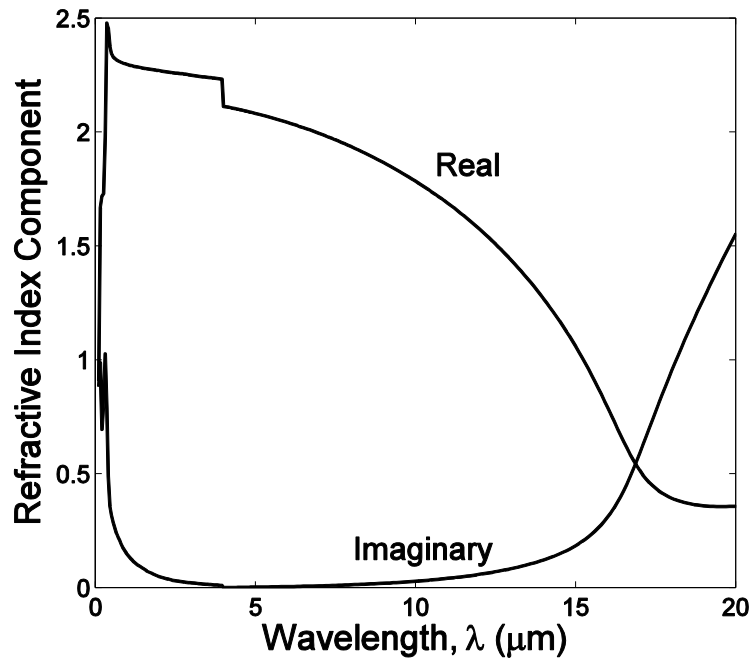Fig. 4.2. Schematic of the cavity and reactive medium configuration.
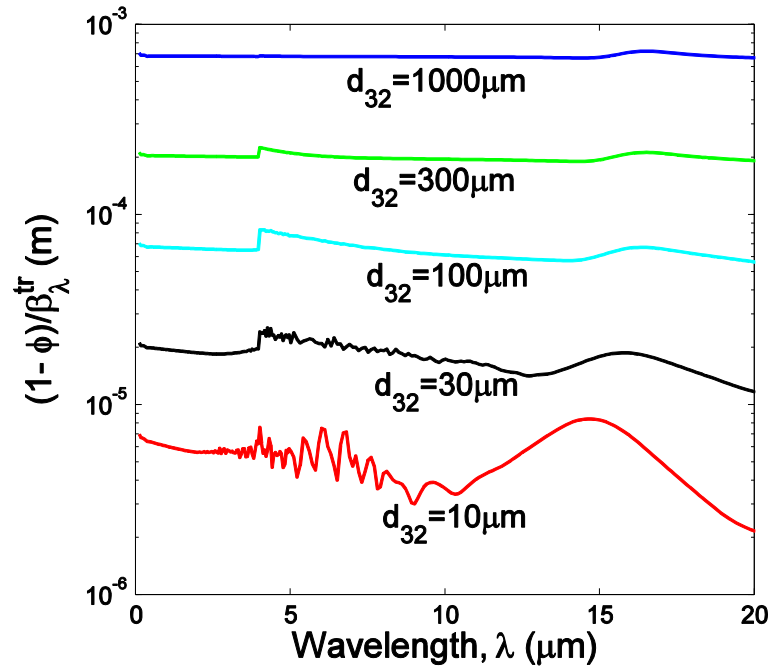

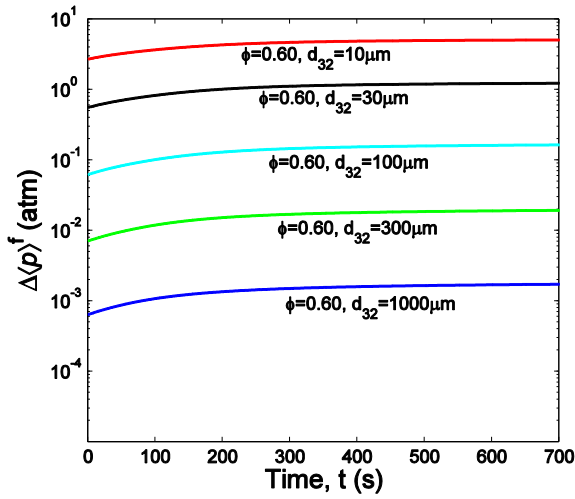Fig. 4.3. Spectral complex refractive index of cerium dioxide.

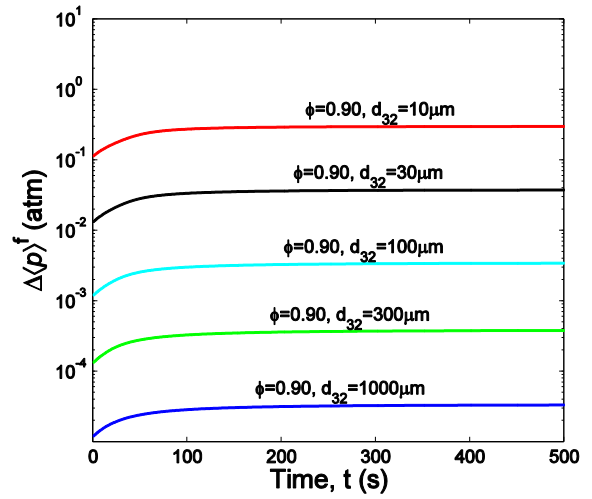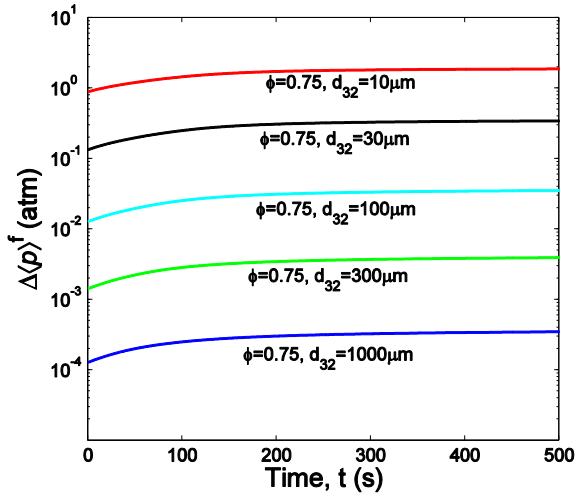Fig. 4.4. Porosity normalized spectral inverse transport extinction coefficients computed using Eq. (4.32). The factor $(1-\phi)$ accounts for the dependence on porosity, so $(1-\phi)/\beta_\lambda^{\text{tr}}$ depends only on the Sauter mean diameter and wavelength.

(a)

(b)

(c)

Fig. 4.5. Transient pressure drop for selected Sauter mean diameters between 10 μm and 1000 μm for a porosity of (a) 0.60, (b) 0.75, and (c) 0.90.
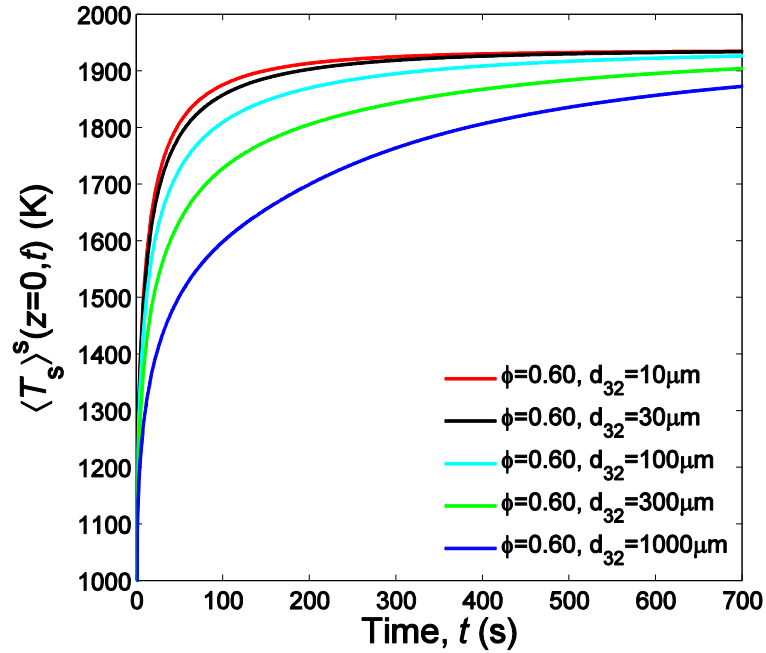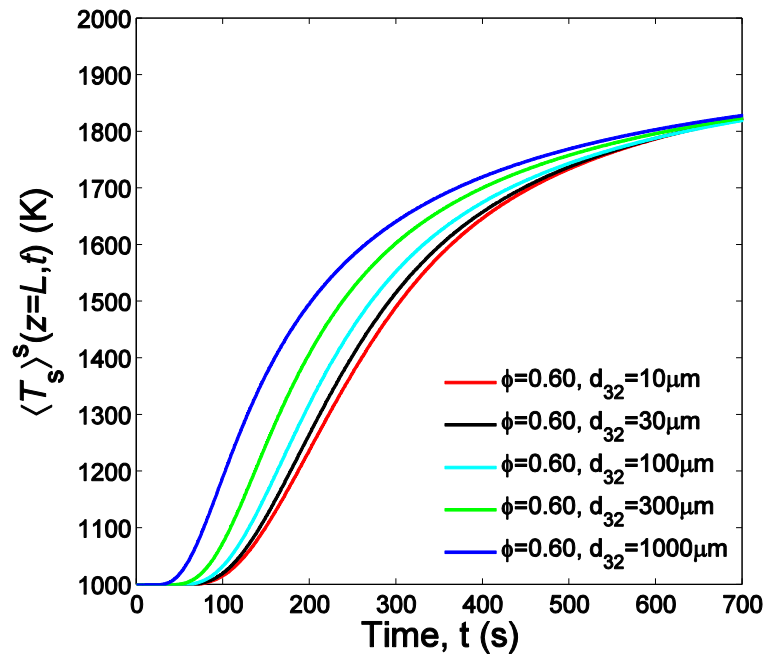
Fig. 4.6. The solid temperatures at the (a) $z = 0$ and (b) $z = L$ boundaries rise more rapidly and slowly, respectively, as the Sauter mean diameter decreases, indicative of the streamwise temperature gradient increasing with the extinction coefficient.
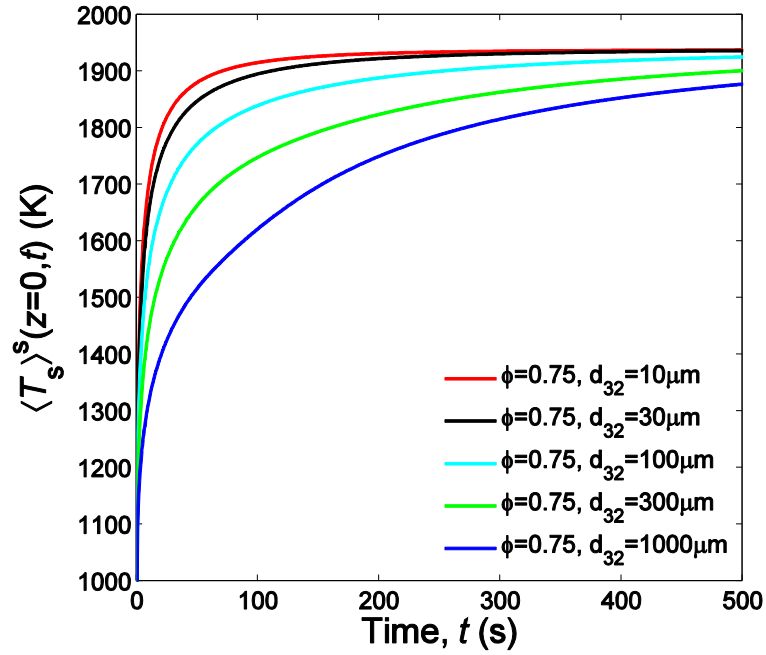
(a)
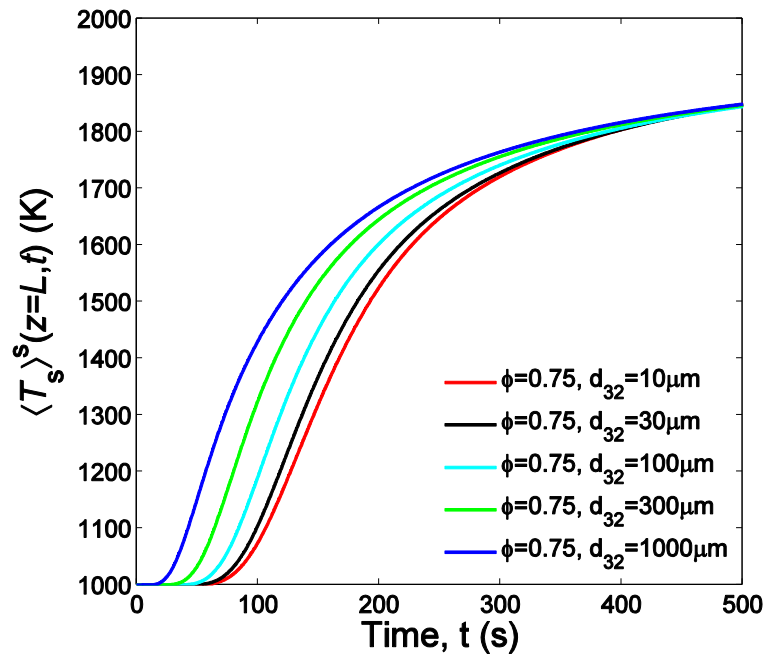
(b)

Fig. 4.7. The solid temperatures at the (a) $z = 0$ and (b) $z = L$ boundaries rise more rapidly and slowly, respectively, as the Sauter mean diameter decreases, indicative of the streamwise temperature gradient increasing with the extinction coefficient.
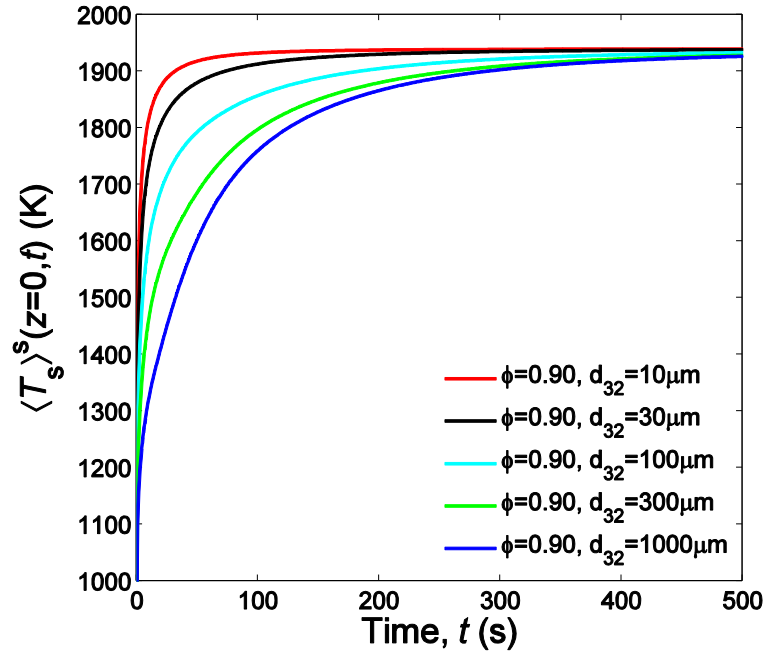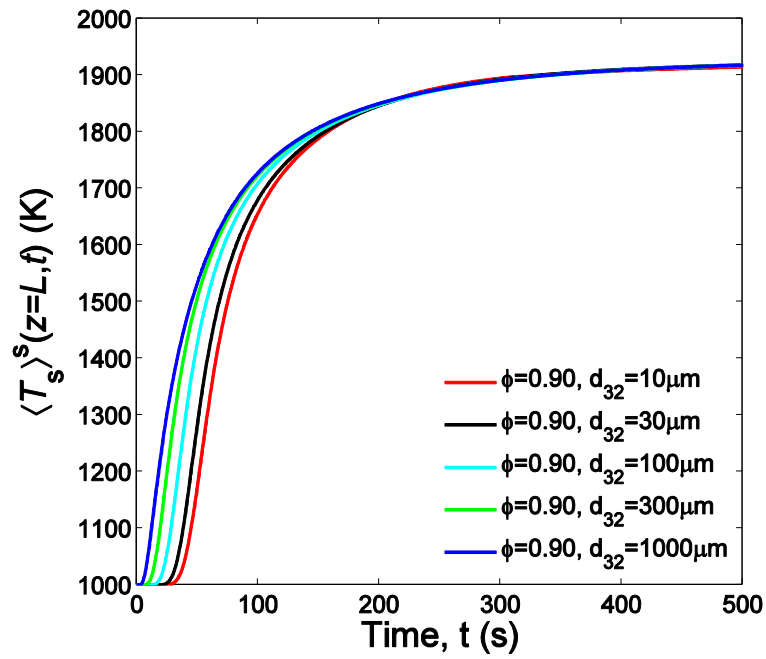
Fig. 4.8. The solid temperatures at the (a) $z = 0$ and (b) $z = L$ boundaries rise more rapidly and slowly, respectively, as the Sauter mean diameter decreases, indicative of the streamwise temperature gradient increasing with the extinction coefficient.

78
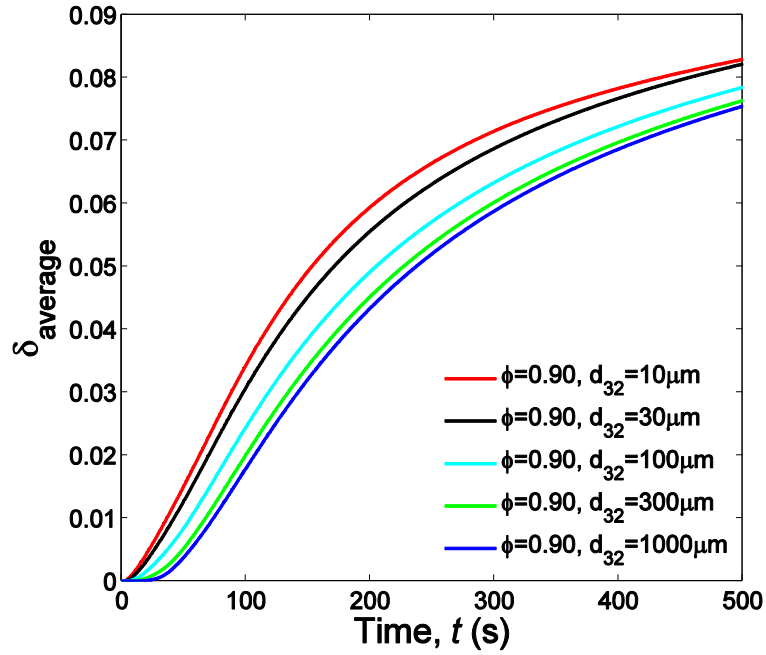
(a)
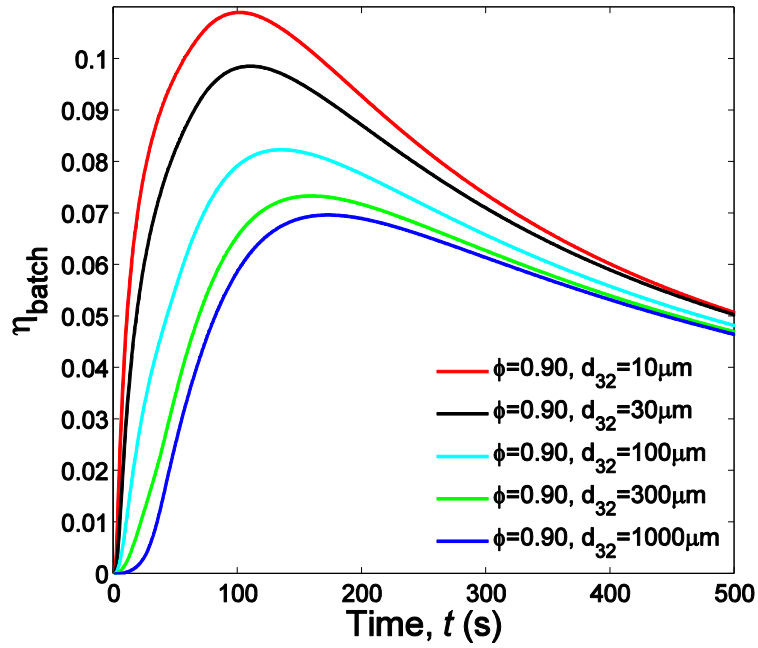
(b)

Fig. 4.9. The (a) average nonstoichiometry and (b) overall solar-to-chemical energy conversion for the process are plotted for $\phi = 0.90$.
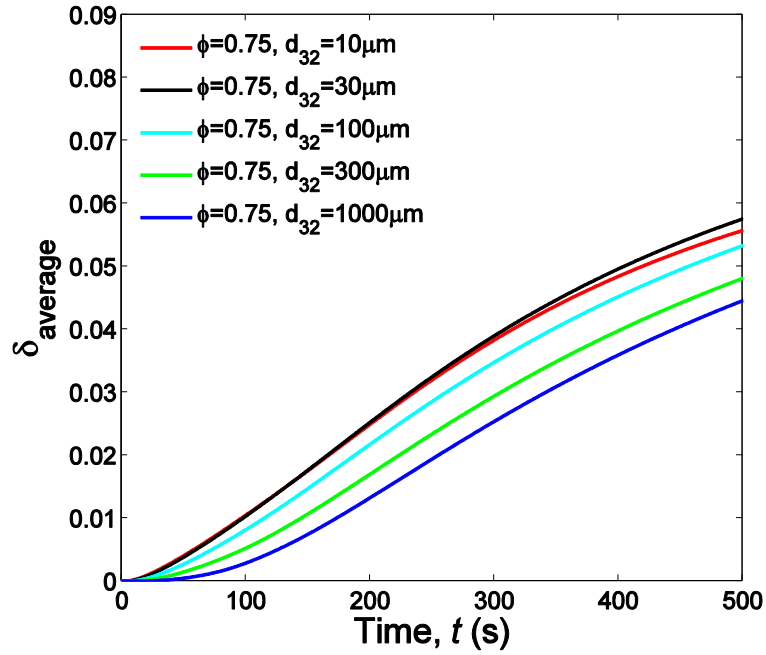
(a)
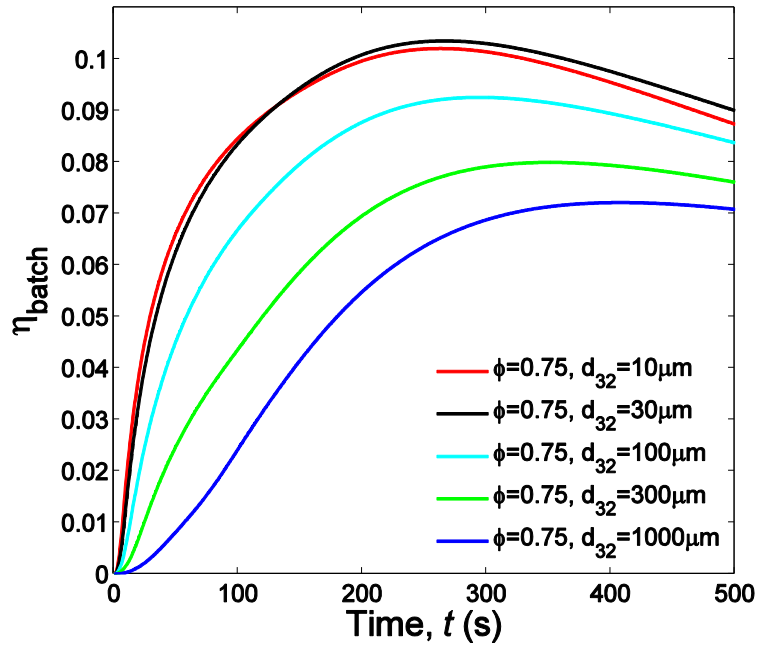
(b)

Fig. 4.10. The (a) average nonstoichiometry and (b) overall solar-to-chemical energy conversion for the process are plotted for $\phi = 0.75$.
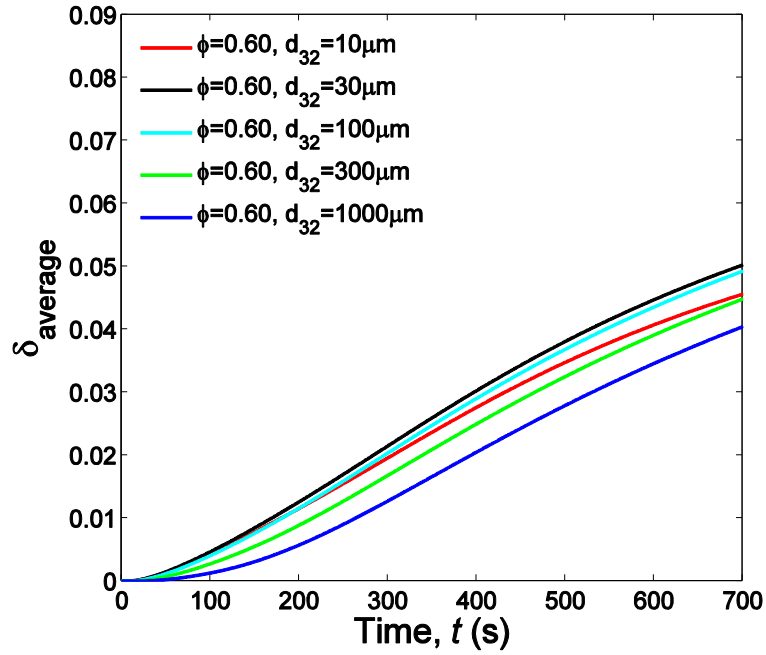
(a)
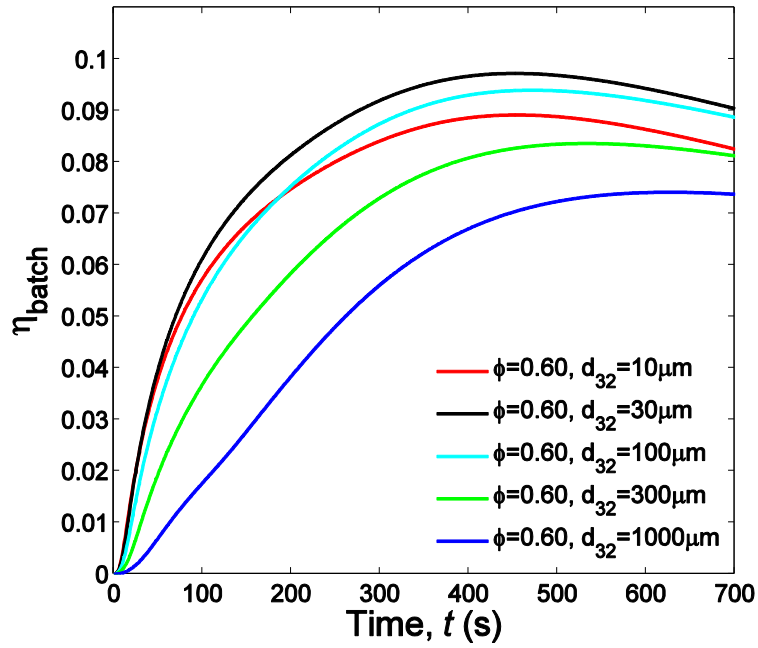
(b)

Fig. 4.11. The (a) average nonstoichiometry and (b) overall solar-to-chemical energy conversion for the process are plotted for $\phi = 0.60$.

Chapter 5

Kinetic Parameter Calibration for the Oxidation of Ceria

Introduction

During the fuel production step of the thermochemical cycle, an oxidizer feedstock is converted into a chemical fuel by repopulating the oxygen vacancies in the ceria lattice created during the reduction step. This oxidation step, being exothermic, becomes thermodynamically favored at temperatures significantly below those at which thermal reduction would be performed. However, the kinetics are anticipated to become more rapid as the temperature increases. Therefore, determining an appropriate compromise between these two competing interests will be a chief consideration for optimizing the performance of the solar thermochemical cycle. While the thermodynamics are known [72], the kinetics of oxidation have not been characterized to the extent that is needed to inform this optimization, and it is this gap that the present effort seeks to eliminate.

This chapter outlines a parameter calibration technique that has been developed to enable data from an experimental campaign aimed at characterizing the oxidation kinetics of ceria to be used to fully determine a reaction rate expression. The technique begins with using a set of volume-averaged governing equations that describe the transport and chemical processes within a porous medium in conjunction with boundary and initial conditions that are formulated to appropriately capture the experimental conditions. Due to the transient nature of the oxidation process, an axially-dispersed plug flow model [96] is applied to account for the dynamic response of the gas analysis instrument. Collectively, these pieces form a tool for evaluating the ability of a hypothesized reaction rate expression to match the experimental observations. Then, this simulation tool is coupled with an optimization algorithm to identify the kinetic parameters that yield the best agreement with the experimental data. Before presenting the details of this kinetic parameter calibration technique and the results from a demonstrative case, the experimental apparatus and procedure used to obtain the experimental data are described.

Experimental Methodology

The experimental work described in this section was carried out by Luke Venstrom, Daniel Boman, and Jane H. Davidson. It is described here in brief to give the reader context for the numerical work that was performed in the present study. To elucidate the influence of temperature on kinetics, ceria powder reduced chemically to a known nonstoichiometry is oxidized isothermally in a flow of fixed CO_2 concentration. Oxidizing ceria with the same initial nonstoichiometry ensures that global oxidation rate data collected at different temperatures are directly comparable.

Ceria Sample

Ceria powder is obtained by crushing a porous ceria monolith synthesized according to the procedure described in [18]. The particles are sieved to between 180 and 850 μm and have a porosity of 65%. The SEM image in Fig. 5.1 shows that the particles are porous with pores and solid feature sizes on the order of tens of micrometers. The microstructure of the ceria particles remains unchanged during testing due to a prolonged calcination at 1773 K.

Experimental Approach

The rate of oxidation of the ceria powder is measured in the packed bed reactor pictured in Fig. 5.2. The packed bed is held vertically in a quartz tube with a quartz frit (pore diameter 90-150 μm). The bed is 10.2 mm in diameter and 8.5 mm high. The overall porosity of the bed, including both interparticle and intraparticle void space, is 77%. The packed bed is heated in an electric furnace and temperature is monitored with a chromel-alumel, stainless-steel sheathed thermocouple probe (3.2 mm diameter) placed in contact with the top of the packed bed to monitor temperature. In a separate experiment, the variation in temperature over the length of the packed bed was measured by traversing the thermocouple probe along the tube axis. The temperature is maintained to within ±10 K over the length of the packed bed.

Gases flow through the packed bed from top to bottom and are delivered using mass flow controllers. The composition of the product gas exiting the reactor is measured using a Raman laser gas analyzer The reactor is heated and the ceria is reduced to

$\delta_i = 0.09 \pm 0.01$ using a flow composed of H_2, H_2O, and Ar at a nominal flow rate of 300 mL(STP) min^{-1}. Following reduction, the reactor is purged of H_2 and H_2O with an inert Ar flow and set to the desired oxidation temperature. Oxidation commences with a flow containing nominally 25 mol% CO_2. While keeping the Ar flow fixed, oxidation is commenced by combining CO_2 (99.99% purity) with the previously established purging flow of Ar and is terminated when the CO in the reactor effluent drops below the detectable limit of the gas analyzer by terminating the supply of CO_2.

Mathematical Model

Candidate Reaction Rate Expressions

Two candidate reaction rate expressions are formulated using the law of mass action and a hypothesized ionization state of the oxygen vacancies in the ceria lattice. The rates are formulated as reversible in order to satisfy chemical equilibrium. First, the splitting of carbon dioxide described by

$$CO_2(g) \leftrightarrow CO(g) + \frac{1}{2}O_2(g) \tag{5.1}$$

and the oxidation of ceria by oxygen described by

$$\lim_{\alpha \to 0} \frac{1}{\alpha} CeO_{2-\delta-\alpha}(s) + \frac{1}{2}O_2(g) \leftrightarrow \frac{1}{\alpha} CeO_{2-\delta}(s) \tag{5.2}$$

are combined to obtain

$$\lim_{\alpha \to 0} \frac{1}{\alpha} CeO_{2-\delta-\alpha}(s) + CO_2(g) \leftrightarrow \frac{1}{\alpha} CeO_{2-\delta}(s) + CO(g) \tag{5.3}$$
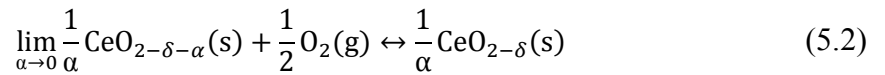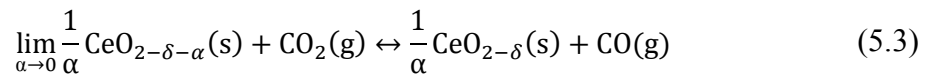
Note that reaction (5.3) suggests complete selectivity toward carbon monoxide (as opposed to carbon deposition), which is consistent with experimental observations

84

[18,32–34,40]. The molar Gibbs free energy changes associated with Eqs. (5.1) and (5.2) are designated by $\Delta \bar{g}_{CO_2}^0$ and $\frac{1}{2}\Delta \bar{g}_{O_2}^0$, respectively, where the latter is defined as

$$\Delta \bar{g}_{O_2}^0 = \bar{R}T \ln\left(\frac{p_{O_2}}{p_{ref}}\right) \tag{5.4}$$

in accordance with [72]. Consequently, the Gibbs free energy change associated with Eq. (5.3) is $\Delta \bar{g}_{CO_2}^0 + \frac{1}{2}\Delta \bar{g}_{O_2}^0$.

In the context of kinetics, combining Eqs. (5.1) and (5.2) to obtain Eq. (5.3) is akin to treating the gas phase oxygen as a reaction intermediate with the quasi-steady state approximation. At the temperatures and nonstoichiometries being considered for the fuel production step, the chemical equilibrium of reaction (5.2) makes the existence of gas phase oxygen highly unfavored; the equilibrium partial pressures of oxygen obtained from Eq. (5.4) are in the range of 10^{-12}–10^{-18} atm [72]. Consequently, a direct incorporation of oxygen into the lattice when carbon dioxide is converted to carbon monoxide as suggested by Eq. (5.3) is a reasonable approach.

If the oxygen vacancies in the ceria lattice are presumed to be doubly ionized, Eq. (5.3) can be alternatively represented using Kröger–Vink notation as

$$2Ce'_{Ce} + V_O^{\cdot\cdot} + CO_2(g) \leftrightarrow 2Ce_{Ce}^X + O_O^X + CO(g) \tag{5.5}$$
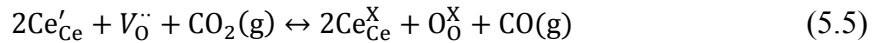
for which an equilibrium constant can be defined as

$$K_{KV,d} = \exp\left(-\frac{\Delta \bar{h}_{KV,d}^0 - T\Delta \bar{s}_{KV,d}^0}{\bar{R}T}\right) = \frac{[Ce_{Ce}^X]^2 [O_O^X]\left(\frac{p_{CO}}{p_{ref}}\right)}{[Ce'_{Ce}]^2 [V_O^{\cdot\cdot}]\left(\frac{p_{CO_2}}{p_{ref}}\right)} \tag{5.6}$$

where $[\text{Ce}_{\text{Ce}}^{\text{X}}]$ represents the fraction of cerium lattice sites occupied by neutrally charged cerium atoms, $[\text{Ce}'_{\text{Ce}}]$ designates the fraction of cerium sites occupied by cerium atoms in a 3+ valence state, $[\text{O}_{\text{O}}^{\text{X}}]$ designates the fraction of oxygen sites occupied by neutrally charged oxygen atoms, and $[V_{\text{O}}^{\cdot\cdot}]$ designates the fraction of oxygen sites that are vacant. Crystal site conservation requires $[\text{O}_{\text{O}}^{\text{X}}] + [V_{\text{O}}^{\cdot\cdot}] = 1$ and $[\text{Ce}_{\text{Ce}}^{\text{X}}] + [\text{Ce}'_{\text{Ce}}] = 1$ whereas electroneutrality requires $4[V_{\text{O}}^{\cdot\cdot}] = [\text{Ce}'_{\text{Ce}}]$. Making these substitutions into Eq. (5.6) and recognizing that the ratio between the number of vacant oxygen lattice sites and the number of cerium sites is the definition of the nonstoichiometry and can therefore be expressed as $\delta = 2[V_{\text{O}}^{\cdot\cdot}]$, the equilibrium constant corresponding to Eq. (5.5) becomes

$$K_{\text{KV,d}} = \exp\left(-\frac{\Delta \bar{h}_{\text{KV,d}}^0 - T\Delta\bar{s}_{\text{KV,d}}^0}{\bar{R}T}\right) = \frac{(1 - 2\delta)^2(1 - 0.5\delta)\left(\frac{p_{\text{CO}}}{p_{\text{ref}}}\right)}{(2\delta)^2(0.5\delta)\left(\frac{p_{\text{CO}_2}}{p_{\text{ref}}}\right)} \tag{5.7}$$

By recognizing the connection between the numerator of $K_{\text{KV,d}}$ and the products (RHS of Eq. (5.5)) and between the denominator of $K_{\text{KV,d}}$ and the reactants (LHS of Eq. (5.5)), an expression for the oxidation reaction rate is constructed in accordance with applying the law of mass action to Eq. (5.5), giving

$$\dot{m}_{\text{sf},i}'' = \nu_i M_i \dot{n}_{\text{sf},i}'' \tag{5.8}$$

$$= \nu_i M_i \frac{\dot{n}_{\text{sf},0}''}{2}\left[\frac{(1 - 2\delta)^2(1 - 0.5\delta)\left(\frac{p_{\text{CO}}}{p_{\text{ref}}}\right)}{K_{\text{KV,d}}} - (2\delta)^2(0.5\delta)\left(\frac{p_{\text{CO}_2}}{p_{\text{ref}}}\right)\right] \tag{5.9}$$

where ν_i is the stoichiometric coefficient used to obtain the correct sign for interphase mass transfer ($\nu_{\text{CO}_2} = 1, \nu_{\text{CO}} = -1$). An important feature of this result regarding reaction orders is that the partial pressure of carbon dioxide is multiplied with nonstoichiometry to the third power in the term accounting for CO_2 consumption. The thermodynamic functions defining $K_{\text{KV,d}}$ are determined by recognizing that Eqs. (5.3)

and (5.5) both represent the oxidation of ceria by carbon dioxide and that an equilibrium constant for the former is given by

$$\exp\left[-\frac{\left(\Delta\bar{h}_{CO_2}^0 + 0.5\Delta\bar{h}_{O_2}^0\right) - T\left(\Delta\bar{s}_{CO_2}^0 + 0.5\Delta\bar{s}_{O_2}^0\right)}{\bar{R}T}\right] = \frac{\frac{p_{CO}}{p_{ref}}}{\frac{p_{CO_2}}{p_{ref}}} \qquad (5.10)$$

Combining Eqs. (5.7) and (5.10) leads to

$$\Delta\bar{h}_{KV,d}^0 = \Delta\bar{h}_{CO_2}^0 + 0.5\Delta\bar{h}_{O_2}^0 \qquad (5.11)$$

$$\Delta\bar{s}_{KV,d}^0 = \Delta\bar{s}_{CO_2}^0 + 0.5\Delta\bar{s}_{O_2}^0 + \ln\frac{(1-2\delta)^2(1-0.5\delta)}{2\delta^3} \qquad (5.12)$$

which upon substituting into Eq. (5.10) gives the reaction rate expression corresponding to doubly ionized oxygen vacancies as

$$\dot{m}_{sf,i}'' = \nu_i M_i \dot{n}_{sf,0}'' \left[\exp\left(\frac{\Delta\bar{g}_{CO_2}^0 + 0.5\Delta\bar{g}_{O_2}^0}{\bar{R}T}\right)\left(\frac{p_{CO}}{p_{ref}}\right)\delta^3 - \left(\frac{p_{CO_2}}{p_{ref}}\right)\delta^3\right] \qquad (5.13)$$

This same process can also be applied to develop an analogous reaction rate expression when the oxygen vacancies are presumed to be singly ionized, in which case the overall reaction is expressed using Kröger–Vink notation as

$$Ce_{Ce}' + V_O^{\cdot} + CO_2(g) \leftrightarrow Ce_{Ce}^X + O_O^X + CO(g) \qquad (5.14)$$
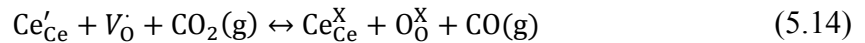
The corresponding equilibrium constant is given by

$$K_{KV,s} = \exp\left(-\frac{\Delta\bar{h}^0_{KV,s} - T\Delta\bar{s}^0_{KV,s}}{\bar{R}T}\right) = \frac{[Ce^X_{Ce}][O^X_O]\left(\frac{p_{CO}}{p_{ref}}\right)}{[Ce'_{Ce}][V^{\cdot}_O]\left(\frac{p_{CO_2}}{p_{ref}}\right)} \tag{5.15}$$

For singly ionized vacancies, electroneutrality requires $2[V^{\cdot}_O] = [Ce'_{Ce}]$ and $\delta = 2[V^{\cdot}_O]$, which when substituted into Eq. (5.15) gives

$$\dot{m}''_{sf,i} = \nu_i M_i \dot{n}''_{sf,i} \tag{5.16}$$

$$= \nu_i M_i \left(2\dot{n}''_{sf,0}\right)\left[\frac{(1-\delta)(1-0.5\delta)\left(\frac{p_{CO}}{p_{ref}}\right)}{K_{KV,s}} - (\delta)(0.5\delta)\left(\frac{p_{CO_2}}{p_{ref}}\right)\right] \tag{5.17}$$

which after relating the thermodynamic functions in $K_{KV,s}$ to those in Eq. (5.10), gives the final reaction rate expression for singly ionized vacancies as

$$\dot{m}''_{sf,i} = \nu_i M_i \dot{n}''_{sf,0}\left[\exp\left(\frac{\Delta\bar{g}^0_{CO_2} + 0.5\Delta\bar{g}^0_{O_2}}{\bar{R}T}\right)\left(\frac{p_{CO}}{p_{ref}}\right)\delta^2 - \left(\frac{p_{CO_2}}{p_{ref}}\right)\delta^2\right] \tag{5.18}$$

Comparing the forms of the reaction rate expressions obtained when the vacancies are assumed to be either singly or doubly ionized reveals that the only difference is the order on the nonstoichiometry. With respect to nonstoichiometry, singly ionized vacancies predict an order of two while doubly ionized vacancies predict an order of three.

Governing Equations

Because the oxidation of ceria by CO_2 occurs under nominally isothermal conditions, the energy equation(s) need not be solved. Rather, the solid and fluid temperatures are set equal to the temperature indicated by the thermocouple that is placed in contact with the packed bed. Consequently, only the mass conservation equations and Darcy's law need to be considered [81]. The solid phase conservation of mass equation is

$$\frac{\partial}{\partial t}\left\{\rho_{\mathrm{CeO_2}}(1-\phi)\frac{M_{\mathrm{O_2}}}{2M_{\mathrm{CeO_2}}}\langle\delta\rangle^{\mathrm{s}}\right\} = \dot{m}''_{\mathrm{sf}}a_{\mathrm{sf}} \tag{5.19}$$

while Darcy's law

$$-\nabla\big(\phi\langle p\rangle^{\mathrm{f}}\big) = \frac{\mu_{\mathrm{f}}\phi\langle\vec{u}\rangle}{K_{\mathrm{PBPP}}} \tag{5.20}$$

and the ideal equation of state for a multi-component mixture

$$\langle p\rangle^{\mathrm{f}} = \left(\sum_i \frac{\langle Y_i\rangle^{\mathrm{f}}}{M_i}\right)\langle\rho\rangle^{\mathrm{f}}\bar{R}\langle T_{\mathrm{f}}\rangle^{\mathrm{f}} \tag{5.21}$$

are combined with the fluid phase conservation of mass equation to obtain

$$\frac{\partial}{\partial t}\left\{\frac{\phi}{\left(\sum_i \frac{\langle Y_i\rangle^{\mathrm{f}}}{M_i}\right)\bar{R}\langle T_{\mathrm{f}}\rangle^{\mathrm{f}}}\langle p\rangle^{\mathrm{f}}\right\} = \nabla\cdot\left\{\frac{\frac{K_{\mathrm{PBPP}}}{\mu_{\mathrm{f}}\phi}}{\left(\sum_i \frac{\langle Y_i\rangle^{\mathrm{f}}}{M_i}\right)\bar{R}\langle T_{\mathrm{f}}\rangle^{\mathrm{f}}}\langle p\rangle^{\mathrm{f}}\nabla\big(\phi\langle p\rangle^{\mathrm{f}}\big)\right\} + \dot{m}''_{\mathrm{sf}}a_{\mathrm{sf}} \tag{5.22}$$

The subscript has been added to the permeability to highlight the context of a packed bed of porous particles; K_{PBPP} needs to relate the gradient of the pressure averaged over the entire fluid phase to the superficial velocity. The species mass equation for species i in the fluid phase is given by

$$\frac{\partial}{\partial t}\big(\phi\langle\rho\rangle^{\mathrm{f}}\langle Y_i\rangle^{\mathrm{f}}\big) + \nabla\cdot\big(\langle\rho\rangle^{\mathrm{f}}\langle\vec{u}\rangle\langle Y_i\rangle^{\mathrm{f}}\big) = \nabla\cdot\big(D_{i,\mathrm{eff}}\langle\rho\rangle^{\mathrm{f}}\nabla\langle Y_i\rangle^{\mathrm{f}}\big) + \dot{m}''_{\mathrm{sf},i}a_{\mathrm{sf}} \tag{5.23}$$

Unlike in thermal reduction, the fluid phase is not a binary gas mixture and so Eq. (5.23) must be applied to solve for more than one chemical species before calculating the argon mass fraction using

$$\langle Y_{Ar} \rangle^f = 1 - \sum_{i,\ i \neq Ar} \langle Y_i \rangle^f \tag{5.24}$$

The total interphase mass flux appearing in Eqs. (5.19) and (5.22) is related to the species interphase mass flux appearing in Eq. (5.23) according to

$$\dot{m}''_{sf} = \sum_i \dot{m}''_{sf,i} \tag{5.25}$$

The specific form of the interphase mass fluxes depends on the hypothesized reaction rate expression. These details are developed and presented in the Candidate Reaction Rate Expressions section.

In using these governing equations to model the experimental ceria sample, it is important to carefully interpret the porosity and effective transport properties in the context of a packed bed of porous particles. The porosity appearing in the governing equations, ϕ, is the total porosity and carries its usual definition as the ratio between the amount of void (fluid) and total volume. By distinguishing between interparticle and intraparticle void (fluid) volumes, the total porosity can be expressed as

$$\phi = \frac{V_{f,inter} + V_{f,intra}}{V_{total}} = \frac{V_{f,inter} + V_{f,intra}}{V_{f,inter} + V_{f,intra} + V_s} \tag{5.26}$$

which can be algebraically manipulated to obtain

$$\phi = \frac{V_{\text{f,inter}}}{V_{\text{total}}} + \frac{V_{\text{f,intra}}}{V_{\text{f,intra}} + V_{\text{s}}} \cdot \frac{V_{\text{total}} - V_{\text{f,inter}}}{V_{\text{total}}} \tag{5.27}$$

$$\phi = \phi_{\text{inter}} + \phi_{\text{intra}}(1 - \phi_{\text{inter}}) \tag{5.28}$$

The intraparticle porosity ϕ_{intra} is a straightforward extension of the usual porosity definition as applied to the porous particle. As stated earlier, the particles retain the porosity of the monoliths from which they were obtained, and so $\phi_{\text{intra}} = 0.65$. The interparticle porosity ϕ_{inter} characterizes the amount of void space between the particles as a consequence of how they are arranged to form the packed bed. Its value is calculated using Eq. (5.28) from knowledge of ϕ_{intra} and ϕ, the latter being determined from measurements of the total mass of the sample, diameter of the packed bed, length of the packed bed, and the density of ceria ($\rho_{\text{CeO}_2} = 7215$ kg m^{-3}). Just as the porosity is further qualified to obtain Eq. (5.28), the spatial averaging operator (with generic operand ψ) for the fluid phase is further qualified according to

$$\langle\psi\rangle^{\text{f}} = \frac{1}{V_{\text{f}}} \int_{V_{\text{f}}} \psi dV = \frac{1}{V_{\text{f}}} \int_{V_{\text{f,inter}}} \psi dV + \frac{1}{V_{\text{f}}} \int_{V_{\text{f,intra}}} \psi dV \tag{5.29}$$

$$= \frac{V_{\text{f,inter}}}{V_{\text{f}}} \left(\frac{1}{V_{\text{f,inter}}} \int_{V_{\text{f,inter}}} \psi dV \right) + \frac{V_{\text{f,intra}}}{V_{\text{f}}} \left(\frac{1}{V_{\text{f,intra}}} \int_{V_{\text{f,intra}}} \psi dV \right) \tag{5.30}$$

$$= \frac{V_{\text{total}}}{V_{\text{total}}} \left(\frac{V_{\text{f,inter}}}{V_{\text{f}}} \langle\psi\rangle^{\text{f,inter}} + \frac{V_{\text{f,intra}}}{V_{\text{f}}} \langle\psi\rangle^{\text{f,intra}} \right) \tag{5.31}$$

$$= \frac{\phi_{\text{inter}}\langle\psi\rangle^{\text{f,inter}} + \phi_{\text{intra}}(1 - \phi_{\text{inter}})\langle\psi\rangle^{\text{f,intra}}}{\phi_{\text{inter}} + \phi_{\text{intra}}(1 - \phi_{\text{inter}})} \tag{5.32}$$

The effective transport properties arising in the set of governing equations are the permeability and the effective diffusivity, which have been evaluated in recognition of the disparate length scales associated with the interparticle and intraparticle void volumes and the pore-level transport mechanisms anticipated to dominate in each [96,97]. The

length scale associated with the interparticle void volume (and particle diameter) is substantially greater than the length scale associated with the intraparticle void volume, which causes the interparticle voids to be a flow path with significantly less resistance. Consequently, the advective mass flux through the bed will be dominated by flow through the interparticle voids while the fluid in the intraparticle voids will be essentially stagnant (and rely on diffusion to deliver/remove the reactants/products throughout the particle). Under these conditions, it is reasonable to assume that for the purposes of analyzing the resistance to flow through the interparticle voids, the union of the solid phase and the intraparticle void can be treated as if it were entirely composed of a solid. Analyzing this packed bed of hypothetically solid particles using Darcy's law leads to

$$-\nabla\big(\phi_{\text{inter}}\langle p\rangle^{\text{f,inter}}\big) = \frac{\mu_{\text{f}}\phi_{\text{inter}}\langle \vec{u}\rangle}{K} \tag{5.33}$$

where the superscript qualifies the averaging operator, indicating that the spatial averaging of the pressure is carried out only over the interparticle fluid volume. The permeability appearing in Eq. (5.33) is evaluated using the hydraulic radius approach, which for the packed bed of hypothetically solid particles gives

$$K = \frac{\phi_{\text{inter}}^3}{k_K a_{\text{sf}}} = \frac{\phi_{\text{inter}}^3 d_{\text{p}}^2}{36 k_K (1 - \phi_{\text{inter}})^2} \tag{5.34}$$

To relate K and K_{PBPP}, the quantities in Eq. (5.33) are related to those in Eq. (5.20). The superficial velocities in Eqs. (5.20) and (5.33) are inherently equivalent. In accordance with the assumption that the intraparticle fluid is stagnant, it is reasonable to anticipate that the intraparticle and interparticle region will have equal pressures, which upon applying Eq. (5.32) leads to $\langle p\rangle^{\text{f,inter}} = \langle p\rangle^{\text{f,intra}} = \langle p\rangle^{\text{f}}$. Lastly, all porosities are assumed to be spatially invariant. Consequently, the permeability of the packed bed of porous particles is evaluated using

$$K_{\text{PBPP}} = \frac{\phi_{\text{inter}}^3 d_{\text{p}}^2}{36 k_K (1 - \phi_{\text{inter}})^2} \tag{5.35}$$

The anticipated transport modes in the intraparticle and interparticle regions also provide the context for interpreting each term in Eq. (5.23), including the effective diffusivity $D_{i,\text{eff}}$. As argued above, the velocity is anticipated to be non-negligible only in the interparticle region. For this scenario, the advective flux appearing in Eq. (5.23) would need to be calculated using the density and mass fraction in the interparticle region only, according to $\langle \rho \rangle^{\text{f,inter}} \langle \vec{u} \rangle \langle Y_i \rangle^{\text{f,inter}}$. However, this expression is equivalent to the one appearing in Eq. (5.23) when the density and mass fractions in the interparticle and intraparticle regions are equal. The mass fractions in the interparticle and intraparticle regions will be equal provided that mass transfer is sufficiently fast to eliminate any gradients that the gas-solid reaction acts to create. Comparisons of the mass transfer and chemical time scales using the Wagner modulus have revealed that mass transfer is indeed sufficiently fast to satisfy this condition so that $\langle Y_i \rangle^{\text{f,inter}} = \langle Y_i \rangle^{\text{f,intra}} = \langle Y_i \rangle^{\text{f}}$. Due to the interparticle and intraparticle temperatures, pressures, and mass fractions being equal, Eq. (5.21) shows that the fluid densities will be equal as well. Therefore, the advective flux in Eq. (5.23) appropriately accounts for the advection of species i through the interparticle voids. Although mass diffusion through the intraparticle voids is expected to be fast relative to the chemistry, the intraparticle voids are expected to be a more tortuous path for diffusion than the interparticle voids when considering mass transport by diffusion on the scale of the bed (as captured by the first term on the RHS of Eq. (5.23)). Therefore, the effective mass diffusivity is evaluated according to

$$D_{i,\text{eff}} = \phi_{\text{inter}} D_i \tag{5.36}$$

where the effective binary diffusion coefficient for species i in the multi-component mixture is calculated using

$$D_i = \frac{1 - X_i}{\sum_{j, j \neq i} \dfrac{X_j}{D_{ij}}} \tag{5.37}$$

where D_{ij} is the binary diffusion coefficient which is calculated using Chapman–Enskog theory [68].

Boundary and Initial Conditions

This gravitationally stable vertical orientation of the reactor allows the packed bed to maintain its cylindrical shape and remain in contact with the lateral wall, which in light of the particle diameters used, is sufficient to minimize any edge effect of bypass flow [98]. Furthermore, the lateral quartz wall is impermeable. Therefore, radial gradients within the packed bed are neglected in the model and the behavior is treated as one-dimensional. Consequently, boundary conditions for Eqs. (5.22)–(5.23) are needed only at the inlet ($z = 0$) and outlet ($z = L$) boundaries.

At the inlet, the total mass flux provides the boundary condition for Eq. (5.22) as

$$\left(\frac{\langle p \rangle^{\mathrm{f}}}{\left(\sum_i \frac{\langle Y_i \rangle^{\mathrm{f}}}{M_i} \right) \bar{R} \langle T_{\mathrm{f}} \rangle^{\mathrm{f}}} \frac{K_{\mathrm{PBPP}}}{\mu_{\mathrm{f}} \phi} \frac{\partial \left(\phi \langle p \rangle^{\mathrm{f}} \right)}{\partial z} \right) \Bigg|_{z=0} = (\rho_{\mathrm{f}} u_z)_0 \tag{5.38}$$

while the mass flux of species i provides the boundary condition for Eq. (5.23) as

$$\left(\langle \rho \rangle^{\mathrm{f}} \langle u_z \rangle \langle Y_i \rangle^{\mathrm{f}} - \langle \rho \rangle^{\mathrm{f}} D_{i,\mathrm{eff}} \frac{\partial \langle Y_i \rangle^{\mathrm{f}}}{\partial z} \right) \Bigg|_{z=0} = (\rho_{\mathrm{f}} u_z Y_i)_0 \tag{5.39}$$

Both $(\rho_{\mathrm{f}} u_z)_0$ and $(\rho_{\mathrm{f}} u_z Y_i)_0$ vary in time to capture the transient associated with commencing the flow of oxidizer into the packed bed. Their values are determined using

the experimental data in conjunction with the application of the instrument response model, as described in the Instrument Response Model section.

At the outlet, the pressure is set to atmospheric and the mass fraction gradients are set to zero. Using this customary upwinding treatment for the mass fractions allows the effluent composition to be obtained from the solution rather than imposed upon it, which is important because it allows for a comparison of the numerically predicted effluent composition and the experimental data.

The initial conditions for Eqs. (5.19), (5.22), and (5.23) are shown in Table 5.1 and are formulated to allow the simulation to begin just as the carbon dioxide is introduced. The initial nonstoichiometry in the bed is set to a uniform value that is calculated from the experimentally measured gravimetric fuel production. The mass fractions are also set to a uniform value based on the composition of the purge gas, which is assumed to be argon with trace amounts of carbon dioxide and carbon monoxide. The pressure and velocity fields listed in Table 5.1 correspond to the steady state analytical solution obtained from solving Eqs. (5.22) and (5.20), respectively, for the case of no interphase mass flux (i.e., no chemical reaction) and uniform mass fraction and temperature fields. The initial pressure and velocity fields are expressed in a compact form by defining

$$p_{0,i}^2 = p_L^2 + \frac{2\mu_f L}{K_{\text{PBPP}}} (\rho u_z)_0 \left(\sum_i \frac{Y_{i,i}}{M_i} \right) \bar{R} T_f.$$ Strictly speaking, the specified initial nonstoichiometry value does not correspond to chemical equilibrium, and so there will be a small interphase mass flux. This minor inconsistency with the assumption used to obtain the steady state analytical solution that is used for the initial conditions is tolerated because the interphase mass flux is small. The impact of this small inconsistency in the initial conditions is further decreased by waiting 1 s after the flow of carbon dioxide into the bed begins increasing before making a comparison with the experimental data. This 1 s wait is big relative to the residence time for gases flowing through the packed bed (30 ms) but also small relative to the time required to completely oxidize the ceria (> 30 s).

Solution Method

The finite volume method [77,78] is used to discretize the governing equations in space. The solutions are obtained using an in-house developed Fortran code that employs

a staggered grid with the linear (central difference) interpolation scheme. Time integration is performed using the implicit Euler method in order to accommodate the disparate time scales and control the action of the nonlinear source terms. The latter allows for enforcing the positivity criterion on pressure, mass fractions, and temperatures as outlined in [81]. The coupled nature of the governing equations is addressed by sequentially solving Eqs. (5.19), (5.23), and (5.22) to update $\langle\delta\rangle^{s}$, $\langle Y_i\rangle^{f}$, and $\langle p\rangle^{f}$, respectively. Then, Eqs. (5.20) and (5.21) are used to update $\langle\vec{u}\rangle$ and $\langle\rho\rangle^{f}$, respectively to complete an outer iteration. Outer iterations are repeated until the L^2 norm of the relative changes in $\langle\delta\rangle^{s}$, $\langle Y_{O_2}\rangle^{f}$, and $\langle p\rangle^{f}$ between two successive outer iterations are all less than 10^{-6}.

Instrument Response Model

The transient nature of the composition of the effluent when oxidizing the packed bed of ceria particles may not be directly captured by the gas analysis equipment due to the possibility of mixing/dispersive processes occurring between the outlet of the packed bed and the inlet to the Raman laser gas analyzer as well as the dynamic response of the instrument itself. Because the numerical simulations provide a prediction of the gas composition at the outlet of the packed bed, these aspects of the experimental apparatus must be accounted for when comparing with the experimental data.

The significance of the mixing/dispersion and/or instrument response behavior has been experimentally investigated using "step input" tests wherein a steady flow of carbon dioxide is abruptly added to (or subtracted from) a steadily flowing stream of argon using a three-way valve placed upstream of the Raman laser gas analyzer inlet. Despite a rapid actuation of the valve, the experimental data feature a gradual rather than abrupt change as shown in Fig. 5.3 for a case where carbon dioxide was suddenly added to a steadily flowing stream of argon. The axially-dispersed plug flow model was used to capture the gradual decline of the argon mole fraction by evaluating the convolution of the "step input" profile $X_{Ar,input}(t)$ with the residence time distribution $E(t)$ according to

$$X_{Ar,disp}(t) = X_{Ar,input,i} + \left(X_{Ar,input}(t) - X_{Ar,input,i}\right) * E(t) \tag{5.40}$$

$$= X_{Ar,input,i} + \int_0^t \left(X_{Ar,input}(t') - X_{Ar,input,i}\right) E(t - t')\, dt' \tag{5.41}$$

where $X_{Ar,input,i}$ is the initial inlet argon mole fraction (i.e., $X_{Ar,input}(t = 0)$) and the residence time distribution of the axially-dispersed plug flow model is given by

$$E(t) = \left(\frac{Pe_{disp}}{4\pi} \frac{1}{t_{res}t}\right)^{\frac{1}{2}} \exp\left[-\frac{Pe_{disp}\left(1 - \frac{t}{t_{res}}\right)^2}{4\frac{t}{t_{res}}}\right] \tag{5.42}$$

By treating the transient input profile $X_{Ar,input}(t)$ as a (rapid) first order decay from its initial to final value, a two-dimensional optimization was performed to determine the values of t_{res} and Pe_{disp} that provide the excellent agreement shown in Fig. 5.3.

The calibration procedure used to formulate the boundary conditions for Eqs. (5.22) and (5.23) and determine the residence time distribution function parameters for a specific data set will now described. The delivery of carbon dioxide used to commence the oxidation experiments is presumed to follow a first order rise given by

$$X_{CO_2}(t)\big|_{z=0} = X_{CO_2,i} + \left(X_{CO_2,steady} - X_{CO_2,i}\right)\left[1 - \exp\left(-\frac{t}{\tau}\right)\right] \tag{5.43}$$

while the amount of carbon monoxide is held at a constant small value, which gives

$$X_{Ar}(t)\big|_{z=0} = 1 - X_{CO_2}(t)\big|_{z=0} - X_{CO}\big|_{z=0} \tag{5.44}$$

Upon converting these mole fractions into mass fractions, the total mass flux is calculated using

$$(\rho_f u_z)_0 = (\rho_f u_z Y_{Ar})_0 / Y_{Ar} \tag{5.45}$$

The short residence times of the gases flowing through the packed bed lead to quasi-steady behavior (i.e., negligible accumulation/storage effects) for the fluid phase, which allows the mole fractions at the outlet to be calculated from those at the inlet according to

$$\left(X_{CO_2}(t) + X_{CO}(t)\right)\big|_{z=L} = \left(X_{CO_2}(t) + X_{CO}\right)\big|_{z=0} \tag{5.46}$$

which can also be thought of as a carbon mass balance. Using the definition of the argon mole fraction at the outlet

$$X_{Ar}(t)|_{z=L} = 1 - X_{CO_2}(t)\big|_{z=L} - X_{CO}(t)|_{z=L} \tag{5.47}$$

combined with Eq. (5.46) gives

$$X_{Ar}(t)|_{z=L} = 1 - X_{CO_2}(t)\big|_{z=0} - X_{CO}|_{z=0} \tag{5.48}$$

which when combined with Eq. (5.44) gives

$$X_{Ar}(t)|_{z=L} = X_{Ar}(t)|_{z=0} \tag{5.49}$$

Therefore, when the gas flows through the packed bed are treated as quasi-steady, the argon mole fraction at the outlet is equal to the argon mole fraction at the inlet. With this result, the values of t_{res} and Pe_{disp} that lead to good agreement between the experimentally measured argon mole fractions and their numerically predicted counterparts computed using

$$X_{Ar,disp}(t) = X_{Ar,i} + \left(X_{Ar}(t)|_{z=0} - X_{Ar,i}\right) * E(t) \qquad (5.50)$$

$$= X_{Ar,i} + \left[\left(X_{Ar,steady} - X_{Ar,i}\right)\left(1 - \exp\left(-\frac{t}{\tau}\right)\right)\right] * E(t) \qquad (5.51)$$

are determined.

To obtain a numerical prediction of the gas composition measured by the Raman laser gas analyzer, the axially-dispersed plug flow model is applied to the mole fractions obtained by solving Eqns. (5.19), (5.22), and (5.23) using the conditions described in the Boundary and Initial Conditions section and the candidate reaction rate of choice. Note that the quasi-steady approximation is used only to relate the compositions at the two boundaries to enable the determination of t_{res} and Pe_{disp}; the quasi-steady approximation is not used when solving Eqns. (5.19), (5.22), and (5.23).

Optimization Algorithm

The rate constant $\dot{n}''_{sf,0}$ appearing in Eqs. (5.13) and (5.18) is the only unknown kinetic parameter in these candidate reaction rate expressions and it is expected to depend solely on temperature. Therefore, to compare with experimental data obtained under isothermal conditions, $\dot{n}''_{sf,0}$ will be constant and the determination of its value becomes an exercise in one-dimensional optimization.

The value of $\dot{n}''_{sf,0}$ is determined by coupling the in-house Fortran code used to solve the governing equations and apply the instrument response model with the general optimization program GenOpt [99] to implement the Golden Section Interval Division algorithm. This algorithm involves successively narrowing an initial search interval until the width of the interval containing the optimal value of $\dot{n}''_{sf,0}$ is less than a desired tolerance. The optimal value of $\dot{n}''_{sf,0}$ is defined as the value which minimizes the objective function used to quantify the agreement between the experimental data and the numerical predictions. This objective function is defined as the root mean square of the differences between the subset of the experimental measurements of the carbon

monoxide mole fraction considered and the corresponding numerically predicted values. As discussed earlier in the Boundary and Initial Conditions section, the initial carbon monoxide mole fraction is not included in the objective function to minimize the influence of the fluid phase initial conditions. The midpoint of the final interval is taken as the optimal value with the width of the final interval defining the uncertainty associated with the optimization.

Results for Oxidation at $T = 1203$ K

To demonstrate the developed kinetic parameter calibration technique, the kinetic rate constant for each of the candidate reaction rate expressions has been obtained for a temperature of 1203 K. The level of agreement with the experimental data is presented and profiles from the numerical solution are plotted to visualize the dynamics of oxidation. All simulations were performed using a time step size of 10^{-2} s on a uniform grid comprising 100 cells, which is sufficiently fine to accurately resolve the encountered gradients in the solution.

Sensitivity to Different Reaction Orders on δ

The experimentally measured argon mole fractions and numerically predicted counterparts used to determine the two parameters of the residence time distribution are shown in Fig. 5.4. In contrast to the step input test results shown in Fig. 5.3, the decline in the argon (rise in the carbon dioxide) mole fraction at the inlet during the oxidation experiment begins to slow and experiences a nearly linear region before reaching its steady value. Although this feature is not perfectly captured by the first order rise and axially-dispersed plug flow model, the agreement is still quite good; the difference between the predicted and experimental mole fraction values is always less than 0.015.

Figure 5.5 compares the experimentally measured carbon monoxide mole fractions and their numerically predicted counterparts using the doubly ionized reaction rate expression (Eq. (5.13)). The rate constant was set to $\dot{n}''_{sf,0} = 9.45939 \times 10^{-3}$ kmol m^{-2} s^{-1}, which is the value determined by minimizing the root mean square error between the numerically predicted and experimentally measured carbon monoxide mole fractions for the 29 data points shown in Fig. 5.5. The uncertainty in this rate constant associated with

the size of the final search interval is $\pm\, 0.00003 \times 10^{-3}$ kmol m^{-2} s^{-1}. The agreement is good at early times when X_{CO} is increasing, but the numerical data display a different curvature and consistently underpredict the experimental values for a majority of the interval during which fuel is being produced. At later times, both sets begin to asymptote as the chemical reaction approaches equilibrium, but the numerical data do this more gradually than the experimental data. The root mean square error associated with the differences in the carbon monoxide mole fractions that are experimentally measured and numerically predicted for the doubly ionized reaction rate expression is 0.007104 while the greatest error at any one point within the set is 0.013583.

The numerically predicted carbon monoxide mole fraction at the outlet of the packed bed is also plotted to reveal its significant difference from the measured values. The abrupt introduction of carbon dioxide that commences the production of fuel (CO) is treated as a first order rise with a time constant of $\tau = 0.02$ s, and the rise in the carbon monoxide at the outlet is just as rapid, after which it monotonically decreases over time.

Figure 5.6 presents the results obtained with the singly ionized reaction rate expression ((5.18)) when the kinetic rate constant is set to the value determined by optimization, which is 6.14228×10^{-4} kmol m^{-2} s^{-1}. The uncertainty in this rate constant associated with the size of the final search interval is $\pm\, 0.00004 \times 10^{-4}$ kmol m^{-2} s^{-1}. The predictions agree extremely well with the experimental measurements when using the singly ionized reaction rate expression; the root mean square error is 0.002082 while the greatest error at any one point is 0.006398. These errors are less than half those associated with using the doubly ionized reaction rate. Once again, the carbon monoxide mole fraction at the outlet of the packed bed rapidly attains its maximum as the carbon dioxide is abruptly introduced and then monotonically decreases over time.

Numerical Simulation Results

Although the primary focus of the oxidation simulations has been to determine kinetic parameters, the simulations can also provide additional insights into the dynamics of the oxidation process. In particular, the presence of gradients can be clearly analyzed by plotting the axial distributions of partial pressures, nonstoichiometry, and reaction rate.

101

The carbon dioxide and carbon monoxide partial pressures obtained using the singly ionized reaction rate expression are presented in Fig. 5.7 and Fig. 5.8, respectively. In addition to their importance in driving the reaction, the partial pressures provide insight into the gas composition because the pressure drop across the bed is insignificant (< 0.015 atm). Furthermore, the low pressure drop indicates that the permeability is sufficiently high to make the results insensitive to its value. Therefore, the level of approximation used in evaluating K_{PBPP} is acceptable. At early times, the large number of oxygen vacancies promotes a more rapid reaction rate, which causes the carbon dioxide partial pressure to decrease in the streamwise direction as the oxidizer is consumed. As more oxygen vacancies are filled, the reaction slows, leading to a decreased fractional conversion of carbon dioxide to carbon monoxide and a more uniform gas composition throughout the packed bed. The evolution of the carbon monoxide profiles are driven by the same dynamics because carbon monoxide production is tied to carbon dioxide consumption. The rapid reaction rate at early times leads to a strong streamwise increase in the carbon monoxide partial pressure because the carbon monoxide being produced throughout the bed accumulates as it is swept downstream.

The time evolution of the nonstoichiometry and reaction rate profiles obtained using the singly ionized reaction rate expression are shown in Fig. 5.9 and Fig. 5.10, respectively. Although the nonstoichiometry is initially uniform, a gradient is quickly established because the large initial nonstoichiometry creates a rapid reaction in the presence of an oxidizer. The high nonstoichiometry creates a reaction that is sufficiently fast to significantly deplete the carbon dioxide and produce carbon monoxide as seen in Fig. 5.7 and Fig. 5.8, respectively, and so the reaction rate magnitude rapidly decreases in the streamwise direction, despite an increased amount of oxygen vacancies. As the oxygen vacancies become filled and the reaction slows, more oxidizer becomes available to downstream locations. The location of the peak reaction rate moves through the packed bed as the optimal balance between abundant oxidizer with limited oxygen vacancies and abundant oxygen vacancies with limited oxidizer continues to travel downstream.

The results obtained using the doubly ionized reaction rate expression are also presented in Figs. 5.11–5.14 for comparison. The trends and features are the same in

102

essentials as those seen in Figs. 5.7–5.10, which is attributed to using the kinetic rate constants that were each obtained by performing an optimization to achieve agreement with a common set of experimental data.

Conclusion

The effluent composition associated with the oxidation of ceria at a temperature of 1203 K displays transients that are sufficiently fast to require a correction for the undesired convolution introduced by mixing/dispersive processes and/or the dynamic response of the Raman laser gas analyzer. The axially-dispersed plug flow model performs well for matching experimental data, but only after determining the optimal values of the residence time distribution parameters, which are not universal but rather depend on the data being used for comparison.

A reversible reaction rate expression based on the law of mass action for singly ionized oxygen vacancies compares very well with experimental data. Relative to the doubly ionized oxygen vacancy expression, the alternative singly ionized oxygen vacancy expression provides a superior fit to the data. The kinetic rate constants that give the best agreement with the experimental data at 1203 K for the singly (Eq. (5.18)) and doubly (Eq. (5.13)) ionized oxygen vacancies are $\dot{n}''_{sf,0} = (6.14228 \pm 0.00004) \times 10^{-4}$ kmol $m^{-2} s^{-1}$ and $(9.45939 \pm 0.00003) \times 10^{-3}$ kmol $m^{-2} s^{-1}$, respectively.

Analyzing the partial pressure, nonstoichiometry, and reaction rate profiles shows that even with short residence times, the rapid kinetics associated with large nonstoichiometries can create significant gradients within the packed bed that prohibit analyzing the packed bed using the concept of a differential reactor.

Table 5.1. Initial conditions.

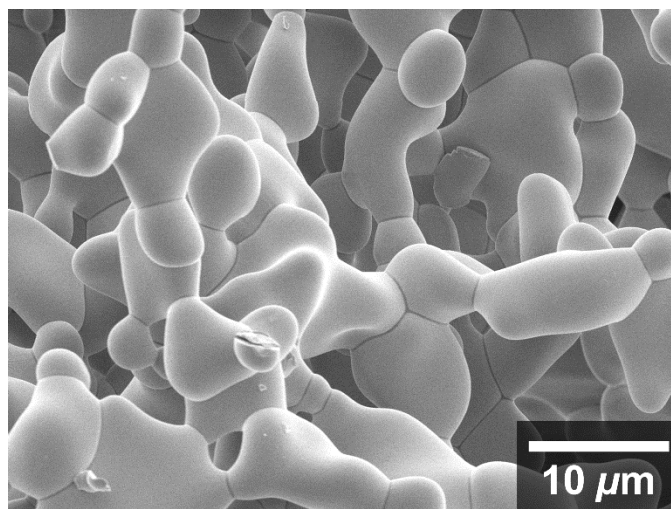| Variable	Initial Value
nonstoichiometry	$\langle \delta \rangle^s = \delta_i$
argon mass fraction	$\langle Y_{Ar} \rangle^f = Y_{Ar,i}$
carbon dioxide mass fraction	$\langle Y_{CO_2} \rangle^f = Y_{CO_2,i}$
carbon monoxide mass fraction	$\langle Y_{CO} \rangle^f = Y_{CO,i}$
pressure	$\dfrac{\langle p \rangle^f}{p_{0,i}} = \left\{ 1 - \left(1 - \left(\dfrac{p_L}{p_{0,i}} \right)^2 \right) \dfrac{z}{L} \right\}^{1/2}$
axial velocity	$\langle u_z \rangle = \dfrac{\dfrac{1}{2} \dfrac{p_{0,i} K_{PBPP}}{\mu_f L} \left(1 - \left(\dfrac{p_L}{p_{0,i}} \right)^2 \right)}{\left\{ 1 - \left(1 - \left(\dfrac{p_L}{p_{0,i}} \right)^2 \right) \dfrac{z}{L} \right\}^{1/2}}$

Fig. 5.1. Scanning electron micrograph of the porous CeO_2 sample at 2,500X (porous monolith synthesized in the laboratory of Prof. Sossina Haile at Caltech, image courtesy of Nicholas D. Petkovich at the University of Minnesota).
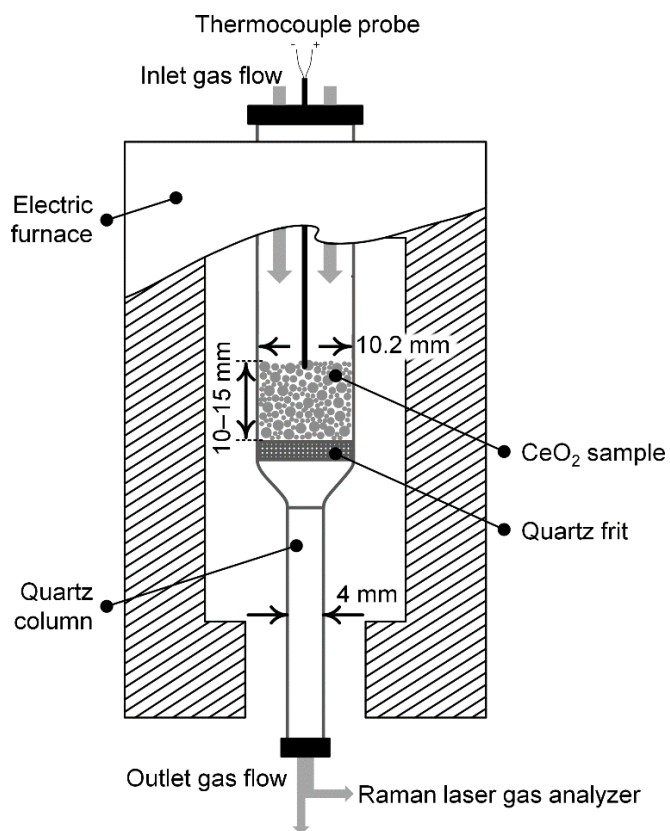

Fig. 5.2. Schematic of the packed bed reactor used to measure the rate of the oxidation of ceria (image courtesy of Dr. Luke Venstrom).
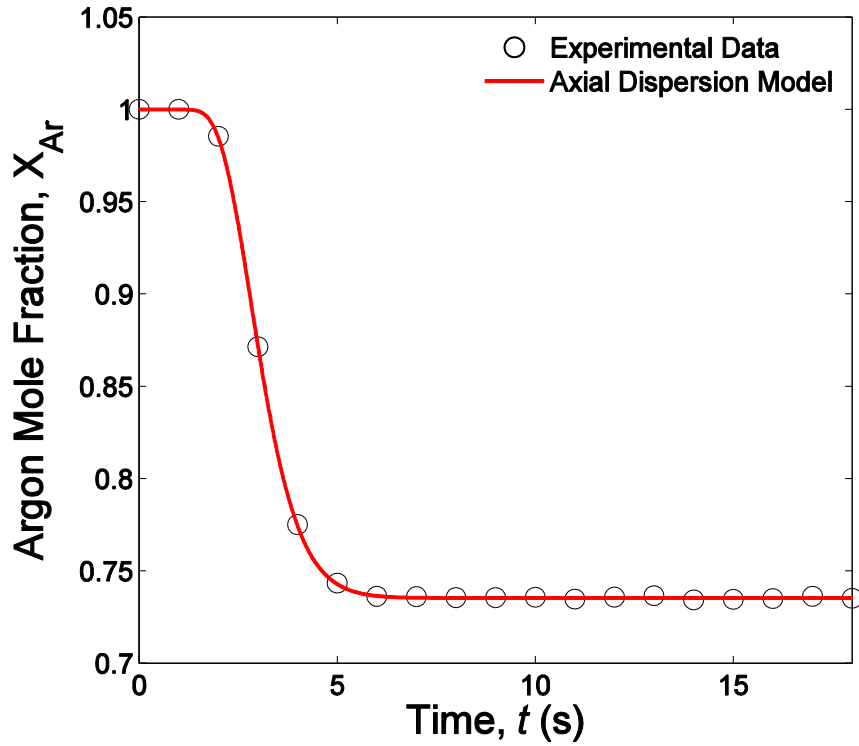
Fig. 5.3. Step change input test experimental data and its theoretical prediction.
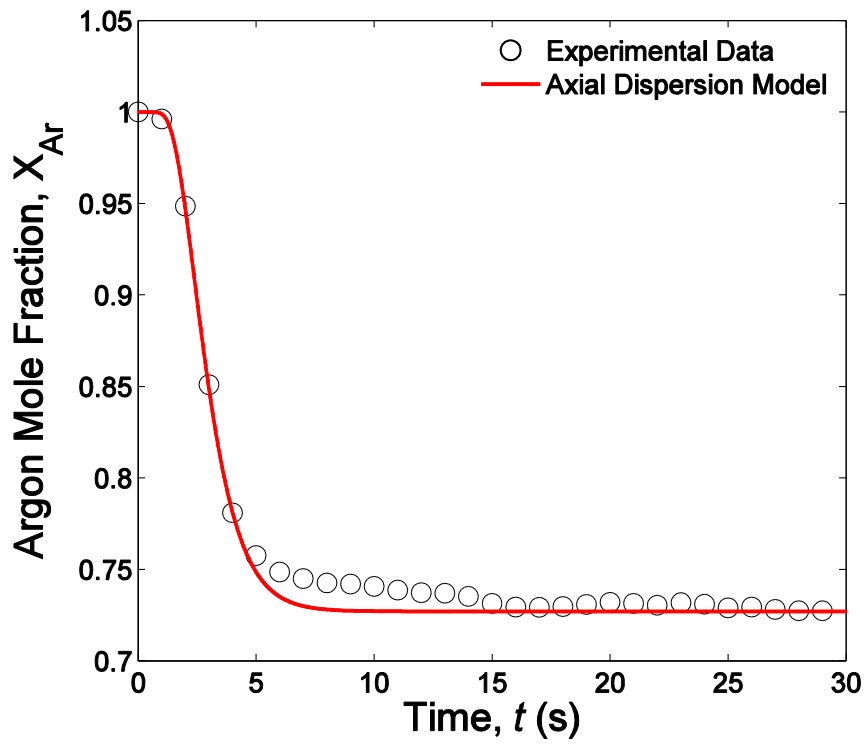

Fig. 5.4. Experimental data during oxidation and its theoretical prediction.
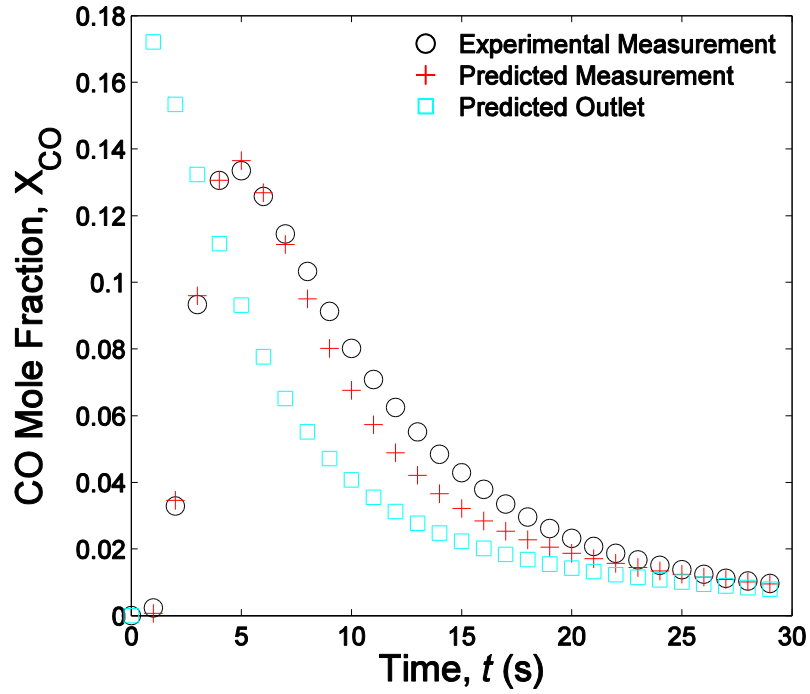
106

Fig. 5.5. Mole fraction comparisons using doubly ionized reaction rate, Eq. (5.13). The uncertainty in the experimental data is ± 0.0025.
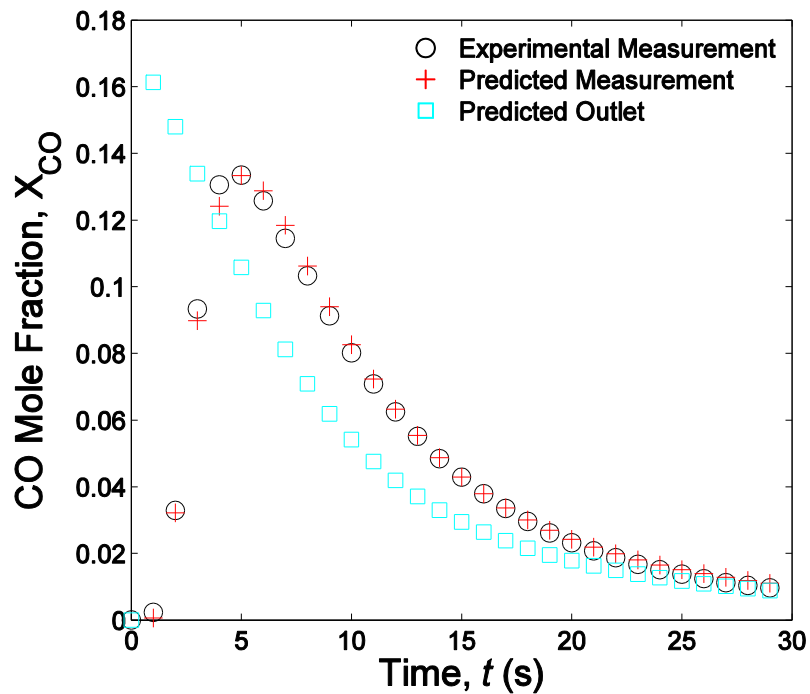

Fig. 5.6. Mole fraction comparisons using singly ionized reaction rate, Eq. (5.18). The uncertainty in the experimental data is ± 0.0025.
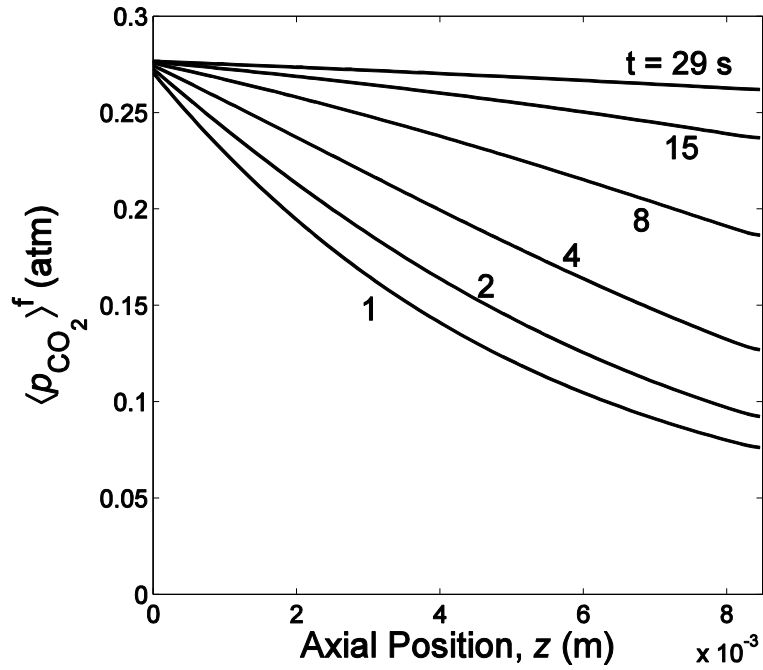
107

Fig. 5.7. Carbon dioxide partial pressure distributions at selected times for the singly ionized reaction rate expression with $\dot{n}''_{sf,0} = 6.14228 \times 10^{-4}$ kmol m^{-2} s^{-1}.

Fig. 5.8. Carbon monoxide partial pressure distributions at selected times for the singly ionized reaction rate expression with $\dot{n}''_{sf,0} = 6.14228 \times 10^{-4}$ kmol m^{-2} s^{-1}.

108

Fig. 5.9. Nonstoichiometry distributions at selected times for the singly ionized reaction rate expression with $\dot{n}''_{sf,0} = 6.14228 \times 10^{-4}$ kmol m^{-2} s^{-1}.

Fig. 5.10. Reaction rate distributions at selected times for the singly ionized reaction rate expression with $\dot{n}''_{sf,0} = 6.14228 \times 10^{-4}$ kmol m^{-2} s^{-1}. The reaction rate is negative for oxidation because the net interphase mass flux is from the fluid into the solid.
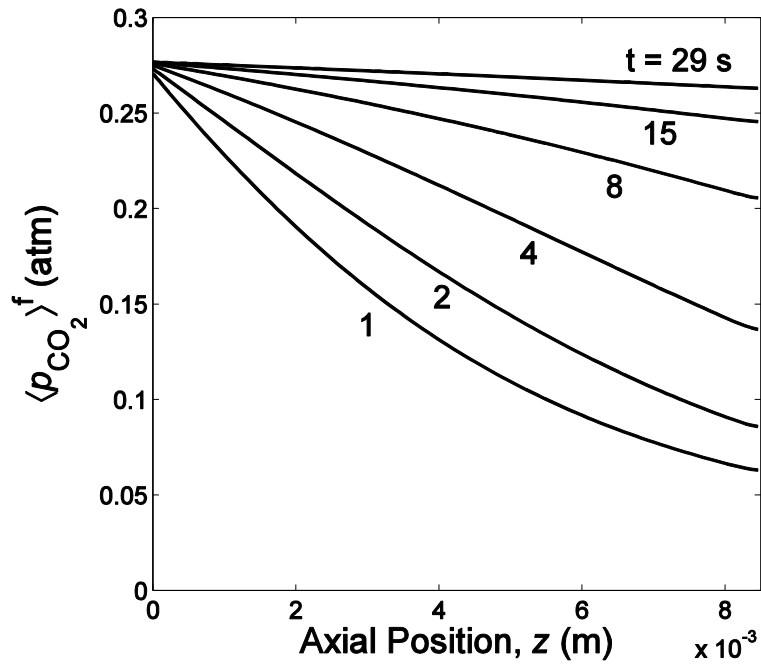
Fig. 5.11. Carbon dioxide partial pressure distributions at selected times for the doubly ionized reaction rate expression with $\dot{n}''_{sf,0} = 9.45939 \times 10^{-3}$ kmol m^{-2} s^{-1}.
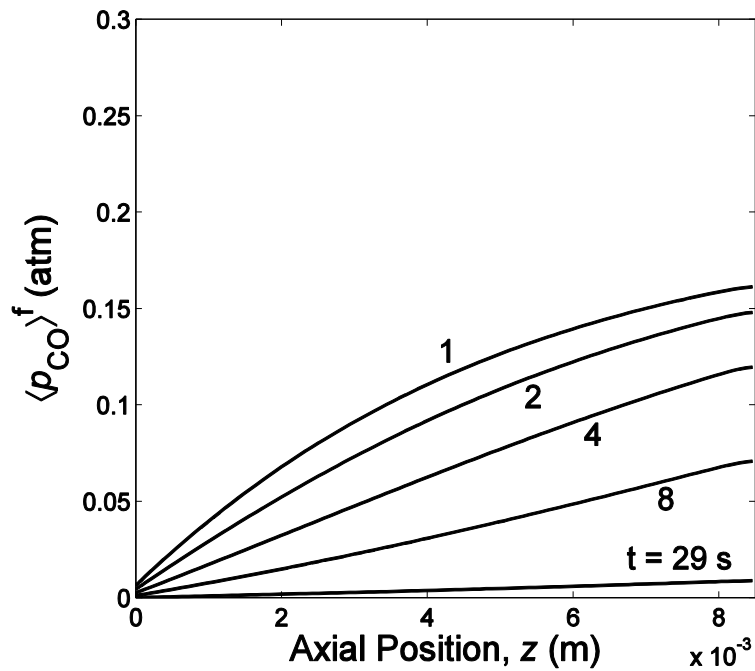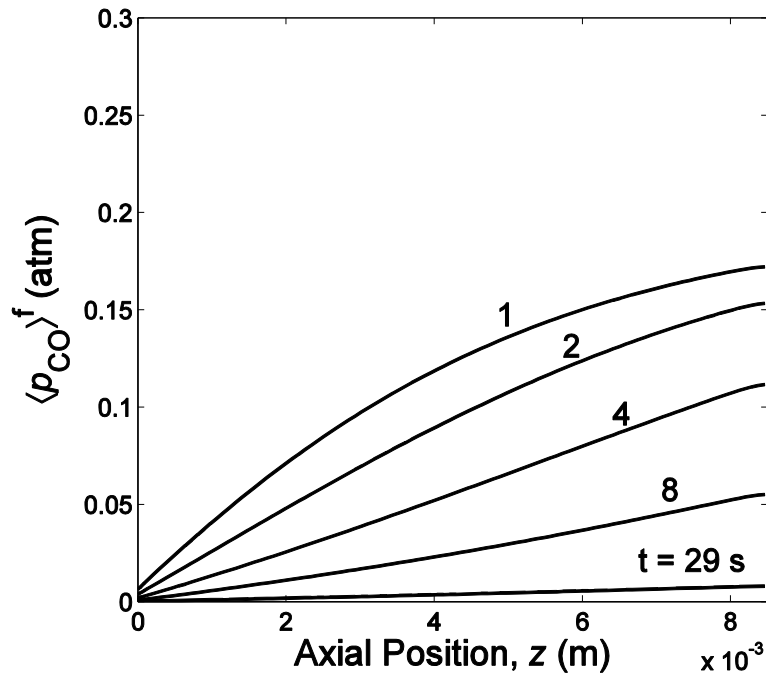

Fig. 5.12. Carbon monoxide partial pressure distributions at selected times for the doubly ionized reaction rate expression with $\dot{n}''_{sf,0} = 9.45939 \times 10^{-3}$ kmol m^{-2} s^{-1}.
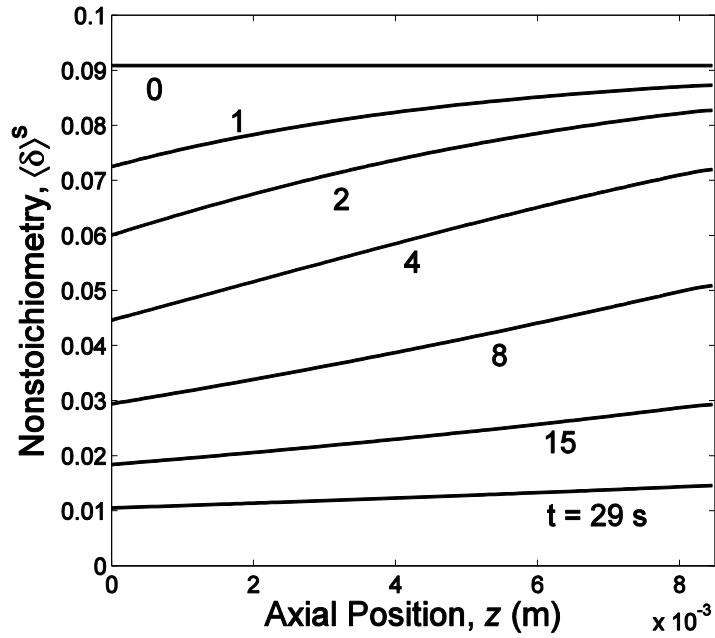
Fig. 5.13. Nonstoichiometry distributions at selected times for the doubly ionized reaction rate expression with $\dot{n}''_{sf,0} = 9.45939 \times 10^{-3}$ kmol m^{-2} s^{-1}.
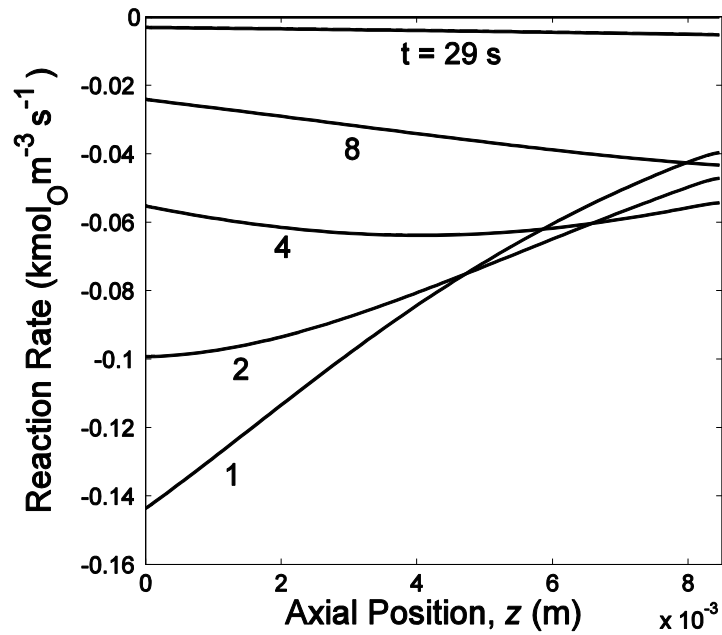

Fig. 5.14. Reaction rate distributions at selected times for the doubly ionized reaction rate expression with $\dot{n}''_{sf,0} = 9.45939 \times 10^{-3}$ kmol m^{-2} s^{-1}. The reaction rate is negative for oxidation because the net interphase mass flux is from the fluid into the solid.
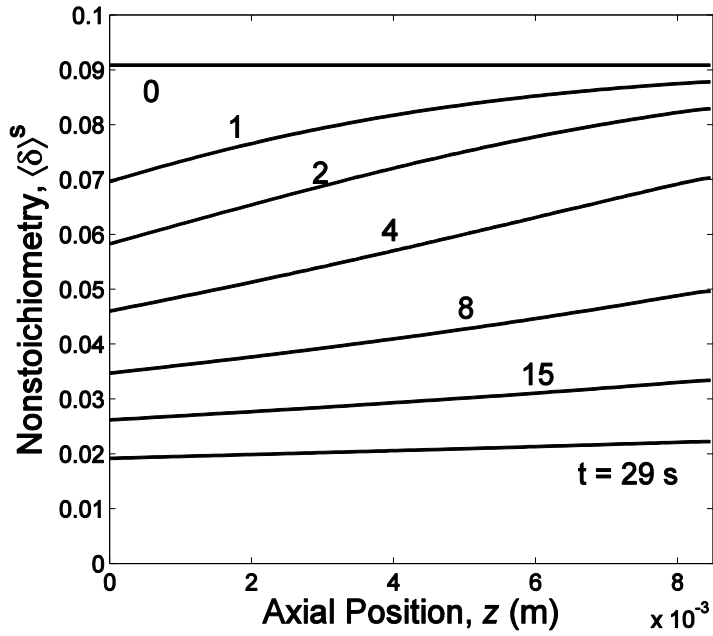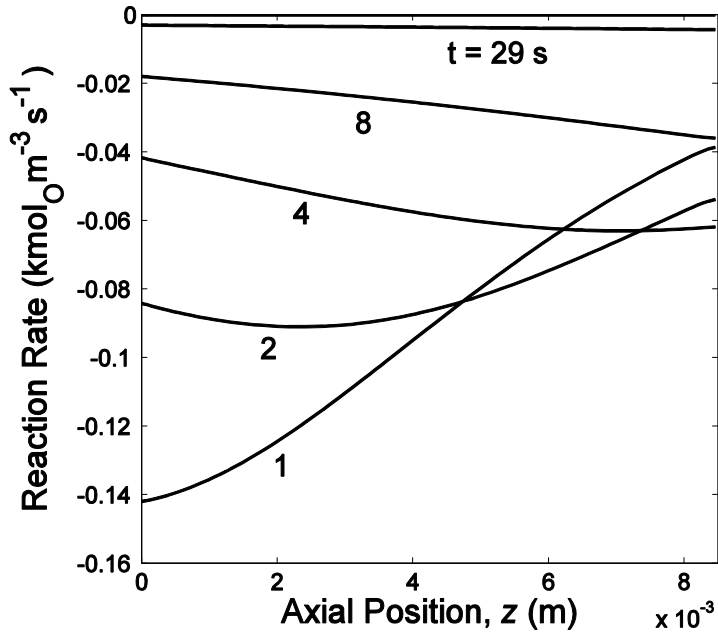
Chapter 6
Conclusion

To meet the projected worldwide demand for energy through the use of renewable sources, technologies must be developed that can both capture and store the abundance found in solar energy. Water and/or carbon dioxide splitting thermochemical cycles based on the redox chemistry of metal oxides are an attractive means to this end because their operating temperatures are compatible with concentrated solar energy systems while their closed material cycles and environmentally benign compounds ensure a long-term sustainable energy solution. In partial redox cycles, the metal oxide exists as a solid throughout the thermochemical cycle, which is an attractive attribute because it obviates separation challenges and creates new opportunities for cyclic processing.

Materials development efforts have identified promising metal oxides, proof-of-concept solar reactors have been tested, and thermodynamics has shown high efficiencies are possible by incorporating heat recovery. To inform the next steps toward commercializing solar thermochemical fuel production, this work has developed a multi-scale model of the multimode heat and mass transfer processes in a reactive porous structure by applying volume-averaging theory. A computational code was developed to numerically solve the governing equations and has been used to analyze both the thermal reduction and oxidation steps of the thermochemical cycle to provide insight into the dynamics of the temperature, nonstoichiometry, mass fraction, velocity, density, and pressure fields throughout the reactive medium.

Using the morphology to tailor the thermochemical response is investigated for a thermal reduction step where the porous structure is placed at the back of a cavity and directly irradiated with concentrated solar energy while a sweep gas flows through the pore network to remove the evolved oxygen product. In this configuration, the sweep gas functions as a thermal energy carrier in addition to its primary role of carrying away the evolved oxygen product. The porosity and Sauter mean diameter of the porous structure are varied from 0.6 to 0.9 and 10 to 1000 μm, respectively, to span the range of candidate

porous monoliths and investigate the impact of the pore morphology on the rate of oxygen release and the solar-to-chemical energy conversion efficiency associated with thermal reduction. When concentrated solar irradiation is used to heat the solid from the low temperature associated with an oxidation step to the high temperatures where oxygen release occurs, non-uniform heating of the solid increases the total amount of oxygen released. This increase in oxygen release is due to the nonlinear temperature dependence of the equilibrium nonstoichiometry values. The morphologies that best promote this beneficial non-uniform heating of the solid are those that minimize the sum of conductive and radiative heat transfer, which involves minimizing the sum of $k_{s,eff}$ and k_{rad}. However, decreasing k_{rad} through the use of small feature sizes (small Sauter mean diameters) also leads to a small permeability, which can become sufficiently small to create a pressure drop large enough to overwhelm the benefit of the non-uniform heating. Selecting an optimal porosity also involves a tradeoff because increasing the porosity decreases K and $k_{s,eff}$ while decreasing the porosity decreases k_{rad}. The optimal Sauter mean diameter associated with this tradeoff decreases as the porosity increases. Ultimately, the best performance was observed with a small feature size and a high porosity; an overall solar-to-chemical energy conversion efficiency of 10.9% was achieved with $d_{32} = 10$ μm and $\phi = 0.9$.

For oxidation, a method for testing hypothesized reaction rate expressions against experimental data was developed wherein the multiscale model is used to simulate a packed bed of porous particles and an axially-dispersed plug flow model is used to account for downstream mixing/dispersive processes and the dynamic response of the gas analysis instrument. Reaction rate expressions are developed and then compared with data for the isothermal oxidation of ceria by carbon dioxide at 1203 K. The reaction rate expression based on treating gas phase oxygen as a reaction intermediate with the quasi-steady state approximation and assuming the oxygen vacancies in the ceria lattice are singly ionized shows excellent agreement with the measured effluent compositions. A direct inference of the kinetics from the experimental data based on treating the packed bed as a differential flow reactor is expected to be inaccurate because the numerically predicted gradients within the experimental packed bed reactor are significant.

113

Because the developed model can be readily extended to other operating conditions, configurations, and solid–gas reactions, many opportunities exist to continue and/or expand this work. Within the context of solar thermochemical fuel production using reactive porous structures of ceria, different operating conditions and configurations should be explored because the morphological parameters that optimize performance are anticipated to depend on the configuration and operating conditions. For example, the macroscale geometry of the porous medium is an important consideration because the length will influence the optical thickness and impact how uniformly the solid is heated. Based on the findings of this study, the flow rate, composition, and temperature of the sweep gas are expected to be key process variables for the thermal reduction step that will greatly impact performance. In addition to determining how the optimal morphological parameters depend on the operating conditions, exploring different operating conditions could also quantify off-design performance. These considerations would greatly inform which morphology is best suited to a particular reactor concept or conversely indicate which operating conditions should be sought after when designing a reactor.

The value of a reaction rate expression that characterizes the intrinsic kinetics of oxidation would be tremendous. The agreement with experimental data at 1203 K is promising, but the developed parameter calibration technique must be applied to experimental data at multiple temperatures because the single parameter of the proposed reaction rate expressions is expected to depend on temperature. Once the kinetics are characterized, the morphological parameter space and different operating conditions can be explored for the oxidation step. Furthermore, a complete thermochemical cycle could be simulated. These simulations would allow the tradeoffs associated with optimizing the morphology for reduction *or* oxidation versus reduction *and* oxidation to be indentified and in so doing greatly inform how reactor performance can be optimized.

In expanding this work to study alternative configurations and operating conditions, the model can also be more targeted at porous monoliths with a specific morphology. For example, all of the effective transport properties can be evaluated using relationships obtained for a very specific morphology such as a 20 ppi RPC structure. As the number

114

of specific morphologies with well-characterized effective transport properties increases, more alternative morphologies can be considered. In regard to internal radiative heat transfer, methods other than the Rosseland diffusion approximation can be used to more fully capture the effects of anisotropic scattering and/or study reactive media that are not optically thick. Adopting a more advanced (and complex) treatment of scattering in the radiative heat transfer model is limited by the extent to which the radiative properties of a candidate morphology have been characterized. If considering reactive media whose optical thickness is small by virtue of a small macroscale dimension of the porous medium, a large difference between the pore-level and macroscale length scales needs to be maintained to preserve the validity of the representative elementary volume (REV) concept inherent to the use of volume-averaged transport equations.

References

[1] Lewis N., and Nocera D., 2006, "Powering the planet: Chemical challenges in solar energy utilization," Proceedings of the National Academy of Sciences, **103** , pp. 15729–15735.

[2] Fletcher E., 2001, "Solarthermal Processing: A Review," ASME J. of Solar Energy Engineering, **123** , pp. 63–74.

[3] Steinfeld A., and Palumbo R., 2001, "Solar thermochemical process technology," Encyclopedia of Physical Science and Technology, **15** , pp. 237–256.

[4] Steinfeld A., and Meier A., 2004, "Solar Fuels and Materials," Encyclopedia of Energy, **5** , pp. 623–637.

[5] Kodama T., 2003, "High-temperature solar chemistry for converting solar heat to chemical fuels," Progress in Energy and Combustion Science, **29** , pp. 567–597.

[6] Kodama T., and Gokon N., 2007, "Thermochemical Cycles for High-Temperature Solar Hydrogen Production," Chemical Reviews, **107** , pp. 4048–4077.

[7] Abanades S., Charvin P., Flamant G., and Neveu P., 2006, "Screening of water-splitting thermochemical cycles potentially attractive for hydrogen production by concentrated solar energy," Energy, **31** , pp. 2805–2822.

[8] Charvin P., Abanades S., Lemort F., and Flamant G., 2008, "Analysis of solar chemical processes for hydrogen production from water splitting thermochemical cycles," Energy Conversion and Management, **49** , pp. 1547–1556.

[9] Nakamura T., 1977, "Hydrogen production from water utilizing solar heat at high temperature," Solar Energy, **19**, pp. 467–475.

[10] Tamaura Y., Steinfeld A., Kuhn P., and Ehrensberger K., 1995, "Production of solar hydrogen by a novel, 2-step, water-splitting thermochemical cycle," Energy, **4** , pp. 325–330.

[11] Fresno F., Yoshida T., Gokon N., Fernandez-Saavedra R., and Kodama T., 2010, "Comparative study of the activity of nickel ferrites for solar hydrogen production by two-step thermochemical cycles," International Journal of Hydrogen Energy, **35** , pp. 8503–8510.

[12] Kodama T., Kondoh Y., Yamamoto R., Andou H., and Satou N., 2005, "Thermochemical hydrogen production by a redox system of ZrO2-supported Co(II)-ferrite," Solar Energy, **78** , pp. 623–631.

[13] Kodama T., Gokon N., and Yamamoto R., 2008, "Thermochemical two-step water splitting by ZrO2-supported NixFe3-xO4 for solar hydrogen production," Solar Energy, **82** , pp. 73–79.

[14] Gokon N., Mizuno T., Nakamuro Y., and Kodama T., 2008, "Iron-containing YSZ (yttrium-stabilized zirconia) system for two-step thermochemical water-splitting," ASME J. of Solar Energy Engineering, **130** .

[15] Ishihara H., Kaneko H., Hasegawa N., and Tamaura Y., 2008, "Two-step water-splitting at 1273-1623 K using yttria-stabilized zirconia-iron oxide solution via co-precipitation and solid-state reaction," Energy, **33** , pp. 1788–1793.

[16] Otsuka K., Hatano M., and Morikawa A., 1985, "Decomposition of Water by Cerium Oxide of delta-phase," Inorganica Chimica Acta, **109** , pp. 193–197.

[17] Abanades S., and Flamant G., 2006, "Thermochemical hydrogen production from a two-step solar-driven water-splitting cycle based on cerium oxides," Solar Energy, **80** , pp. 1611–1623.

[18] Chueh W., and Haile S., 2010, "A thermochemical study of ceria: exploiting an old material for new modes of energy conversion and CO2 mitigation," Philosophical Transactions of the Royal Society A, **368**, pp. 3269–3294.

[19] Charvin P., Abanades S., Beche E., Lemort F., and Flamant G., 2009, "Hydrogen production from mixed cerium oxides via three-step water-splitting cycles," Solid State Ionics, **180** , pp. 1003–1010.

[20] Kang K., Kim C., Park C., and Kim J., 2007, "Hydrogen Reduction and Subsequent Water Splitting of Zr-Added CeO2," Journal of Industrial and Engineering Chemistry, **13** , pp. 657–663.

[21] Kaneko H., Miura T., Ishihara H., Taku S., Yokoyama T., Nakajima H., and Tamaura Y., 2007, "Reactive ceramics of CeO2-MOx (M = Mn, Fe, Ni, Cu) for H2 generation by two-step water splitting using concentrated solar thermal energy," Energy, **32** , pp. 656–663.

[22] Kaneko H., Ishihara H., Taku S., Naganuma Y., Hasegawa N., and Tamaura Y., 2008, "Cerium ion redox system in CeO2-xFe2O3 solid solution at high temperatures (1273-1673K) in the two-step water-splitting reaction for solar H2 generation," Journal of Material Science, **43** , pp. 3153–3161.

117

[23]   Kaneko H., and Tamaura Y., 2009, "Reactivity and XAFS study on (1-x)CeO2-xNiO (x = 0.025-0.3) system in the two-step water-splitting reaction for solar H2 production," Journal of Physics and Chemistry of Solids, **70** , pp. 1008–1014.

[24]   Kaneko H., Taku S., Naganuma Y., Ishihara T., Hasegawa N., and Tamaura Y., 2010, "Development of Reactive Ceramics for Conversion of Concentrated Solar Heat Into Solar Hydrogen With Two-Step Water-Splitting Reaction," ASME J. of Solar Energy Engineering, **132** .

[25]   Tada M., Ishihara T., Kaneko H., and Tamaura Y., 2010, "O2-Releasing Reactivity of Ceria-based Reactive Ceramics on Irradiation of Concentrated Solar Beam for Solar Hydrogen Production," Proceedings of the ASME 2010 4th International Conference on Energy Sustainability .

[26]   Petkovich N., Rudisill S., Venstrom L. J., Davidson J. H., and Stein A., 2011, "Control of Heterogeneity in Nanostructured Ce1-xZrxO2 Binary Oxides for Enhanced Thermal Stability and Water Splitting Activity," Journal of Physical Chemistry C, **115**(43), pp. 21022–21033.

[27]   Agrafiotis C., Roeb M., Konstandopoulos A., Nalbandian L., Zaspalis V., Sattler C., Stobbe P., and Steele A., 2005, "Solar water splitting for hydrogen production with monolithic reactors," Solar Energy, **79** , pp. 409–421.

[28]   Roeb M., Sattler C., Kluser R., Monnerie N., de Oliveria L., Konstandopoulos A., Agrafiotis C., Zaspalis V., Nalbandian L., Steele A., and Stobbe P., 2006, "Solar Hydogen Production by a Two-Step Cycle Based on Mixed Iron Oxides," ASME J. of Solar Energy Engineering, **128** , pp. 125–133.

[29]   Kodama T., Hasegawa T., Nagasaki A., and Gokon N., 2009, "A Reactive Fe-YSZ Coated Foam Device for Solar Two-Step Water Splitting," ASME J. of Solar Energy Engineering, **131** .

[30]   Gokon N., Kodama T., Imaizumi N., Umeda J., and Seo T., 2011, "Ferrite/zirconia-coated foam device prepared for by spin coating for solar demonstration of thermochemical water-splitting," International Journal of Hydrogen Energy, **36** , pp. 2014–2028.

[31]   Kaneko H., Miura T., Fuse A., Ishihara H., Taku S., Fukuzumi H., Naganuma Y., and Tamaura Y., 2007, "Rotary-Type Solar Reactor for Solar Hydrogen Production with Two-step Water Splitting Process," Energy & Fuels, **21**, pp. 2287–2293.

[32] Chueh W., Falter C., Abbot M., Scipio D., Furler P., Haile S., and Steinfeld A., 2010, "High-Flux Solar-Driven Thermochemical Dissociation of CO2 and H2O Using Nonstoichiometric Ceria," Science, **330**, pp. 1797–1801.

[33] Furler P., Scheffe J. R., and Steinfeld A., 2012, "Syngas production by simultaneous splitting of H2O and CO2 via ceria redox reactions in a high-temperature solar reactor," Energy & Environmental Science, **5**(3), p. 6098.

[34] Furler P., Scheffe J., Gorbar M., Moes L., Vogt U., and Steinfeld A., 2012, "Solar Thermochemical CO2 Splitting Utilizing a Reticulated Porous Ceria Redox System," Energy & Fuels, **26**(11), pp. 7051–7059.

[35] Miller J., Allendorf M., Diver R., Evans L., Siegel N., and Stuecker J., 2008, "Metal oxide composites and structures for ultra-high temperature solar thermochemical cycles," Journal of Material Science, **43** , pp. 4714–4728.

[36] Liang Z., Chueh W., Ganesan K., Haile S., and Lipinski W., 2011, "Experimental Determination of Transmittance of Porous Cerium Dioxide Media in the spectral range of 300--1100 nm," Experimental Heat Transfer, **24**(4), pp. 285–299.

[37] Ganesan K., and Lipinski W., 2011, "Experimental Determination of Spectral Transmittance of Porous Cerium Dioxide in the Range 900--1700 nm," ASME Journal of Heat Transfer, **133**(10), p. 104501.

[38] Ganesan K., Dombrovsky L. A., and Lipiński W., 2013, "Visible and near-infrared optical properties of ceria ceramics," Infrared Physics & Technology, **57**, pp. 101–109.

[39] Haussener S., and Steinfeld A., 2012, "Effective Heat and Mass Transport Properties of Anisotropic Porous Ceria for Solar Thermochemical Fuel Generation," Materials, **5**(12), pp. 192–209.

[40] Chueh W., and Haile S., 2009, "Ceria as a Thermochemical Reaction Medium for Selectively Generating Syngas or Methane from H20 & CO2," ChemSusChem, **2**, pp. 735–739.

[41] Venstrom L. J., Petkovich N., Rudisill S., Stein A., and Davidson J. H., 2012, "The Effects of Morphology on the Oxidation of Ceria by Water and Carbon Dioxide," ASME J. of Solar Energy Engineering, **134**(1), p. 011005 (8).

[42] Rudisill S. G., Venstrom L. J., Petkovich N. D., Quan T., Hein N., Boman D. B., Davidson J. H., and Stein A., 2013, "Enhanced Oxidation Kinetics in Thermochemical Cycling of CeO2 through Templated Porosity," Journal of Physical Chemistry C, **117**, pp. 1692–1700.

[43] Al-Hamamre Z., Al-Zoubi A., and Trimis D., 2010, "Numerical Investigation of the partial oxidation process in porous media based reformer," Combustion Theory and Modelling, **14** , pp. 91–103.

[44] Dhamrat R., and Ellzey J., 2006, "Numerical and experimental study of the conversion of methane to hydrogen in a porous media reactor," Combustion and Flame, **144** , pp. 698–709.

[45] Farzaneh M., Ebrahimi R., Shams M., and Shafiey M., 2007, "Two-dimensional Numerical Simulation of Combustion and Heat Transfer in Porous Burners," Engineering Letters.

[46] Keshtkar M., and Nassab S. G., 2009, "Theoretical analysis of porous radiant burners under 2-D radiation field using discrete ordinates method," Journal of Quantitative Spectroscopy and Radiative Transfer, **110** , pp. 1894–1907.

[47] Malico I., and Pereira J., 2001, "Numerical Study on the Influence of Radiative Properties in Porous Media Combustion," ASME Journal of Heat Transfer, **123** , pp. 951–957.

[48] Mishra S., Steven M., Nemoda S., Talukdar P., Trimis D., and Durst F., 2006, "Heat transfer analysis of a two-dimensional rectangular porous radiant burner," International Communications in Heat and Mass Transfer, **33** , pp. 467–474.

[49] Du L., and Xie M., 2006, "The Influences of Thermophysical Properties of Porous Media on Superadiabatic Combustion with Reciprocating Flow," Heat Transfer-Asian Research, **35** , pp. 336–350.

[50] Szekely J., Evans J., and Sohn H., 1976, Gas-Solid Reactions, Academic Press .

[51] Valipour M., and Saboohi Y., 2007, "Modeling of multiple noncatalytic gas-solid reactions in a moving bed of porous pellets based on finite volume method," Heat and Mass Transfer, **43** , pp. 881–894.

[52] Gupta P., and Saha R., 2004, "Analysis of Gas-Solid Noncatalytic Reactions in Porous Particles: Finite Volume Method," International Journal of Chemical Kinetics, **36** , pp. 1–11.

[53] Peters B., 2003, Thermal Conversion of Solid Fuels, WIT Press .

[54] Lipinski W., and Steinfeld A., 2004, "Heterogeneous thermochemical decomposition under direct irradiation," International Journal of Heat and Mass Transfer, **47** , pp. 1907–1916.

[55] Dombrovsky L., Schunk L., Lipinski W., and Steinfeld A., 2009, "An ablation model for the thermal decomposition of porous zinc oxide layer heated by concentrated solar radiation," International Journal of Heat and Mass Transfer, **52** , pp. 2444–2452.

[56] Schunk L., Lipinski W., and Steinfeld A., 2009, "Ablative Heat Transfer in a Shrinking Packed-Bed of ZnO Undergoing Solar Thermal Dissociation," American Institute of Chemical Engineering, **55** , pp. 1659–1666.

[57] Osinga T., Olalde G., and Steinfeld A., 2004, "Solar Carbothermal Reduction of ZnO: Shrinking Packed-Bed Reactor Modeling and Experimental Validation," Industrial and Engineering Chemistry Research, **43** , pp. 7981–7988.

[58] Belghit A., Daguenet M., and Reddy A., 2000, "Heat and mass transfer in a high temperature moving packed bed subject to an external radiative source," Chemical Engineering Science, **55** , pp. 3967–3978.

[59] Lipinski W., and Steinfeld A., 2005, "Transient radiative heat transfer within a suspension of coal particles undergoing steam gasification," Heat and Mass Transfer, **41** , pp. 1021–1032.

[60] Lipinski W., Z'Graggen A., and Steinfeld A., 2005, "Transient Radiation Heat Transfer within a Nongray Nonisothermal Absorbing-Emitting-Scattering Suspension of Reacting Particles Undergoing Shrinkage," Numerical Heat Transfer, Part B, **47** , pp. 443–457.

[61] Lipinski W., Thommen D., and Steinfeld A., 2006, "Unsteady radiative heat transfer within a suspension of ZnO particles undergoing thermal dissociation," Chemical Engineering Science, **61** , pp. 7029–7035.

[62] Lloyd G., Razani A., and Kim K., 2001, "Formulation and Numerical Solution of Non-Local Thermal Equilibrium Equations for Multiple Gas/Solid Porous Metal Hydride Reactors," ASME Journal of Heat Transfer, **123** , pp. 520–526.

[63] Lautenberger C., and Fernandez-Pello C., 2009, "A model for the oxidative pyrolysis of wood," Combustion and Flame, **156** , pp. 1503–1513.

[64] Agrafiotis C., Pagkoura C., Lorentzou S., Kostoglou M., and Konstandopoulos A., 2007, "Hydrogen production in solar reactors," Catalysis Today, **127** , pp. 265–277.

[65] Lapp J., Davidson J. H., and Lipinksi W., 2012, "Efficiency of two-step solar thermochemical non-stoichiometric redox cycles with heat recovery," Energy, **37** , pp. 591–600.

[66]   Whitaker S., 1999, The Method of Volume Averaging, Kluwer Academic .

[67]   Dombrovsky L. A., Ganesan K., and Lipiński W., 2012, "Combined two-flux approximation and Monte Carlo model for identification of radiative properties of highly scattering dispersed materials," Computational Thermal Sciences, **4**, pp. 365–378.

[68]   Cussler E. L., 2009, Diffusion: Mass Transfer in Fluid Systems, Cambridge University Press, Cambridge.

[69]   Yaws C., ed., 2009, "Transport Properties of Chemicals and Hydrocarbons: Viscosity, Thermal Conductivity, and Diffusivity of C1 to C100 organics and Ac to Zr inorganics."

[70]   Binnewies M., and Milke E., eds., 2002, "Thermochemical data of elements and compounds."

[71]   Chekhovskoy V. Y., and Stavrovsky G. I., 1970, "Thermal Conductivity of Cerium Dioxide," Ninth Conference on Thermal Conductivity, pp. 295–298.

[72]   Panlener R., Blumenthal R., and Garnier J., 1975, "A thermodynamic study of nonstoichiometric cerium dioxide," Journal of Physics and Chemistry of Solids, **36**, pp. 1213–1222.

[73]   Modest M., 2003, Radiative Heat Transfer, Academic Press, New York.

[74]   Kaviany M., 1995, Principles of Heat Transfer in Porous Media, Springer, New York.

[75]   Wakao N., Kaguei S., and Funazkri T., 1979, "Effect of fluid dispersion coefficients on particle-to-fluid heat transfer coefficients in packed beds. Correlation of Nusselt numbers.," Chemical Engineering Science, **34** , pp. 325–336.

[76]   Kuwahara F., Yang C., Ando K., and Nakayama a., 2011, "Exact Solutions for a Thermal Nonequilibrium Model of Fluid Saturated Porous Media Based on an Effective Porosity," Journal of Heat Transfer, **133**(11), p. 112602.

[77]   Ferziger J. H., and Peric M., 2001, Computational Methods for Fluid Dynamics, Springer, New York.

[78]   Patankar S., 1980, Numerical Heat Transfer and Fluid Flow, Taylor & Francis, London.

[79] Bader R., Venstrom L., Davidson J., and Lipinski W., 2013, "Thermodynamic analysis of isothermal redox cycling of ceria for solar fuel production," Energy & Fuels, In press.

[80] Lapp J., 2013, "Heat Transfer Analysis of a Solid-Solid Heat Recuperation System for Solar-Driven Nonstoichiometric Redox Cycles," Journal of Solar Energy Engineering, **135**(3), p. 031004.

[81] Keene D. J., Davidson J. H., and Lipinski W., 2013, "A Model of Transient Heat and Mass Transfer in a Heterogeneous Medium of Ceria Undergoing Nonstoichiometric Reduction," Journal of Heat Transfer, **135**(5), p. 052701.

[82] Petrasch J., Wyss P., Stämpfli R., and Steinfeld A., 2008, "Tomography-Based Multiscale Analyses of the 3D Geometrical Morphology of Reticulated Porous Ceramics," Journal of the American Ceramic Society, **91**(8), pp. 2659–2665.

[83] Petrasch J., Wyss P., and Steinfeld a., 2007, "Tomography-based Monte Carlo determination of radiative properties of reticulate porous ceramics," Journal of Quantitative Spectroscopy and Radiative Transfer, **105**(2), pp. 180–197.

[84] Petrasch J., Meier F., Friess H., and Steinfeld A., 2008, "Tomography based determination of permeability, Dupuit–Forchheimer coefficient, and interfacial heat transfer coefficient in reticulate porous ceramics," International Journal of Heat and Fluid Flow, **29**(1), pp. 315–326.

[85] Petrasch J., Schrader B., Wyss P., and Steinfeld A., 2008, "Tomography-Based Determination of the Effective Thermal Conductivity of Fluid-Saturated Reticulate Porous Ceramics," Journal of Heat Transfer, **130**(3), p. 032602.

[86] Haussener S., Coray P., Lipinski W., Wyss P., and Steinfeld A., 2010, "Tomography-Based Heat and Mass Transfer Characterization of Reticulate Porous Ceramics for High-Temperature Processing," ASME Journal of Heat Transfer, **132** .

[87] Dombrovsky L. A., 2012, "The Use of Transport Approximation and Diffusion-based Models in Radiative Transfer Calculations," Computational Thermal Sciences, **4**(4), pp. 297–315.

[88] Akolkar a., and Petrasch J., 2012, "Tomography-Based Characterization and Optimization Of Fluid Flow Through Porous Media," Transport in Porous Media, **95**(3), pp. 535–550.

[89] Haussener S., Coray P., Lipiński W., Wyss P., and Steinfeld A., 2010, "Tomography-Based Heat and Mass Transfer Characterization of Reticulate

Porous Ceramics for High-Temperature Processing," Journal of Heat Transfer, **132**(2), p. 023305.

[90]   Nield D. A., 1991, "Estimation of the Stagnant Thermal Conductivity of Saturated Porous Media," International Journal of Heat and Mass Transfer, **34**(6), pp. 1575–1576.

[91]   Apetz R., and Bruggen M. P. B., 2003, "Transparent Alumina: A Light-Scattering Model," Journal of the American Ceramic Society, **86**(3), pp. 480–486.

[92]   Hsu P.-F., and Howell J. R., 1992, "Measurements of Thermal Conductivity and Optical Properties of Porous Partially Stabilized Zirconia," Experimental Heat Transfer, **5**, pp. 293–313.

[93]   Tien C. L., and Drolen B. L., 1987, "Thermal Radiation in Particulate Media with Dependent and Independent Scattering," Annual Review of Numerical Fluid Mechanics and Heat Transfer, **1**, pp. 1–32.

[94]   Marabelli F., and Wachter P., 1987, "Covalent insulator CeO2: Optical reflectivity measurements," Physical Review B, **36**(2), pp. 1238–1243.

[95]   Bohren C., and Huffman D., 1998, Absorption and Scattering of Light by Small Particles, Wiley-VCH, New York.

[96]   Levenspiel O., 1998, Chemical Reaction Engineering, Wiley.

[97]   Bird R., Stewart W., and Lightfoot E., 2007, Transport Phenomena, Wiley.

[98]   Beavers G. S., Sparrow E. M., and Rodenz D. E., 1973, "Influence of Bed Size on the Flow Characteristics and Porosity of Randomly Packed Beds of Spheres," Journal of Applied Mechanics, **40**(3), pp. 655–660.

[99]   Wetter M., 2011, "GenOpt Generic Optimization Program."